2016

High-Resolution Correlation Using Geophysical and Geochemical Methods on Three Cambrian Drumian Marine Sedimentary Successions in The House Range Embayment, Western Laurentia

Emad I. Elfar
Louisiana State University and Agricultural and Mechanical College

HIGH-RESOLUTION CORRELATION USING GEOPHYSICAL AND GEOCHEMICAL METHODS ON THREE CAMBRIAN DRUMIAN MARINE SEDIMENTARY SUCCESSIONS IN THE HOUSE RANGE EMBAYMENT, WESTERN LAURENTIA

A Dissertation

Submitted to the Graduate Faculty of the
Louisiana State University and
Agricultural and Mechanical College
in partial fulfillment of the
requirements for the degree of
Doctor of Philosophy

in

The Department of Geology and Geophysics

by
Emad Ismail Elfar
B.S., Tanta University, 2002
M.S., Tanta University, 2009
August 2016

ACKNOWLEDGEMENTS

After having my master degree from Tanta University, I got a full funded PhD mission from the Egyptian Ministry of Higher Education in a competitive funding opportunity in 2011. I did not hesitate to contact the soon-to-be my advisor, Dr. Brooks Ellwood, who I worked with in collecting two Paleocene/Eocene boundary sections in Upper Egypt in 2004. I am deeply thankful to him for his continuous support, guidance and advice during the progress of this project. He was extremely helpful from day one when he picked me up from Baton Rouge airport and assisted me settle down, through helping during multiple field trips that were funded from the Robey Clark endowment at Louisiana State University, to reviewing multiple manuscripts.

I would like also to thank Suzanne Ellwood, Eman Eldakkak, Jennifer Kenyon, and Minhee Chou for their kind assistance during the field work and sample collection. I am greatly indebted to Amber Ellwood for her help during samples preparation and measurement for magnetic susceptibility and carbonate contents, and for running selected samples for carbon and oxygen isotopes.

I would like to express my deep gratitude to my committee members, Dr. Samuel Bentley, Dr. Sophie Warny, and Dr. Wei-Hsung Wang for their valuable discussions and suggestions that helped me to expand my expertise over the course of this research.

Finally, this appreciation is extended to my wife, Eman Eldakkak, for her unlimited encouragement and incredible help in so many different ways that can never be repaid.

PREFACE

The goal of this research is to trace and constrain not only the base of the Drumian stage but also the LOOP/FAD of *P. atavus* and the DICE in the HRE. Accounting for lithologic complexity among the three studied sections is a prerequisite for such study. Therefore, this dissertation is divided into three chapters. Each chapter is a stand-alone paper for publication.

Chapter one represents high-resolution lithostratigraphic correlation among the three studied sections based mainly on detailed detrital/carbonate investigations. This paper is the product of research that had four goals. First, to investigate the complex lithological variations and their causes in the HRE among the Drum Mountains GSSP (UT), House Range Marjum Pass (UT), and Snake Range Packrat (NV) sections. Second, to interpret from these data climatic and sea level fluctuations that have caused the lithologic complexities. Third, to determine and refine the depositional setting represented by each section. Fourth, to identify, trace and interpret some of the numerous storm-event layers identified within the HRE.

Chapter two aims to identify lithostratigraphic marker (s) that might be used to trace important surfaces such as the base of the Drumian Stage and the FAD/LOOP of *P. atavus* from the GSSP through the Marjum Pass and into the Packrat section. It also aims to test the synchronicity of *P. atavus* within the HRE, and investigate the reliability of *P. atavus* as biostratigraphic marker for high resolution studies.

Chapter three provides high resolution chemostratigraphic correlation among three slope and basinal sections where hundreds of samples have been analyzed to test DICE synchronicity regionally within the HRE across the base of the Drumian Stage. In addition,

this test is extended to three southern carbonate platform sections (Wah Wah, Panaca Hills and Desert Range). Their published chemostratigraphic data sets (Howley, 2010; Howley and Jiang, 2010) were used.

TABLE OF CONTENTS

ABSTRACT

The Global boundary Stratotype Section and Point (GSSP) of the base of the Cambrian Drumian Stage was defined at 62 m above the base of the Wheeler formation, at the First Appearance Datum (FAD) of *Ptychagnostus atavus* (*P. atavus*), and at 10 meter below the DrumIan Carbon isotope Excursion (DICE) on the Stratotype Ridge in the Drum Mountains western Utah, (Babcock at al., 2004; 2007). Tracing the base of the the Drumian stage to other Middle Cambrian sequences in the House Range Embayment (HRE), a fault-controlled deep-water intrusion into an extensive carbonate platform along the passive margin of western Laurentia, was tentative and uncertain. The complex lithological variations, the absence of lithostratigraphic and other reliable biostratigraphic markers, and the widely-spaced sampling and coarse correlation among HRE sections, have contributed to such uncertainty. This study focuses on regional high-resolution correlation among the Drumian GSSP section, the Marjum Pass section, and the Packrat section. The objective of this research is to account for such complex facies variations, and constrain not only the base of the Drumian Stage but also the Lowest Occurrence Observed Point (LOOP)/FAD of *P. atavus*, and the DICE within the HRE.

The HRE lithological variations follow broad facies patterns. Carbonates dominate at the edges of the HRE and decrease inward, while detrital materials dominate along the HRE trough and decrease outward. Three storm layers helped in tracing important surfaces including the base of the Drumian Stage from one section into the other. Unfortunately, the GSSP was defined based on reworked *P. atavus* specimens at the base of the first storm layer that has an erosional base and is composed of reworked sediments. Therefore, the FAD/LOOP of *P. atavus* is diachronous and its acme is synchronous within the three studied sections. It is

concluded also that the DICE is a chronostratigraphic marker that constrain the base of the Drumian Stage in the embayment and the nearby southern platform sections unless suppressed by the incoming heavy-isotopic platform carbonates. The DICE maximum negative $\delta^{13}C$ excursion is synchronous while the onset and the end of the DICE are diachronous.

CHAPTER I: SEA LEVEL AND CLIMATIC-INDUCED FACIES VARIATIONS IN THE MIDDLE-CAMBRIAN HOUSE RANGE EMBAYMENT, WESTERN LAURENTIA

The Middle-Cambrian House Range Embayment (HRE) represents a deep-water intrusion into an extensive carbonate platform along the passive margin of western Laurentia. The distribution and source of the HRE mixed siliciclastic-carbonate sediments are poorly understood because many key elements have been missed during field observations or coarse correlation. This study accounts for the complex lithological variations in the HRE, and improves our understanding concerning the global climatic and sea level fluctuations that drive these variations. Magnetic susceptibility (χ) and carbonate content ($CaCO_3$%) are used to construct high-resolution correlation among three overlapping Middle-Cambrian marine sedimentary sections. Successions studied are; 1) the Drumian Global boundary Stratotype Section and Point (GSSP) in the Drum Mountains, western Utah, 2) the Marjum Pass section in the House Range, western Utah, and 3) the Packrat section in Great Basin National Park, eastern Nevada. The HRE lithological variations follow broad facies patterns. Carbonates dominate at the edges of the HRE and decrease inward, while detrital materials dominate along the HRE trough and decrease outward. The carbonate/detrital ratio varies on the HRE ramps, the area between the HRE Edge and trough, due to; 1) the position of each section, (2) sea level fluctuations, and 3) the physical processes, primarily storms, that act on the carbonate platform. This ratio increases during sea level fall and storm events, and maximizes during the maximum sea level fall. It also decreases during sea level rise, and reaches its minimum at times when sea level is at a maximum stand. Careful examination of facies variations among the studied sections helps to decipher the depositional setting at each section. The GSSP is a shallow trough section, the

Marjum Pass is a lower slope section of the northern HRE ramp, and the Packrat is a lower slope section of the southern HRE ramp.

1.1. Introduction

The Middle-Cambrian HRE was formed by a normal fault that extended about 400 km in a NE-SW direction across what is known as the Great American Carbonate Bank (Hintze, 1988) (Figs. 1.1 and 1.2). The Great American Carbonate Bank is a Laurentian extensive carbonate continental shelf that is built up mainly from algal and/or microbial carbonate sediment (Palmer, 1971; Brady and Koepnick, 1979; Aitken, 1997) (Fig. 1.1). The fault bounds the southern margin of the asymmetric embayment separating the shallow-water carbonate sediment from deep-water, terrigenous-dominated sediment (Rees, 1986). The northern margin of this trough is a drowning platform that was formed as a southward sloping ramp (Rees, 1986). As the Laurentian landmass turned counterclockwise during the Phanerozoic, the normal fault rotated from the NW-SE to the NE-SW direction (Rees, 1986) (Figs. 1.1 and 1.2). In this paper, today's coordinates is used unless otherwise stated. Therefore, the easterly paleo-trade winds are referred to here as northerly trade winds. Although the Middle-Cambrian HRE was subjected to four compressional periods during the Paleozoic and Mesozoic, and extensional periods during the Cenozoic, that displaced and distorted its original configuration, the studied sections reported here lie in areas that have little deformation (Dickinson, 1981; Robison, 1982; Speed, 1982; Rees, 1984; 1986).

Many paleontological, sedimentological and stratigraphical studies have been done using multiple sections from within and outside the embayment (Palmer, 1965; Brady and Koepnick, 1979; Dickinson, 1981; Robison, 1982; Speed, 1982; Rees, 1986; Aitken, 1997; Elrick and Snider, 2002; Langenburg, 2003; Howley and Jiang,

2007; Brett et al., 2009; Halgedahl et al., 2009; Howley and Jiang, 2010). They rely on widely-spaced sampling and field observations to extract sea level fluctuations, tectonic evolution and depositional history of the HRE. Although they are useful in examining spatial and temporal long-term variations among sedimentary sequences, many key elements may be missed and misinterpreted, especially when high resolution is required. More challenges are added at the upper carbonate ramp, close to the carbonate platform, where varying carbonate production, sea level fluctuations, and physical processes produce rapidly changing lithologies. Identifying and tracing small-scale erosional surfaces, hiatuses, and minor thickness changes are key elements in distinguishing between normal deposition and storm deposits. Closely spaced sampling, along with field observations, are necessary to unravel some of these complexities. This study focuses on regional high-resolution correlation among three Middle Cambrian marine sedimentary sections that are located within the HRE and cover the interval through the base of the Drumian Stage. The sampled sections include; 1) the Global boundary Stratotype Section and Point (GSSP) for the Drumian Stage that has been placed on Stratotype Ridge in the Drum Mountains, western Utah, 2) the Marjum Pass section in the House Range, western Utah, and 3) the Packrat section in Great Basin National Park, along the southern flank of the Snake Range, eastern Nevada (Fig. 1.2). Both the GSSP and Marjum Pass sections have been previously studied and their depositional setting have been defined. The GSSP was introduced as a slope section while the Marjum Pass section was reported to be deposited at the deepest part of the HRE (Langenburg, 2003; Babcock et al., 2004; 2007; Howley, 2010; Howley and Jiang, 2010)

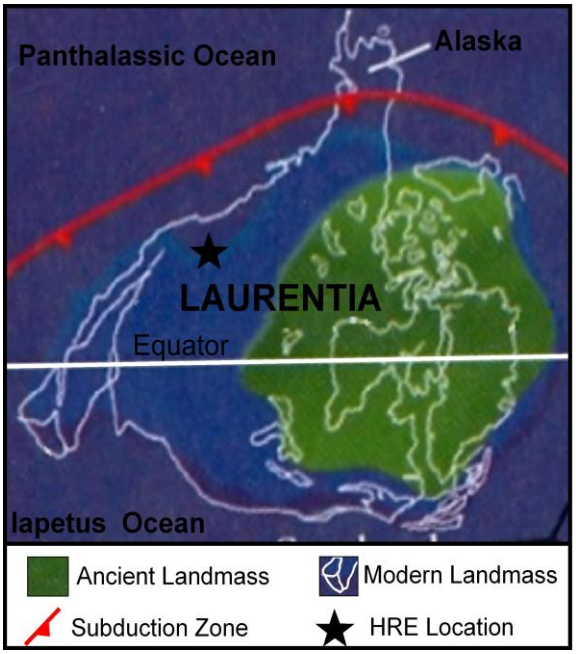

Figure 1.1. Paleogeographic map showing the Laurentian extensive carbonate shelf of the Middle Cambrian System. The approximate location of the House Range Embayment (HRE) is shown as a star (Scotese, 2001).

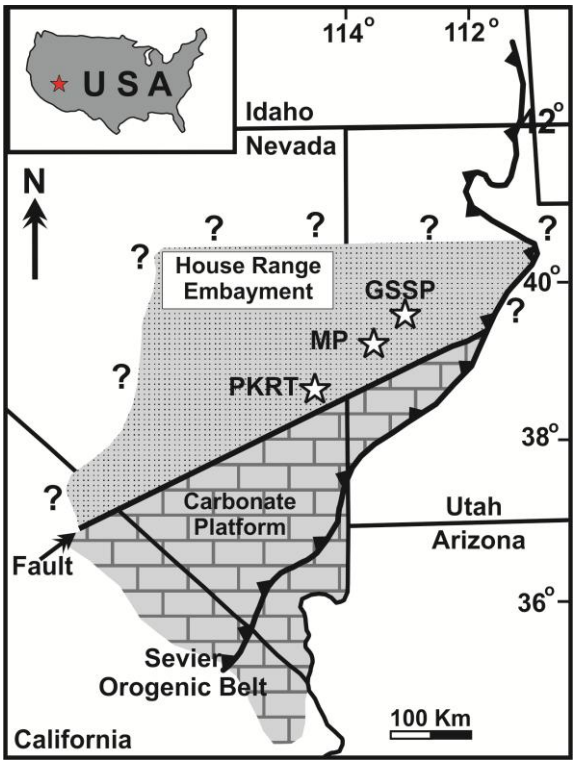

Figure 1.2. Non-palinspastic reconstruction map showing the location of the studied GSSP, Marjum Pass and Packrat sections (modified from Palmer, 1971; Elrick and Snider, 2002; Howley et al., 2006). As the Laurentian landmass turned counterclockwise during the Phanerozoic, the normal fault rotated 90° from the NW-SE to the NE-SW direction (Rees, 1986). The NE–SW normal fault separates the Laurentian carbonate shelf facies from the slope, with mixed siliciclastic-carbonate facies.

This paper is the product of research that had four goals. First, to investigate the complex lithological variations and their causes in the HRE. Second, to interpret climatic and sea level fluctuations that have caused the lithologic complexities. Third, to determine and refine the depositional setting represented by each section. Fourth, to identify, trace and interpret some of the numerous storm-event layers identified within the HRE.

1.2. Methods

1.5.1. Sampling and field observations

In the GSSP outcrop, minor structures including faults were observed on the Stratotype Ridge; the ridge that hosts the GSSP section. Therefore, the GSSP section was collected from the eastern flank of the Stratotype Ridge where three indurated limestone beds were traced ~130 meters away from the observed fault. The new location has better outcrop because the base of the Drumian Stage is well exposed, and no structures have been observed. In the Packrat section and nearby equivalent outcrops, syndepositional structures including folds, erosional surfaces, and debris flow are observed. A total of 1009 samples were collected from the three studied outcrops at 5 to 10 cm uniform intervals. All covered intervals were cleaned and brushed to the freshest surface possible. 20-30 gm of each sample were placed in small pre-labeled plastic zip-lock bags then grouped in larger cloth bags and returned to the Rock Magnetism Laboratory at LSU for final preparation and measurement. Each measurement is assumed to represent relatively short period of time. All samples were run for mass-specific magnetic susceptibility (χ) and carbonate percent ($CaCO_3$%). Because the facies within the HRE are mainly composed of varying ratios of carbonates and detrital materials, laboratory χ and $CaCO_3$% data are used to investigate and interpret lithologies. The three outcrops

were examined, in details, for structural complexities and lithologic variations. Syndepositional structures including folds, erosional surfaces, and density flows are also considered during the field work.

1.5.2. Mass specific magnetic susceptibility (χ)

Before measurement, all samples were crushed in order to reduce the effect of anisotropy on χ. Measurements were conducted using the Williams high-sensitivity χ Bridge in the rock magnetism laboratory at LSU; an extremely low, alternating field χ bridge that is calibrated relative to mass using standard salts (Swartzendruber, 1991). Ten grams of each sample were measured three times and the mean was calculated. Because it is very difficult to measure sample volume with high precision, mass-specific χ is generally considered the standard for magnetic susceptibility measurement (Ellwood et al., 2013). χ represents the bulk susceptibility of all minerals that are included in each sample (diamagnetic, paramagnetic and ferrimagnetic minerals (Nagata, 1961; Tarling and Hrouda, 1993). Because ferrimagnetic minerals are altered quickly after deposition in the marine environment (Karlin and Levi, 1983; Karlin and Levi, 1985) , and diamagnetic minerals have only weak, negative susceptibility, the χ signal in most marine sedimentary rocks comes mainly from paramagnetic minerals (Ellwood et al., 2013). Because detrital materials in the marine sediments are composed mainly of paramagnetic minerals (Ellwood et al., 2013), the χ variations account for the influx of these materials into the marine system and hence into the HRE. Laboratory measurements of χ are preferred over the field measurements in this study, because field measurements are affected by roughness of the measured surfaces, the surface area of the detector, the anisotropy of the outcrop, and the very low sensitivity of field instruments.

1.5.3. Percent carbonate ($CaCO_3$%) determined using carbonate digestion

Carbonate digestion has been performed using the method of Jones and Kaiteris (1983). 0.5 gm of each sample were crushed to a ~63μ size and dried for 1 hour at 110° C. 0.25 gm were carefully weighted and placed in the bottom of a reaction vessel, and 5 mm of 99% phosphoric acid was then placed in a side arm of the same vessel. The vessel was sealed and a vacuum produced within the vessel using a vacuum pump. The reaction was then initiated by tilting the reaction vessel, thus allowing the phosphoric acid in the vessel to mix with the sample. The reaction was allowed to continue for 1.5 hours, with agitation every 30 minutes. After the reaction ceased, the system was again pumped down and the pressure in the vessel measured before and after releasing the gas into the system. The difference between the two measurements represents the CO_2 gas pressure generated by the reaction. These results are calibrated for the volume difference between different reaction vessels as well as for both temperature, pressure before and after measurements (Jones and Kaiteris, 1983).

1.3. Results

$CaCO_3$% and χ data for the three sections are presented along with their normalized values in Figures 1.3 to 1.5. The raw data are presented as black dashed lines with all data points included, while the blue solid lines represent data smoothed using splines. The splined data for χ and $CaCO_3$% are normalized in order to better visualize the consistency between detrital/carbonate flux into the HRE. Splined data are preferred over the raw data in the normalization process, because much of the noise and high frequency cycles have been removed. In addition, as opposed to moving averages, splined data hold correct stratigraphic position for each data point. Normalized values are calculated for each data point using the following equation,

Norm. Value = (splined data point-MIN)/ (MAX-MIN), (1)

where MIN and MAX are the minimum and maximum values for the splined data set while MAX-MIN is the total range of the splined data. These curves start at the closest formation boundary associated with each section; the base of the Wheeler Formation for the GSSP and Marjum Pass sections, and the base of the Lincoln Peak Formation in the Packrat section. In order to better visualize all curves, χ is set to increase to the right, while the $CaCO_3$% is set to increase toward the left. These curves cover an interval that includes the Middle Cambrian uppermost part of the unnamed Stage Five and the lowermost part of the Drumian Stage. Twelve correlation points (CP), CP1 to CP12, and multiple arrows are added to both χ and $CaCO_3$% curves for correlation purposes (Figs. 1.6 and 1.7). The CPs highlight both peaks and troughs that have high correlation potential among the three sections examined, and the arrows mark the corresponding long-term trend of change. $CaCO_3$% is indicative of the amount of carbonate in each sample relative to the total mass of the sample. Non-carbonate percent is the inverse of $CaCO_3$%. Because χ variations represent detrital component; mainly the paramagnetic minerals that either flux into the marine system or result from diagenesis of the associated ferrimagnetic minerals after deposition in the marine environment (Nagata, 1961; Ellwood et al., 2000; Ellwood et al., 2006; Ellwood et al., 2013), non-carbonate diamagnetic materials can be extracted from the integration of χ and $CaCO_3$% curves (green area; Figs. 1.3, 1.4, and 1.5). These materials are likely to be either organic materials, quartz (sand/silt) or their mixture. Even though caution is required when interpreting this zone because χ is carried by wide spectrum of minerals that have wide χ range, such interpretation still valid through low χ intervals. In addition, its confidence increases if correlated among multiple equivalent sections.

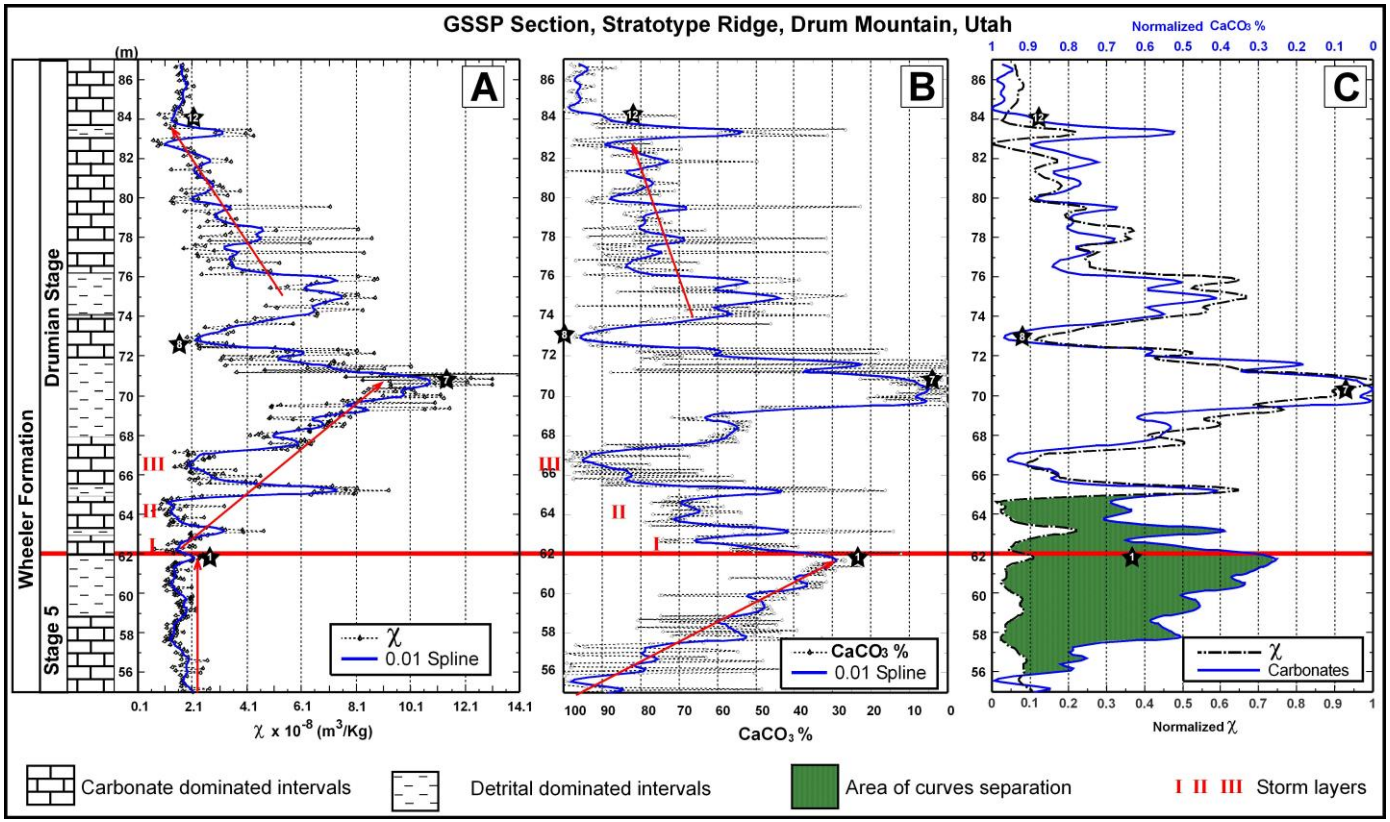

Figure 1.3. Three curves showing χ and $CaCO_3$% obtained for the GSSP section. A is the χ curve showing the raw χ data as a black dashed line with data points included, and smoothed data as a solid blue line. χ values increase to the right. B is the $CaCO_3$% curve showing $CaCO_3$% data as a black dashed line with data points included and smoothed data as a solid blue line. $CaCO_3$% values decrease to the right. C represents the normalized curves of χ and $CaCO_3$% plotted together. Only the smoothed data sets are normalized as noise and high frequency signal are removed. The direction of increase of χ and $CaCO_3$% are the same as in A and B. The base of the Drumian Stage is defined at 62 m (Babcock et al., 2007). The height for the GSSP is measured from the base of the Wheeler Formation. The numbered stars and red arrows in the A to C curves represent correlation points (CP1-CP12) and trends that are used for correlation purposes. Also the three events, I, II, and III, are high $CaCO_3$%, low χ, layers. The green coded interval represents an area where the $CaCO_3$% and χ curves are widely separated.

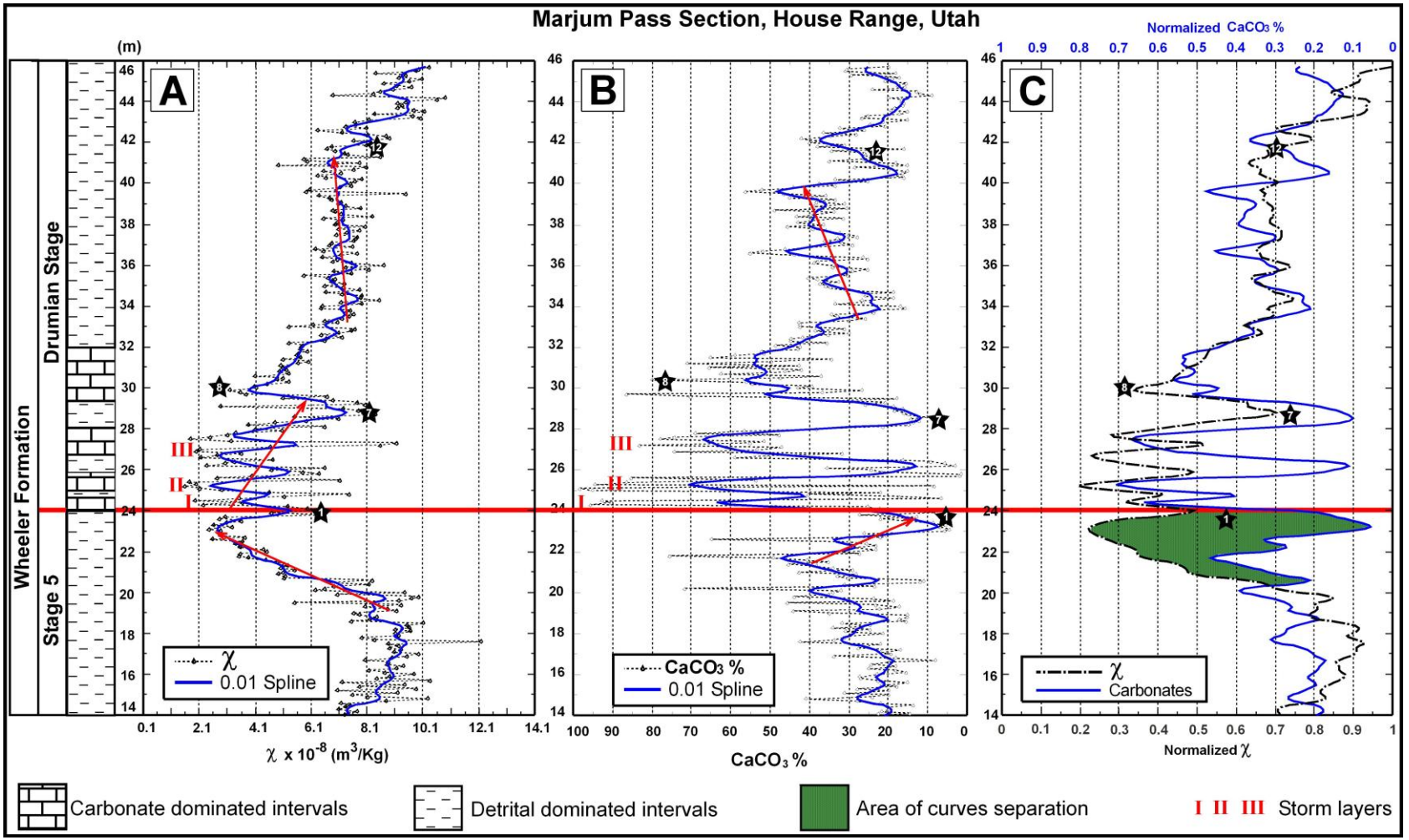

Figure 1.4. Three curves showing the results obtained from the Marjum Pass section. The features on the three curves, A to C, are illustrated in the caption of Figure 1.3. The base of Drumian Stage is defined at 24 m based on an ongoing research. Height for the Marjum Pass section is measured from the base of the Wheeler Formation.

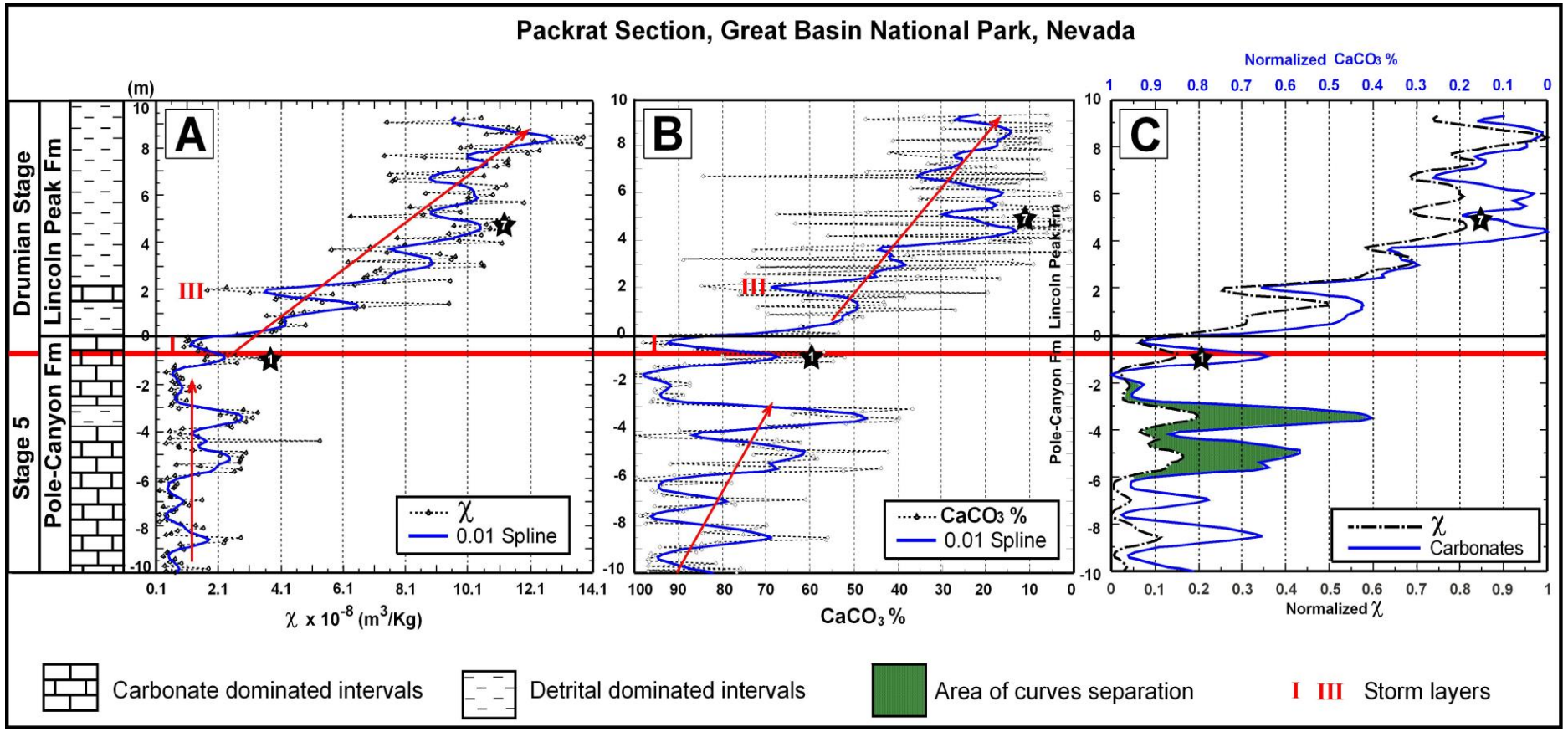

Figure 1.5. Three curves showing the results obtained from the Packrat section. The features on the three curves (A to C) are illustrated in the figure 1.3 caption. The base of Drumian Stage is defined here at ~0.8 m based on an ongoing research. Height for the Packrat section is measured from the base of the Lincoln Peak Formation.

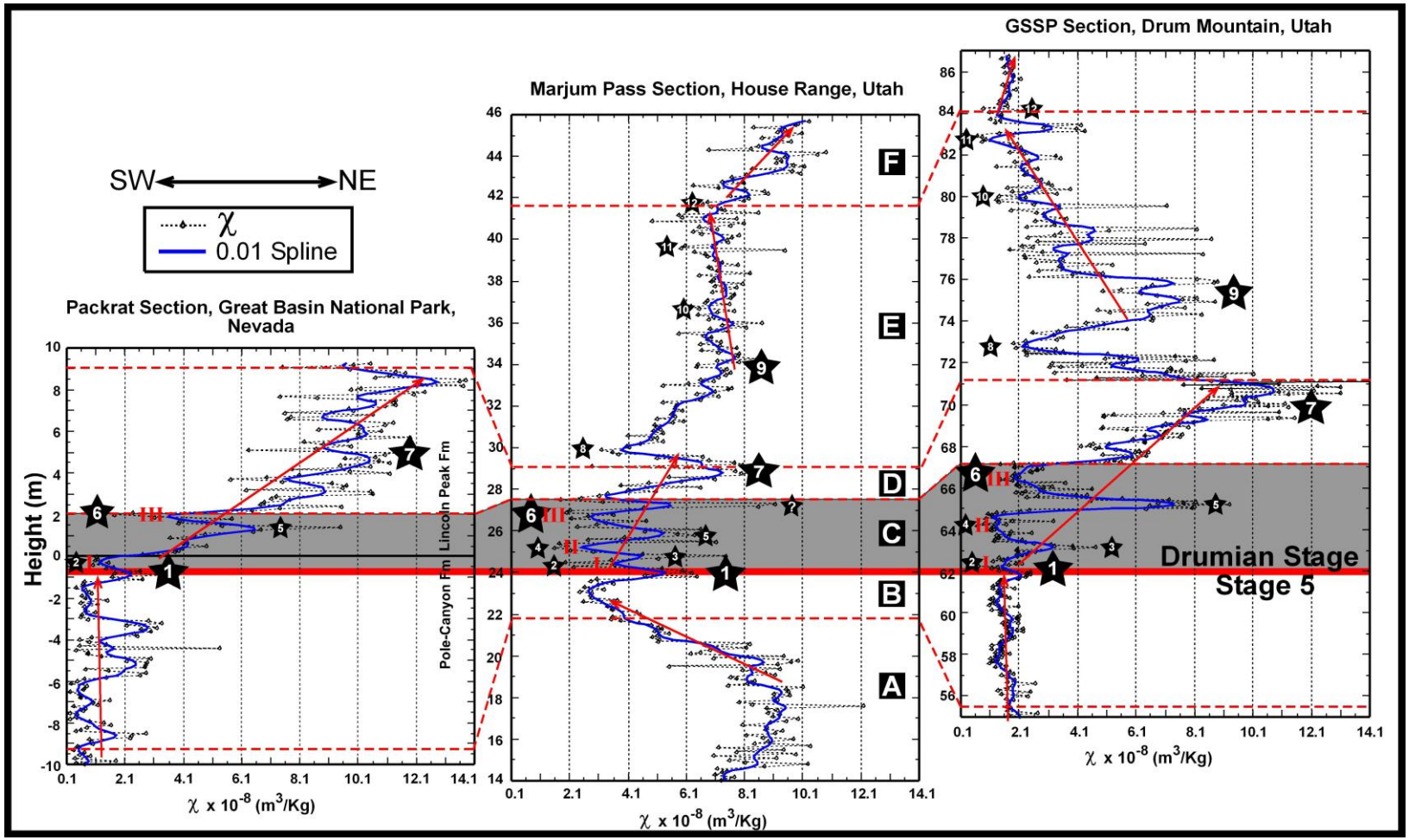

Figure 1.6. Three χ curves showing high resolution correlation among the studied localities; GSSP, Marjum Pass and Packrat Sections. The numbered stars represent correlation points (CPs) where the χ signal behaves the same among the three sections. Each CP represents either a peak or a trough on the χ curve. The six intervals, A to F, that are delimited by red dashed lines above and below the basal boundary of the Drumian Stage, have high correlation potential among the three sections. The red arrows represent the direction of change in the χ curve.

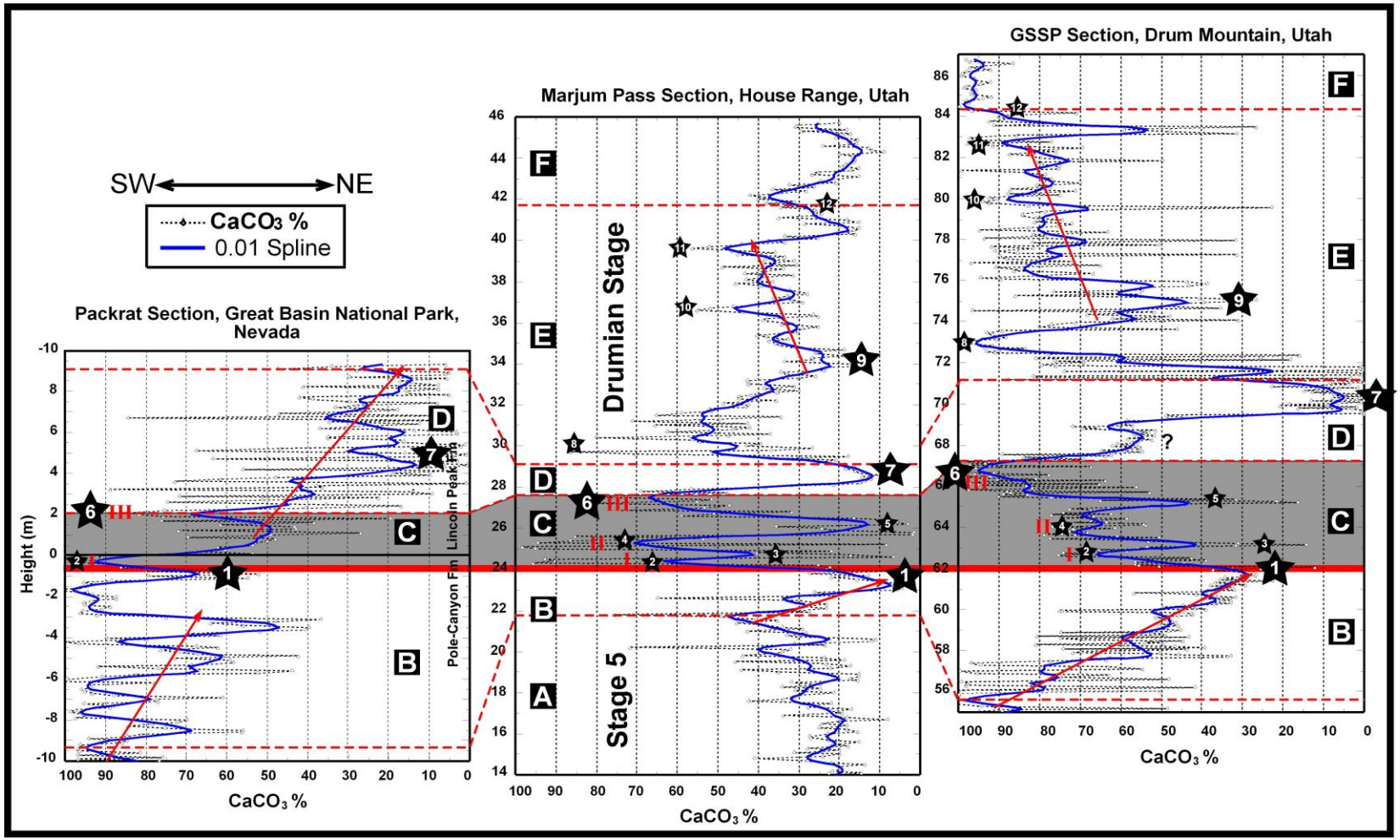

Figure 1.7. Three $CaCO_3$% curves showing high resolution correlation among the studied localities; GSSP, Marjum Pass and Packrat Sections. The numbered stars represent correlation points (CPs) where the $CaCO_3$% signal behaves the same among the three sections. Each CP represents either a peak or a trough on the $CaCO_3$% curve. The six intervals, A to F, that are delimited by red dashed lines above and below the basal boundary of the Drumian Stage, have high correlation potential among the three $CaCO_3$% curves. The red arrows represent the direction of change in the $CaCO_3$% curve.

At the GSSP section, the mean $CaCO_3$% value is ~62%, while the mean for χ is 3.66 x 10^{-8} m^3/kg (Fig. 1.3). In general, during Stage Five, χ values are generally low, ranging from 1.0 to 2.0 x 10^{-8} m^3/kg. The same low χ values are observed above the basal boundary in the Drumian GSSP section at 73 m and 84 m (CP8 and CP12; Fig. 1.3). Between these low values, the curve shows two long-term χ cycles. Above the base of the Drumian Stage, the first cycle exhibits a long-term χ increase up to 13.1 x 10^{-8} m^3/kg at 70.5 m, with the second cycle exhibiting a maximum at 75 m (~9.1 x 10^{-8} m^3/kg). Three low susceptibility intervals (I, II, and III) interrupt the long-term increase of the first cycle (Fig. 1.3). The carbonate curve shows a significant $CaCO_3$% increase from the first (I) to the third (III) interval. These intervals are separated by two χ highs or two $CaCO_3$% low zones (Fig. 1.3A and 1.3B). Figure 1.3C shows high consistency between χ and $CaCO_3$% normalized values, except for the lowermost interval where the $CaCO_3$% curve exhibits a monotonic, long-term decrease and the χ curve indicates very little change. This creates an area of separation in the two curves that increases in width toward the stage boundary. This separation area is color-coded (green) in this and the following diagrams (Figs. 1.3C, 1.4C, and 1.5C).

Stratigraphic timing indicates that the Marjum Pass section starts earlier and ends later than the lower and the upper limits of the GSSP section, respectively (Fig. 1.4). The mean $CaCO_3$% at Marjum Pass is ~33% while the mean χ is 6.7 x 10^{-8} m^3/kg. During Stage Five, the χ curve starts at a maximum value (~9.1x10^{-8} m^3/kg), but then decreases to very close to ~2.1x10^{-8} m^3/kg right below the base of Drumian Stage. The two cycles that are exhibited in the GSSP section are also identified in the Marjum Pass section as well. The upper and lower limits of these two cycles at the Marjum pass section are observed at 23, 30 and 42 meters above the base of

the Wheeler Formation (Fig. 1.4). The peaks of the two cycles remain slightly below 8.1x10^{-8} m^3/kg. A high frequency interval is observed above CP1 (24–30 m) and is correlated to the same interval in the GSSP section (CP1 to CP7) (Fig. 1.4). This interval includes three high carbonate pulses and shows an upward, long-term χ increase (Fig. 1.4A and 4B). Figure 1.1.4C shows high consistency between χ and $CaCO_3$% normalized values. Both χ and $CaCO_3$% decrease toward the basal boundary of Drumian Stage, again creating an area of separation, but one that is smaller than in its counterpart in the GSSP section (Fig. 1.4C).

The Packrat section covers most of the first cycle that has been observed in the other two sections (Fig. 1.5). The mean $CaCO_3$% of this section is ~59%, while the mean χ is 4.74 x 10^{-8} m^3/kg. During Stage Five, χ stays low, below the 2.1 x 10^{-8} m^3/kg gridline, with a few slight exceptions. Above the base of the Drumian Stage, χ shows a steady long-term increase up to ~13.5 x 10^{-8} m^3/kg (Fig. 1.5A). This behavior is correlative to the GSSP section, with the exception of the high-frequency interval and high $CaCO_3$% pulses that are absent in this section. Figure 1.5C shows the highest consistency between the χ and $CaCO_3$% normalized curves among the three sections. The normalized χ and $CaCO_3$% curves also separate below the Drumian Stage basal boundary (Figs. 1.3C, 1.4C, and 1.5C).

1.4. Correlation

Figures 1.6 and 1.7 represent χ and $CaCO_3$% correlation, respectively, among the three sections. In addition to the twelve correlation points, CP1 to CP12, that are traced partially from the GSSP through the Marjum Pass into the Packrat sections, six intervals, A to F, are also identified (Figs. 1.6 and 1.7). Each of these intervals has its own unique signal that can be traced along the NE-SW transect within HRE. Multiple arrows are placed in these figures on the χ and $CaCO_3$ curves

to highlight the long-term transgressive-regressive (T-R) cycles exhibited in these sections.

χ curves show high correlation potential above the CP7 between the GSSP and Marjum Pass sections. This interval represents ~1.5 cycles and includes CP8 to CP12. Correlation points CP1 through CP6 can be traced between the three sections (Fig. 1.6). This shaded interval is expanded in the GSSP section and more condensed at the Packrat section; the Marjum Pass section lies in between. Some of these correlation points (CP3, CP4, CP5 and CP6) are absent or have negligible thickness in the Packrat section (Fig. 1.6). CP7, on the other hand, shows a different thickness variation between the three sections, with highest thickness observed in the Packrat section, being thinnest in Marjum Pass section (Fig. 1.6). CP7 also has high correlation potential because, 1) its χ values start below 2.1 x 10^{-8} m^3/kg, 2) it peaks at the highest χ values in the GSSP and Packrat sections, but slightly below values in the Marjum Pass section, and 3) it is composed of ~5 short-term χ cycles in all sections. These cycles are represented as single data points in the Marjum Pass section because here it has condensed sedimentation at this level and because of its coarser sampling interval (10 cm). These short-term χ cycles are represented clearly in both the GSSP and Packrat sections (Fig. 1.6). Below CP1, the GSSP and the Packrat sections show high consistency with very little long-term χ change, while the Marjum Pass section shows a dramatic χ decrease.

The $CaCO_3$% highlights the three interruptive pulses (I, II, and III; Fig. 1.7). The correlation points CP2, CP4, and CP6 mark these pulses in the $CaCO_3$% curves. The $CaCO_3$% and thicknesses increase upward from the first (I) to the third (III) pulse. It is also observed that the thickness of each pulse decreases to the southwest until it vanishes (pulse II) or reduces markedly in its thickness (pulse III) in

the Packrat section (Fig. 1.7). Below CP1, $CaCO_3$% curves also highlight the overall decrease in $CaCO_3$% in the three sections, although χ curves through this interval show either no change or a χ decrease. Above CP7, there is high $CaCO_3$% correlation potential between the GSSP and the Marjum Pass sections.

1.5. Interpretation

Section location, sea level changes and physical processes that act on the carbonate platform contribute to how χ and the $CaCO_3$% signal behave in each section within the HRE. Eustatic, rather than relative, sea level changes are suggested here because the studied sections lie within an interval that is bounded by the second and third regional sequence boundaries, which are characterized by tectonic quiescence (Howley, 2010).

The normalized χ and $CaCO_3$% curves covary with each other during the studied interval in the three sections except for the interval below the base of Drumian Stage, where these parameters show an area of separation (Figs. 1.3C, 1.4C, and 1.5C). This area of separation decreases in size from the GSSP through the Marjum Pass to the Packrat sections, and marks the beginning of sea level rise. During this interval, $CaCO_3$% decreases in all sections, while χ records either decrease at the Marjum Pass section or very little change at both the GSSP and Packrat sections (Figs. 1.3C, 1.4C, and 1.5C). The non-carbonate materials seem to have less bulk susceptibility than expected, in contrast to the rest of the studied interval, suggesting the existence of non-carbonate diamagnetic materials such as organic matter and/or quartz grains at the beginning of the sea level rise. These materials could be the reason behind this area of separation as it may have dampened χ of the non-carbonate components. This indicates that χ signature is driven mainly by the non-carbonate materials within each sample. These

interpretation is in consistent with the work done by Ellwood and others (2000). They conclude that the paramagnetic and other detrital constituents mainly control the χ signal in marine sedimentary rocks.

The GSSP and Packrat sections have a more consistent χ signal and higher average $CaCO_3$% (~62% and ~59%) than the Marjum Pass section (~33%) (Figs. 1.6 and 1.7). This results from those sections being located closer to the carbonate platform than is the Marjum Pass section.

1.5.1. Drumian Stage GSSP Section

The GSSP section is close to the NE end of embayment trough where the embayment has minimal width and depth, in addition, the fault has minimal displacement compared with the Packrat section (Fig. 1.8). Therefore, the GSSP is surrounded by the carbonate platform, and is affected more than the other two sections by the advance and retreat of the carbonate factory. As the carbonate factory advances during sea level falls, the GSSP location is flooded with carbonates from the surrounding platform. The platform water currents that were driven by trade winds play an important role in delivering these carbonate sediments to the embayment. Laurentia was reported to straddle the equator during the middle Cambrian and was partly within the northerly trade winds belt during the Middle Cambrian (Scotese and Barrett, 1990; Elrick and Snider, 2002; Peng and Babcock, 2008; Howley, 2010). Therefore, the northern platform is likely to be the main source of carbonates into the HRE, with minor contribution from the southern platform during the time of maximum sea level fall.

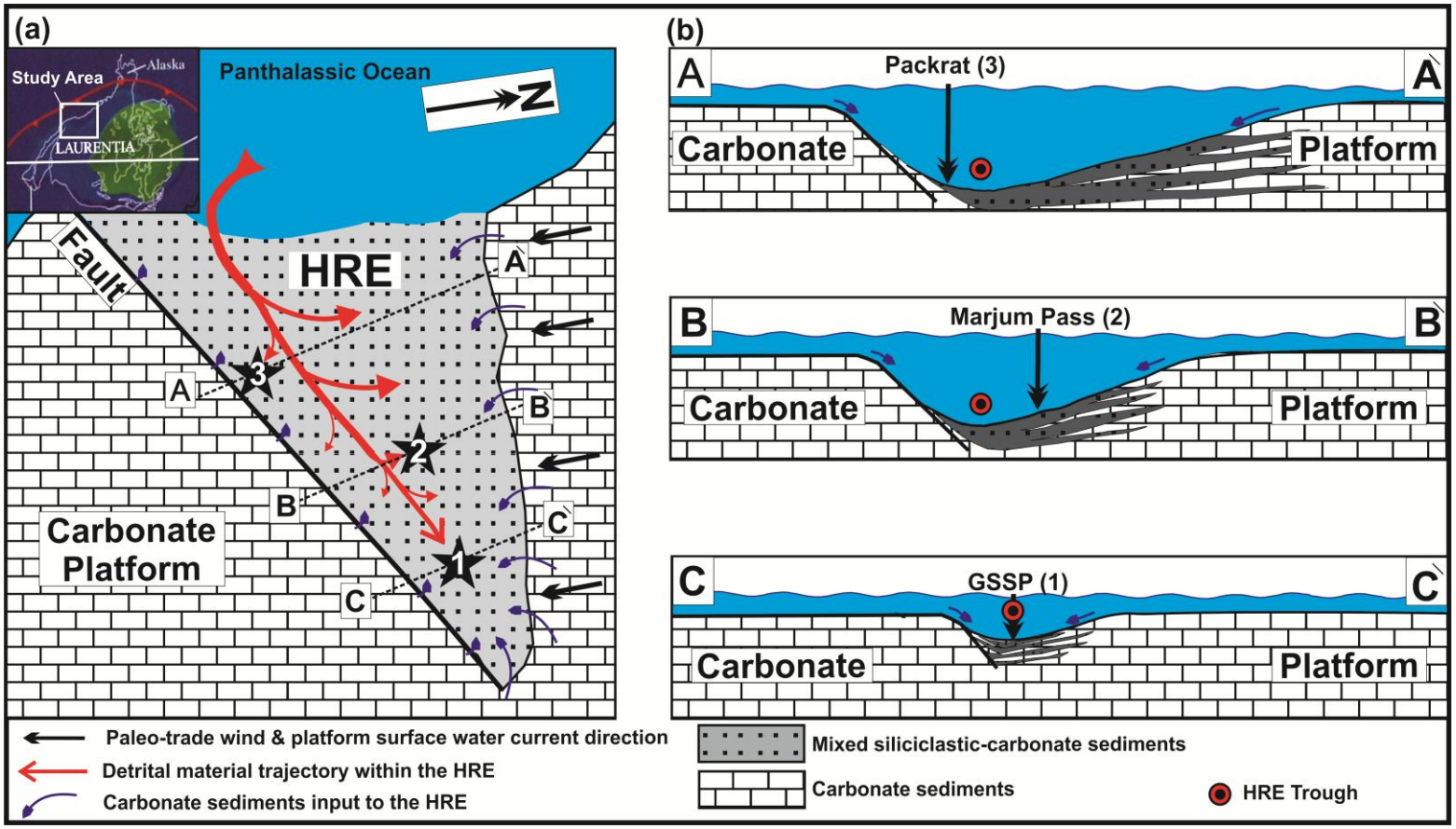

Figure 1.8. Hypothetical Paleogeographic map of the HRE showing facies distribution, sediment trajectories, and the location of the three sections relative to the embayment edge and trough. (a) A plan view of the embayment showing how detrital materials and carbonate are delivered to the embayment. Detrital materials are channelized first through the trough (the main red line) and spread to the northern and southern ramps (red arrows that split away from the main red line). Blue arrows around the embayment show that the carbonate dominated sediments have been delivered to the HRE across its edges. The present North direction and the direction of both paleo-trade winds and the platform surface currents are shown on the map. (b) Three cross sections showing the relative depth and width of the HRE at each section. Also shown is the location of each section relative to the embayment edge and trough.

1.5.2. Marjum Pass Section

The Marjum Pass section is located on the downslope side of the northern ramp (Fig. 1.8), where it is far from the embayment edge and thus receiving less carbonates than the other two sections. It has ~40% $CaCO_3$% during maximum sea level fall (at 22 m; Fig. 1.7) when the other two sections have more than 90% carbonates at the same time (Fig. 1.7). $CaCO_3$% analysis indicates that the Marjum Pass section was closer to the trough than to the northern edge of the HRE because it received more detrital material than carbonates (Fig. 1.7). The detrital materials are provided to the Marjum Pass section from the HRE mouth through the HRE trough, and its carbonates from either the northern carbonate platform during storm events or as pelagic carbonates. The gradual change in the upper and lower parts of the χ curve records gradual lithological variations while the middle part records frequent lithological changes (Fig. 1.6).

1.5.3. Packrat Section

The Packrat section lies on the southern ramp very close to the normal fault (Fig. 1.8) where carbonates are shed off the southern platform across the fault scarp to the section during the maximum sea level fall and early sea level rise. Accordingly, the southern platform is the main source of carbonates into the Packrat section because it is not likely that these carbonates cross the northern ramp and the trough to the section. Likewise, the Packrat section is closer to the southwest part of the HRE (Figs. 1.2 and 1.8), where the depth and width of the embayment and the fault displacement are at their maximum, producing more space to accommodate the north-coming carbonate sediments on the northern ramp. Syndepositional sliding, gliding and folding structures (Figs. 1.9 and 1.10), at or close to the section, indicate

that it is seated on the high angle surface of the southern ramp. Syndepositional folding suggests that it is a downslope section, close to the embayment trough.

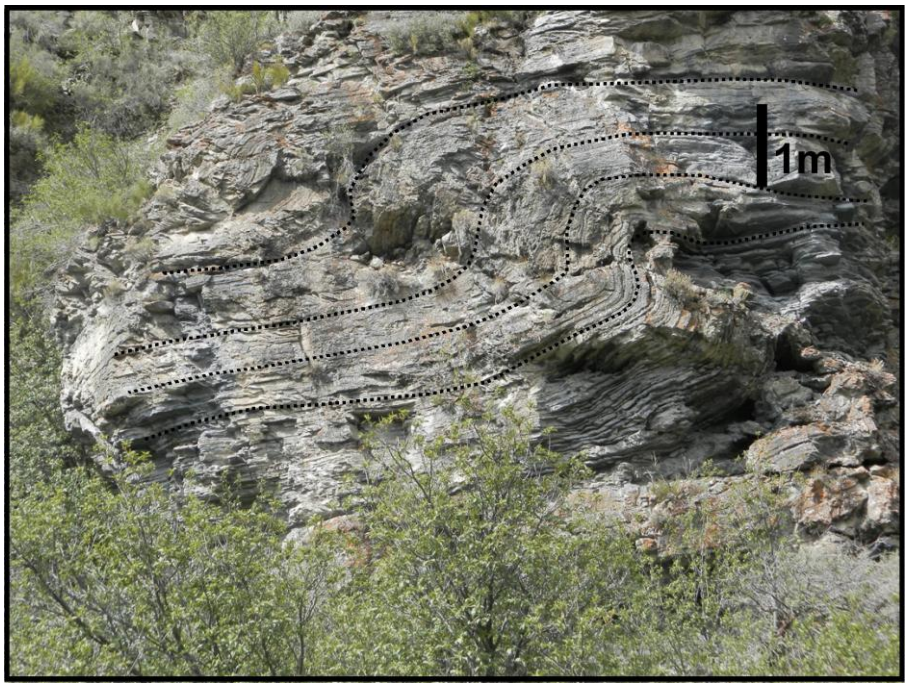

Figure 1.9. Photographs showing a syndepositional fold close to the Packrat section. The black bar represent ~1 meter scale.

Figure 1.10. Photographs showing a syndepositional density flow structure in the lower part of the Packrat section. The thickness of this layer varies with an average of ~0.5 m. The arrow indicates a boulder that was picked up by this downslope density flow and encased in the middle of this layer.

1.5.4. Integration of Sections and Facies Interpretation

Below CP1 (Fig. 1.7), both the GSSP and the Packrat sections represent the last phase of sea level fall, where $CaCO_3$% is at its maximum (>90%) at the boundary between intervals A and B (Fig. 1.7), and the earlier stage of sea level rise, where the $CaCO_3$% signal decreases (interval B; Fig. 1.7). The Marjum pass section covers the same interval (B), in addition to, the late stage of the preceding sea level rise and the entire sea level fall (Interval A; Figs. 1.6 and 1.7). The late stage of sea level rise is represented at the base of the Marjum Pass section where the $CaCO_3$% is at its minimum (~20%). During interval A, the sea level fall is characterized by increasing $CaCO_3$% values, while χ decreases during this time (Figs. 1.6 and 1.7).

Sea level continues to rise above CP1, leaving all sections at greater depths. Therefore, χ signal increases at the expense of $CaCO_3$% signal until maximize at CP7 (Fig. 1.6) reflecting the increase in terrigenous materials deposited during intervals B, C and D (Figs. 1.6 and 1.7). Three carbonate layers (CP2, CP4, and CP6) interrupt this long-term increase. These layers are interpreted as three separate storm events (I, II, and III) that eroded the surrounding carbonate platform and deposited their sediment within the slope and basinal area of the HRE (Fig. 1.8). This interpretation is supported by multiple observations; 1) the $CaCO_3$% of each storm layer is higher than its bounding layers and is well correlated among the studied sections. Also the shaded interval, C, that encompasses the three storm layers has higher $CaCO_3$% than its bounding B and D intervals, 2) the storm layers are observed during sea level rise where $CaCO_3$% is expected to decrease and χ is expected to increase, 3) they interrupt the long-term χ increase that maximizes at CP7 and accounts for detrital material increase above the base of the Drumian Stage (Fig. 1.6). They also interrupt the long-term $CaCO_3$% decrease that starts at

the base of interval B and minimizes at CP7 at the GSSP and Packrat sections (Fig. 1.7). 4) χ curve exhibits an overall smooth transition from high to low χ values, and vice versa, in the Marjum Pass section except for the interval across these storm deposits where high frequency χ signal is observed. This interval has the highest amplitude and frequency $CaCO_3$% signal in the Marjum Pass section reflecting high facies variation (Figs. 1.6 and 1.7), 5) the thickness of each storm layer decreases basinward, away from the carbonate platform and the HRE edge. Their thicknesses decrease from the GSSP section, shallow trough section, through the Marjum pass section, the lower slope section of the northern ramp, to the Packrat section, the lower slope section of the southern ramp (Fig. 1.8), and 6) an erosional surface is observed at the base of the first storm layer at the GSSP section (Fig. 1.11). This surface is located at 62 m above the base of the Wheeler formation and was recorded as a stage boundary (Babcock et al., 2004; Babcock et al., 2007; Brett et al., 2009). These storm layers were left undisturbed because bioturbation remained insignificant during the middle Cambrian (Gingras and Konhauser, 2015). In addition, it was reported that bioturbation was suppressed during multiple intervals in the Middle-Cambrian Wheeler Formation because the HRE is reported to have anoxic poorly-oxygenated deep water where the Oxygen Minimum Zone (OMZ) was well developed (Rogers, 1984; Rees, 1986; Savrda and Bottjer, 1987; Elrick and Snider, 2002; Gaines and Droser, 2003; Gaines and Droser, 2005; Gaines et al., 2005; Halgedahl et al., 2009). In the GSSP section, these storm events may be confused with normal deposition, even at high resolution sampling, because the $CaCO_3$% has higher variations and higher frequency through the whole section. Widely-spaced sampling and coarse correlation add more challenges in identifying these storm layers.

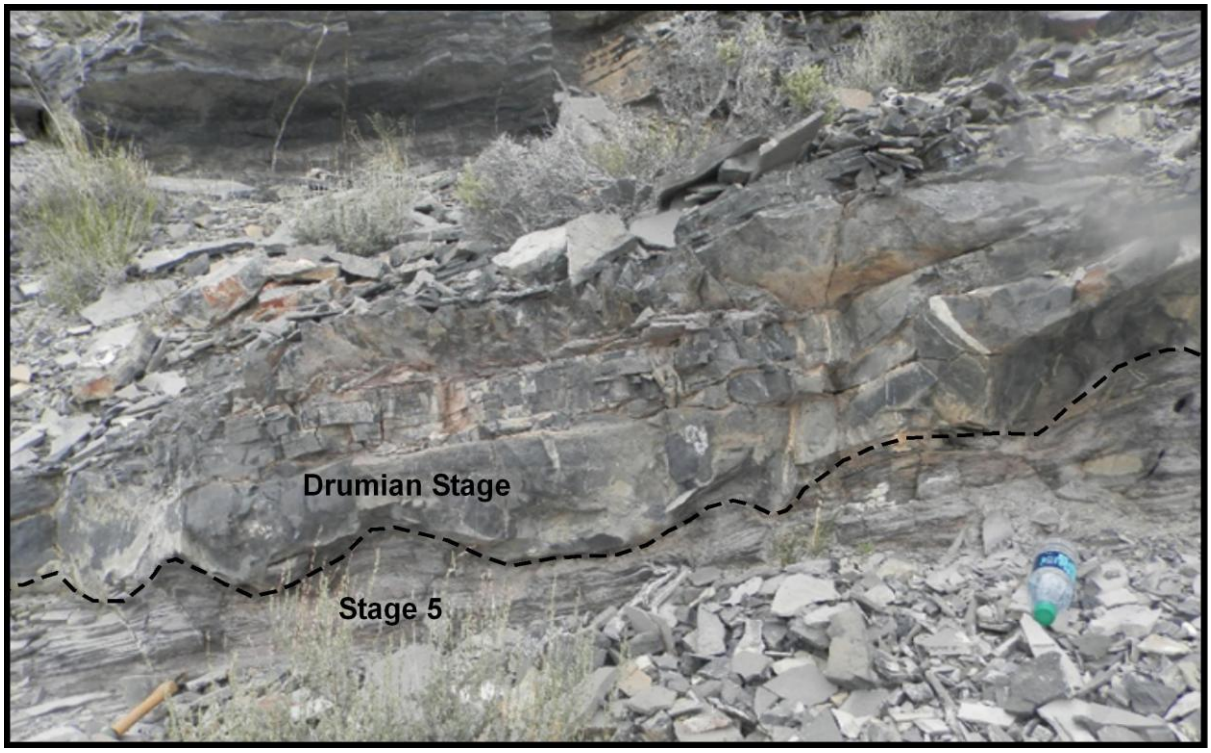

Figure 1.11. Photographs showing the basal boundary for the Drumian Stage at the GSSP section. Ripple marks predominate this erosional surface as it represents the base of the first storm layer (CP2) in Figure 1.7. Arrows indicate this erosional surface.

Multiple studies on the GSSP section refer to these interruptive storm layers as three calcisiltite layers that are composed of silt-size carbonate grains (Babcock et al., 2004; Babcock et al., 2007; Brett et al., 2009). Brett et al. (2009) interpret each calcisiltite bed as either a single storm deposit or a turbidity current event. This is in consistent with the interpretation presented here, where the three separate storm events eroded the carbonate platform, delivered the storm agitated sediments into the HRE slope and basinal areas, and triggered three separate turbidity currents. The studied interval lies within the Wheeler Formation that has been deposited in ramp-to-basin environment below the storm wave base (Robison, 1999; Babcock et al., 2004; Howley et al., 2006; 2007). Therefore, the turbidity currents traveled southward downslope the northern HRE ramp following the platform surface-water-currents that were driven mainly by the northerly trade winds. The turbidity currents are expected to be erosive in the upslope areas as it conserve its momentum close

to the northern HRE edge not too far below the storm wave base. They lost their inertia and exhausted downslope by settling of their suspended sediments along the ramp, and died out at or very close to the HRE trough. In addition, the low slope angle of the northern HRE ramp (<1° Palmer, 1971; Elrick and Snider, 2002) precluded such currents from maintaining their inertia under their own gravity. Field observations as well as χ and $CaCO_3$% curves support this interpretation. An erosional surface is observed at the base of the first storm layer in the shallow GSSP section that is close to the carbonate platform and the HRE edge. Unfortunately, the base of the second (II) and third (III) storm layers are not well exposed in the GSSP section. Also, the thickness of each storm layer decreases downslope because most of storm sediments were deposited in the upslope areas close to the northern edge (Figs. 1.6 and 1.7). Moreover, the coarse sediments, calcisiltite, has been reported in the shallow HRE GSSP section (Babcock et al., 2007; Brett et al., 2009), while finer sediments are observed in the lower slope Marjum Pass section.

The storm events cause disturbances along the southern edge of the embayment at the fault scarp, initiating some turbidity currents. Although the southern ramp has a higher slope angle than the northern one, the storm events have negligible thickness (event III) or are absent (event II), because the trade-wind driven surface currents move the storm sediments southward away from the HRE (Figs. 1.1 and 1.8). Also, the location of the Packrat section, being at the bottom of the southern ramp, makes it difficult for such turbidity currents to reach that location. Only the first event (I) is observed because the first storm event succeeded in moving the unstable deposits down the southern ramp and across the fault scarp.

Even though the GSSP and Packrat sections are closer to the embayment edge, than is the Marjum Pass section (Fig. 1.8), $CaCO_3$% is reduced more

dramatically at the GSSP (0-5%) and Packrat (~5%) sections than at Marjum Pass (10-20%) during the interval of maximum sea level stand (interval D; Fig. 1.7). In addition, detrital materials increased more dramatically in the GSSP (χ >12.1 x 10^{-8} m^3/kg) and the Packrat (χ ~13.1 x 10^{-8} m^3/kg) sections than in Marjum Pass (χ ~8.1x10^{-8} m^3/kg) at this time (interval D; Fig. 1.6). Moreover, the Packrat section is more expanded than the GSSP, and the Marjum Pass is the most condensed during this interval (Figs. 1.6 and 1.7). This dictates the source and the trajectory of detrital materials within the HRE. The detrital materials are provided to the embayment through the HRE mouth, where it connects to the deep open water of the Middle Cambrian Panthalassic Ocean (Fig. 1.8). They are channelized, first through the trough, and then they spread out to the northern and southern ramps of the HRE during sea level rise (Fig. 1.8). It is not likely that these terrigenous sediments were delivered to the embayment from the main continent by aeolian processes (Dalrymple et al., 1985), or through bypass zones that cut through the middle Cambrian extensive carbonate shelf (Hintze and Robison, 1975; Rogers, 1984; Rees, 1986), because the adjacent platform sections are composed of pure carbonates, in addition, the bypass zones are not recorded anywhere in Utah, southern Idaho or southern Nevada (Elrick and Snider, 2002). Therefore, it has been argued that terrigenous sediments were loaded into deep-water currents from far north (near the British Columbia–North-West Territories border) and brought into the HRE (Aitken, 1978; Aitken, 1997; Elrick and Snider, 2002).

Consequently, sections that are at or very close to the trough, and the HRE mouth, receive more detrital material at maximum sea level stand, than do those away from the trough, and the HRE mouth, on either the northern or the southern ramps (Fig. 1.8). These interpretations refine the position of each section; the GSSP

section is at the NE end of the embayment trough, the Marjum Pass section is on the downslope side of the northern ramp, far enough from the trough to receive less terrigenous materials than the other two sections, and the Packrat section is on the southern ramp close to the trough (Fig. 1.8). Syndepositional structures including folds, erosional surfaces and debris flows at or close to the Packrat section refine its position (Figs. 1.9 and 1.10). In summary, the GSSP and the Packrat sections are closer to both the embayment edge and trough, than is the Marjum Pass section because the latter was located on wide, gently sloping, northern ramp (Fig. 1.8). The approximate slope angle of the ramp is <1^{o} (Palmer, 1971; Elrick and Snider, 2002). Therefore, they have higher facies variations than is the Marjum Pass section. During maximum sea level fall, at the base of the interval B, the advance of the carbonate factory flooded the two sections reflecting >90% of $CaCO_3$% (Figs. 1.6 and 1.7). During maximum sea level rise, at CP7, they have enough accommodation space not only to accommodate the existing sediments but also to accommodate more sediments as the carbonate factory retreats, thus recording the lowest $CaCO_3$% and the highest terrigenous materials input in both sections at CP7 (Figs. 1.6 and 1.7). In contrast, the Marjum Pass section exhibit a smooth transition where a balance between the carbonate and detrital input is achieved. The only exception for the smooth transition occurs during the storm interval where high amplitude and high frequency facies variation are observed (Interval C; Figs. 1.6 and 1.7).

Above the CP7, both the GSSP and Marjum Pass sections have high correlation potential during intervals E and F (Figs. 1.6 and 1.7). These intervals represent deposition under normal circumstances where no storm events are observed. The eustatic sea level fluctuations drive the carbonate factory advance and retreat and account for the associated facies variation. The position of each

section relative to the embayment edges and trough, accounts for the difference in terrigenous (χ) and $CaCO_3$% at any location on those curves. CP12 records the maximum sea level fall where the $CaCO_3$% is a maximum at the GSSP, resembling the starting point of the section. Also CP12 marks the beginning of a sea level rise where χ curves show the start of the next cycle.

1.6. Discussion

Sediments in the HRE were delivered either under normal conditions, where deposition was controlled mainly by eustatic sea level changes, or under storm events, where deposition was controlled by the physical processes that act on the carbonate platform. According to the results obtained in this study, the location of each studied section, relative to the embayment edge and trough (Fig. 1.8), accounts for the differences in both χ and $CaCO_3$% signals between the three sections. The GSSP is a shallow trough section that is located at the very NE end of the HRE (Fig. 1.8) where it is surrounded mostly by the carbonate platform. Therefore, it was most heavily affected by the carbonate factory advance and retreat. It was flooded by carbonates during sea level fall and by detrital material during maximum sea level rise (CP7). The Packrat is a lowerslope section along the southern ramp where the seafloor had a higher slope angle than did the northern ramp. Therefore, syndepositional fold structures and debris flows are observed (Figs. 1.9 and 1.10) at or very close to the section. Carbonates were shed off the fault scarp, resulting in a carbonate-dominated interval during maximum sea level fall or early sea level rise. It was quickly replaced by a detrital-dominated interval, either during sea level rise or at the maximum sea level rise, because the Packrat section is a downslope section that is close to the HRE trough. The section at Marjum Pass is a downslope section on the northern ramp where an input balance of both carbonate and detrital materials

is recorded. Therefore, both χ and $CaCO_3$% have smooth transitions from high to low values and vice versa. This makes the Marjum Pass ideal for identifying eustatic sea level changes, because these data sets respond smoothly to lithologic variations.

Physical processes that act on the shelf have their own signal that are superimposed on the overall χ and $CaCO_3$% signals. CP2, CP4 and CP6 are three storm layers that were deposited from three separate turbidity currents, which, in turn, are controlled by three separate storm events (I, II, and III). They have high $CaCO_3$% (> 70%) that increase upward from the first to the third storm event layers in both the GSSP and Marjum Pass sections. The thickness of each layer decreases laterally toward the HRE trough because the turbidity current is gradually exhausted by settling of suspended load (Figs. 1.6 and 1.7). The thicknesses, and both $CaCO_3$% and χ signals variations of these storm layers result from the southwest width and depth increase of the HRE, and the location of each section relative to the embayment edge (Figs. 1.6, 1.7 and 1.10). The storm layers disappear or are minimized in thickness in the Packrat section, because of its location on the southern ramp close to the trough. In addition, the trade-winds driven water-currents drove the storm agitated sediments southward away from the embayment.

The source of terrigenous and carbonate materials were investigated using χ and $CaCO_3$% curves by observing the thicknesses and signal changes of the corresponding layers. This relationship is better observed during a time of maximum sea level rise and fall, where maximum terrigenous and carbonate influx into the HRE are best recovered. It is observed that carbonate-dominated intervals during maximum sea level fall or early sea level rise (interval B; Fig. 1.7) show an inverse relationship to that of terrigenous-dominated intervals during maximum sea level rise

(interval D; Fig. 1.6), when the location of each section is taken into account. The location of each section relative to the HRE edge is a key factor that helps in identifying the carbonate sediment source. Likewise, the location of each section relative to the HRE trough is a key factor that helps in identifying the terrigenous sediment source.

During Stage Five, carbonate layers in the shallow GSSP section, closer to the HRE edge, are expanded, while the deeper Marjum Pass section, farther from the embayment edge, has condensed carbonate layers (Fig. 1.6). The decrease in thickness of the carbonate-dominated intervals away from the HRE edge during maximum sea level fall and/or early sea level rise, is supported by the Packrat section. Although the Packrat section represents a deeper section, it exhibits an expanded section during Stage Five (interval B) because it was located closer to the HRE edge than was the Marjum Pass section. Consequently, the carbonate platform is considered as the main source of carbonate sediments into the HRE. More support for this interpretation is provided by the three storm layers, CP2, CP4, and CP6. The thickness of each layer decreases away from the HRE edge, from the GSSP to the Marjum Pass sections (Fig. 1.7).

During maximum sea level rise (interval D; Fig. 1.6), the Packrat section, on the SW side the HRE trough, has more expanded section than does the GSSP section, which is at the NE end of the trough. At maximum sea level rise, both sections had enough accommodation space to allow deposition of more sediment than already existed. The decrease of the terrigenous sediment in the NE direction, and away from the trough, is supported by observations at the Marjum Pass section. Although it was deposited in deeper water than the GSSP section, it is more condensed through the same intervals because it was farther from the trough than

the other two sections. This interpretation follows because the terrigenous sediment was being provided from the SW side of the embayment and channelized through the HRE trough to the GSSP section (Fig. 1.10). Some of this sediment settled in the trough and on the two ramps while on its way to the GSSP location.

The first, CP2, second, CP4, and third, CP6, storm layers can be traced from the GSSP through the Marjum Pass to the Packrat sections. These layers, then, represent chronostratigraphic markers that easily facilitate the correlation among the three studied sections and help in tracing important surfaces from one section into the other.

1.7. Conclusion

Even though the House Range Embayment (HRE) facies are composed of varying of carbonate/detrital ratios, the main lithological variations seem to follow broad facies patterns. Carbonate sediments are maximized at the HRE edges and decrease inward, and detrital materials are maximized along the HRE trough and decrease outward. In between these two end points, the carbonate/detrital ratio varies according to: 1) the position of each section within the HRE, 2) the eustatic sea level fluctuations during sediment deposition, and 3) the physical processes that act on the carbonate platform around the HRE. This carbonate/detrital ratio increases during sea level falls and storm events, and maximizes during times of maximum sea level fall. It also decreases during sea level rise, and minimizes during times of maximum sea level rise.

The Drumian Stage Global boundary Stratotype Section and Point (GSSP) in the Drum Mountains, Utah, is a shallow trough section that is located close to the northeast end of the HRE, and is surrounded by a western Laurentia carbonate platform. It is a carbonate-dominated section because the width and depth of the

HRE are at their minimum where the GSSP is located. Carbonates are shed off the surrounding carbonate platform to the GSSP locality. A second, coeval section, the Marjum Pass section in the House Range, Utah, is a lower-slope section found along the northern HRE ramp, where the width and depth of the HRE are higher than at the GSSP section. Marjum Pass is a detrital-dominated section that received its detrital components from the HRE mouth through the HRE trough, and its carbonates from either the northern carbonate platform during storm events or as pelagic carbonates. The Packrat section is a lower-slope section of the southern HRE ramp where the width and depth of the HRE were at their maximum. It is a mixed section; carbonate-dominated in its lower half and detrital dominated in its upper half. It received its carbonates from the southern portion of the carbonate platform and detrital materials from the HRE mouth through the HRE trough.

Physical processes that acted on the shelf had their own signal that are superimposed on the overall magnetic susceptibility (χ) and $CaCO_3$% signals. CP2, CP4 and CP6 are three storm-generated turbidite layers that were deposited from three separate turbidity currents, which, in turn, were controlled by three separate storm events (I, II, and III). They have high $CaCO_3$% (> 70%) that increases upward from the first to the third turbidite in both the GSSP and Marjum Pass sections. In addition, the thickness of each layer decreases laterally toward the HRE trough due to turbidity current exhausted. These three turbidite layers represent chronostratigraphic markers that make it possible to correlate among the three studied sections and help in tracing important surfaces from one section into the others.

1.8. References

Aitken, J.D., 1978. Revised models for depositional grand cycles, Cambrian of the southern Rocky Mountains, Canada. Bulletin of Canadian Petroleum Geology, 26(4): 515-542.

Aitken, J.D., 1997. Stratigraphy of the Middle Cambrian plat-formal succession, southern Rocky Mountains. Geol. Surv. Can. , 398: 322

Babcock, L.E., Rees, M.N., Robison, R.A., Langenburg, E.S., Peng, S., 2004. Potential Global Standard Stratotype-section and Point (GSSP) for a Cambrian stage boundary defined by the first appearance of the trilobite Ptychagnostus atavus, Drum Mountains, Utah, USA. Geobios, 37(2): 149-158.

Babcock, L.E., Robison, R.A., Rees, M.N., Peng, S., Saltzman, M.R., 2007. The global boundary stratotype section and point (GSSP) of the Drumian Stage (Cambrian) in the Drum Mountains, Utah, USA. Episodes, 30(2): 85-95.

Brady, M.J., Koepnick, R.B., 1979. A Middle Cambrian platform-to-basin transition, House Range, West central Utah. Geology Studies, 26, Part 1: 1-7.

Brett, C.E., Allison, P.A., DeSantis, M.K., Liddell, W.D., Kramer, A., 2009. Sequence stratigraphy, cyclic facies, and lagerstätten in the Middle Cambrian Wheeler and Marjum Formations, Great Basin, Utah. Palaeogeography, Palaeoclimatology, Palaeoecology, 277(1-2): 9-33.

Dalrymple, R.W., Narbonne, G.M., Smith, L., 1985. Eolian action and the distribution of Cambrian shales in North America. Geology [Boulder], 13(9): 607-610.

Dickinson, W.R., 1981. Plate tectonics and the continental margin of California. in Ernst, W.G., ed., The Geotectonic Development of California, Prentice-Hall, Upper Saddle River, New Jersey: 1–28.

Ellwood, B.B., Balsam, W.L., Roberts, H.H., 2006. Gulf of Mexico sediment sources and sediment transport trends from magnetic susceptibility measurements of surface samples. Marine Geology, 230(3-4): 237-248.

Ellwood, B.B., Crick, R.E., El Hassani, A., Benoist, S.L., Young, R.H., 2000. Magnetosusceptibility event and cyclostratigraphy method applied to marine rocks; detrital input versus carbonate productivity. Geology [Boulder], 28(12): 1135-1138.

Ellwood, B.B. et al., 2013. Testing high resolution magnetic susceptibility and gamma radiation methods in the Cenomanian-Turonian (Upper Cretaceous) GSSP and near-by coeval section. Palaeogeography, Palaeoclimatology, Palaeoecology, 378: 75-90.

Elrick, M., Snider, A.C., 2002. Deep-water stratigraphic cyclicity and carbonate mud mound development in the Middle Cambrian Marjum Formation, House Range, Utah, USA. Sedimentology, 49(5): 1021-1047.

Gaines, R.R., Droser, M.L., 2003. Paleoecology of the familiar trilobite Elrathia kingii; an early exaerobic zone inhabitant. Geology [Boulder], 31(11): 941-944.

Gaines, R.R., Droser, M.L., 2005. New approaches to understanding the mechanics of Burgess Shale-type deposits; from the micron scale to the global picture. Sedimentary Record, 3(2): 4-8.

Gaines, R.R., Kennedy, M.J., Droser, M.L., 2005. A new hypothesis for organic preservation of Burgess Shale taxa in the middle Cambrian Wheeler Formation, House Range, Utah. Palaeogeography, Palaeoclimatology, Palaeoecology, 220(1-2): 193-205.

Gingras, M., Konhauser, K., 2015. The Cambrian evolution of burrowing species is thought to have facilitated sediment mixing. However, sediment fabrics suggest that bioturbation remained insignificant until the appearance of more efficient sediment mixer in Silurian Nature Geoscience, 8: 825-826.

Halgedahl, S.L., Jarrard, R.D., Brett, C.E., Allison, P.A., 2009. Geophysical and geological signatures of relative sea level change in the upper Wheeler Formation, Drum Mountains, west-central Utah; a perspective into exceptional preservation of fossils. Palaeogeography, Palaeoclimatology, Palaeoecology, 277(1-2): 34-56.

Hintze, L.F., 1988. Geologic history of Utah. Brigham Young University geology studies. Special publication: 7. Provo, Utah : Dept. of Geology, Brigham Young University, c1988.

Hintze, L.F., Robison, R.A., 1975. Middle Cambrian stratigraphy of the House, Wah Wah, and adjacent ranges in western Utah. Geological Society of America Bulletin, 86(7): 881-891.

Howley, R.A., 2010. Sequence and chemostratigraphy of the Middle Cambrian succession in Nevada and Utah, United States.

Howley, R.A., Jiang, G., 2007. Sequence stratigraphy of the Middle Cambrian succession in eastern Nevada and western Utah; evidence for the initiation and termination of the House Range embayment. Abstracts with Programs - Geological Society of America, 39(6): 150-150.

Howley, R.A., Jiang, G., 2010. The Cambrian Drumian carbon isotope excursion (DICE) in the Great Basin, western United States. Palaeogeography, Palaeoclimatology, Palaeoecology, 296(1-2): 138-150.

Howley, R.A., Rees, M.N., Jiang, G., 2006. Research paper: Significance of Middle Cambrian mixed carbonate-siliciclastic units for global correlation: southern Nevada, USA. Palaeoworld, 15: 360-366.

Jones, G.A., Kaiteris, P., 1983. A vacuum-gasometric technique for rapid and precise analysis of calcium carbonate in sediments and soils. Journal of Sedimentary Petrology, 53(2): 655-660.

Karlin, R., Levi, S., 1983. Diagenesis of magnetic minerals in recent haemipelagic sediments. Nature, 303(5915): 327-330.

Karlin, R., Levi, S., 1985. Geochemical and sedimentological control of the magnetic properties of hemipelagic sediments. Journal of Geophysical Research: Solid Earth (1978–2012), 90(B12): 10373-10392.

Langenburg, E.S., 2003. The Middle Cambrian Wheeler Formation; sequence stratigraphy and geochemistry across a ramp-to-basin transition, United States.

Nagata, T., 1961. Rock magnetism. Tokyo, Maruzen Co., 1961. Rev. ed.

Palmer, A.R., 1965. Trilobites of the late Cambrian Pterocephaliid biomere in the Great Basin, United States. Geological Survey (U.S.). Professional paper: 493. Washington, U.S. Govt. Print. Off., 1965.

Palmer, A.R., 1971. The Cambrian of the Great Basin and adjacent areas, western United States. Wiley-Intersci., London-New York, International, pp. 1-78.

Peng, S.C., Babcock, L.E., 2008. Cambrian Period. in Ogg, J.G., Ogg, G., and Gradstein, F.M., eds., A Concise Geologic Time Scale: Cambridge University Press, Cambridge, U.K.: 37-46.

Rees, M.N., 1984. A fault-controlled trough through a carbonate platform, Middle Cambrian House Range embayment, Utah and Nevada, United States.

Rees, M.N., 1986. A fault-controlled trough through a carbonate platform; the Middle Cambrian House Range Embayment. Geological Society of America Bulletin, 97(9): 1054-1069.

Robison, R.A., 1982. Some Middle Cambrian agnostoid trilobites from western North America. Journal of Paleontology, 56(1, Part 1): 132-160.

Robison, R.A., 1999. Base of Ptychagnostus atavus Zone, candidate stratotype for base of unnamed international series. in Palmer, A.R., ed., Laurentia 99. V Field Conference of the Cambrian Stage Subdivision Working Group, International Subcommission on Cambrian Stratigraphy, Institute for Cambrian Studies, Boulder, Colorado: 15–17.

Rogers, J.C., 1984. Depositional environments and paleoecology of two quarry sites in the Middle Cambrian Marjum and Wheeler formations, House Range, Utah. Geology Studies, 31(1): 97-115.

Savrda, C.E., Bottjer, D.J., 1987. The exaerobic zone, a new oxygendeficient marine biofacies. Nature Geoscience, 327: 54-56.

Scotese, C.R., 2001. Atlas of Earth History, Volume 1, Paleogeography, PALEOMAP Project, Arlington, Texas, 52 pp.

Scotese, C.R., Barrett, S.F., 1990. Gondwana's movement over the South Pole during the Palaeozoic; evidence from lithological indicators of climate. Memoirs of the Geological Society of London, 12: 75-85.

Speed, R.C., 1982. Evolution of the sialic margin in the central Western United States. AAPG Memoir, 34: 457-468.

Swartzendruber, L.J., 1991. Properties, units and constants in magnetism. Journal of Magnetism and Magnetic Materials, 100: 573-575.

Tarling, D.H., Hrouda, F., 1993. The magnetic anisotropy of rocks. London ; New York : Chapman & Hall, 1993. 1st ed.

CHAPTER II: TRACING THE BASE OF THE DRUMIAN STAGE: TESTING THE SYNCHRONICITY OF THE FAD/LOOP OF *PTYCHAGNOSTUS ATAVUS* WITHIN THE HOUSE RANGE EMBAYMENT, WESTERN LAURENTIA

The base of the Drumian Stage at the Global boundary Stratotype Section and Point (GSSP) locality in the Drum Mountains, Utah, was defined by the First Appearance Datum (FAD) of the Agnostoid trilobite *Ptychagnostus atavus* (Babcock et al., 2007). The Lowest Occurrence Observed Point (LOOP) of the same fossil was reported at 27 m above the base of the Wheeler Formation in the House Range, western Utah, and at 30 m above the Lincoln Peak/Pole Canyon formations boundary in the southern Snake Range, eastern Nevada (Robison, 1982). Speculation arises concerning the validity of the FAD/LOOP of *P. atavus* as biostratigraphic marker used to constrain the base of the Drumian Stage in these locations when high resolution correlation is conducted. Is it synchronous across the House Range Embayment (HRE)? If not, where is the base of Drumian Stage in the Marjum Pass locality, House Range and the southern Snake Range? Is *P. atavus* a useful index in defining the base of the Drumian Stage?

The answer to these questions becomes more difficult in the absence of common lithostratigraphic and other biostratigraphic markers across the HRE. This makes geochemical and geophysical data sets a more effective and reliable way to correlate among localities in western Laurentia. This study focuses on regional high-resolution correlation among three Middle Cambrian marine sedimentary successions that contain the base of the Drumian Stage. Closely-spaced samples have been collected from, (1) the Drumian GSSP in the Drum Mountains, western Utah, (2) the Marjum Pass section in the House Range, further west in Utah, and (3) the Packrat section in the Snake Range, Great Basin National Park, eastern Nevada.

The base of the Drumian Stage is traced from the GSSP to the other two successions and lies at the base of the first of three storm layers identified in all three studied successions. This layer represents a lithostratigraphic marker unit that helps to constrain not only the basal boundary of the Drumian Stage, but also the LOOP of *P. atavus* within the HRE slope and basinal sections studied. The FAD/LOOP of *P. atavus* is diachronous within the three studied sections and is recorded within carbonate-dominated storm deposits. However, its acme is synchronous and is observed at the base of the carbonate-dominated layer, CP8, which was deposited during normal sedimentation processes. Unfortunately, the GSSP was defined based on reworked *P. atavus* specimens at the base of the first storm layer that has an erosional base and is composed of reworked sediments. Consequently, the Drumian stage GSSP should be redefined. The Packrat section in Great Basin National Park is a good candidate for redefinition because it is the least affected by storm deposits above the Pole Canyon/Lincoln Peak formations boundary, has high sediment accumulation rates (SAR), and records sea level fluctuation effectively. The LOOP of *P. atavus* is likely to occur globally within carbonate-dominated facies. Facies are well correlated among slope-and-basinal successions of western Laurentia and southern China at the LOOP of *P. atavus*.

2.1. Introduction

The International Union of Geological Sciences (IUGS) and the International Commission on Stratigraphy (ICS) are working hard to locate stratigraphic sections that have continuous sedimentation with decent sediment accumulation rates (SAR) that assure events separation. Such successions represent formally defined standards for the Phanerozoic, and once all are defined, will serve as the Global boundary Stratotype Section and Point (GSSP) for the base of any given geologic

stage (Cowie, 1986; Cowie et al., 1986; Remane et al., 1996). The rules for defining GSSP sections indicate that a GSSP should not be defined based on a reworked species, not have any major erosional surfaces, not have missing intervals or reworked sediments at the GSSP level, because it represents a reference section to which other equivalent sequences can be correlated (Cowie, 1986; Cowie et al., 1986; Remane et al., 1996).

This study focuses on the GSSP for the basal boundary of the Middle-Cambrian Drumian Stage, at ~505 Ma (Gradstein et al., 2012). It was ratified in 2006 by both the ICS and IUGS, and placed at the First Appearance Datum (FAD) of *P. atavus* on Stratotype Ridge, Drum Mountains, Utah, USA (Babcock et al., 2007). The Drumian GSSP section was selected within an open-shelf to basinal low-latitude locality because it contains unique faunal assemblages that can be correlated to low and high latitude sections of both open-shelf and slope-to-basin areas (Babcock et al., 2004; 2007). *P. atavus* was favored to define the base of this stage because it has worldwide recognition and its FAD was correlated to Lowest Occurrence Observed Point (LOOP) among multiple localities; Australia, Asia, Europe and North America (Robison, 1982; Rowell et al., 1982; 1994; Geyer and Shergold, 2000; Peng and Robison, 2000; Ergaliev and Ergaliev, 2001; Pham, 2001; Babcock et al., 2004; Peng et al., 2004; 2007). In the present study, two other equivalent sections were targeted, (1) the Marjum Pass section that was collected in the House Range (39°14'30.13" N - 113°22'30.61" W) , western Utah, and (2) the Packrat section that was collected along the North Fork of the Big Wash (38°54’00.63926” N - 114°13’25.05219” W), Great Basin National Park, southern Snake Range, White Pine County, eastern Nevada (Fig. 2.1).

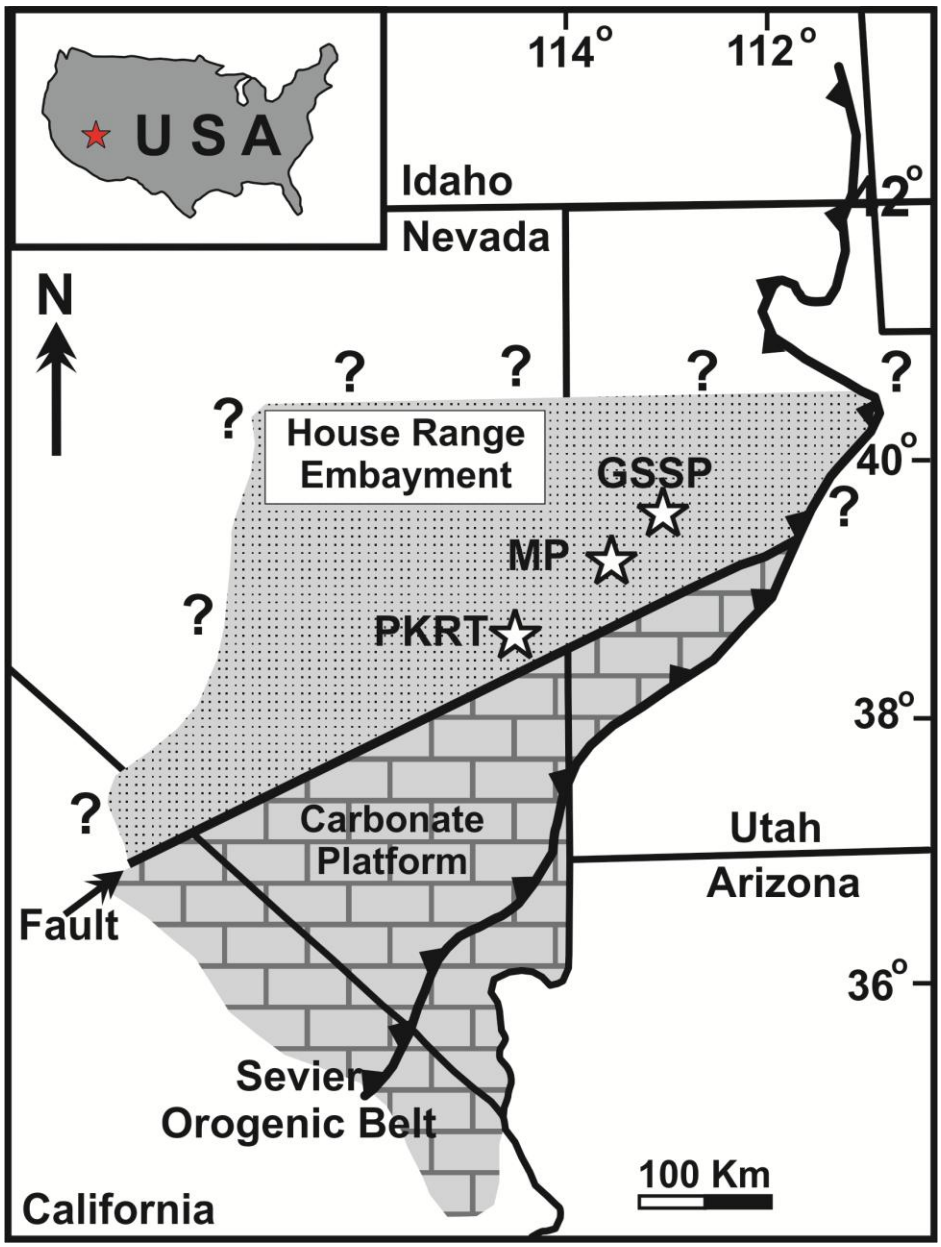

Figure 2.1. Non-palinspastic reconstruction map showing the location of the studied GSSP, Marjum Pass and Packrat sections (modified from Palmer, 1971; Elrick and Snider, 2002; Howley et al., 2006). The NE–SW normal fault separates the Laurentian carbonate shelf facies from the slope, mixed siliciclastic-carbonate facies.

The stratigraphic position of FAD of *P. atavus* in the HRE was defined at 71 m above the Wheeler Formation in the Drum Mountains, and the LOOPs of *P. atavus* at 27 m above the base of the same formation in the House Range, and at ~30 m above the base of the Lincoln Peak Formation in the Snake Range (Robison, 1982; Rowell et al., 1982; 1999). At the GSSP section, a few individuals were recovered after intensive *P. atavus* search below its previous stratigraphic position.

Accordingly, the FAD of *P. atavus* was stratigraphically moved down to 62 m above the base of the Wheeler Formation, at the base of the first calcisiltite, the first storm, layer (Babcock et al., 2004; 2007). However, the previous FAD of *P. atavus* is considered to be its acme because a thin coquina limestone bed that is composed almost entirely of *P. atavus* allochems was observed at the GSSP section (Babcock et al., 2007).

Testing the synchronicity of the FAD/LOOP of *P. atavus* within the HRE was challenging and its correlation among the three locations was tentative. Multiple factors led to this uncertainty. First, the FAD/LOOP positions in the three sections are not tied to lithostratigraphic nor other reliable biostratigraphic markers that can be traced from one section into another. Second, the three sections are markedly different in lithology: the GSSP is carbonate-dominated, Marjum Pass is detrital-dominated and the Packrat locality has multiple mixed facies (Chapter-I; Howley et al., 2006). Third, *P. atavus* has exhibits only rare occurrences and requires intensive search to be recovered. As a result, in the GSSP section, the FAD of *P. atavus* was redefined at 9 m below its previous position before it was finally ratified in 2006 (Robison, 1982; Babcock et al., 2004). Last, *P. atavus* is often confused with *Ptychagnostus gibbus* because these two Agnostoid trilobites have multiple common morphological characteristics (Robison, 1982; Rowell et al., 1982). The coarse correlation among HRE sections has contributed to the resolution problem discussed above. Although coarse correlation is useful in identifying long-term lithological variations that solve many other problems, still, it is limited in defining common chronostratigraphic surfaces to which these FAD/LOOP points can be adjusted.

The present study integrates the high-resolution correlation among the GSSP, Marjum Pass, and Packrat sections that has been established using Magnetic

susceptibility (χ) and calcium carbonate content ($CaCO_3$%), with the LOOP, FAD and acme of *P. atavus*. The search for *P. atavus* was also conducted at the Packrat and Marjum Pass sections. Our goals here were, 1) to identify lithostratigraphic marker (s) that might be used to trace the base of the Drumian Stage within the HRE, 2) to trace the FAD/LOOP of *P. atavus* from the GSSP through the Marjum Pass and into the Packrat section, 3) to test the synchronicity of *P. atavus* within the HRE, and 4) to investigate the reliability of *P. atavus* as biostratigraphic marker for high resolution studies.

2.2. Geological background

The House Range Embayment (HRE) was created by normal fault that cut through an extensive carbonate belt located along the western Laurentian continental margin and propagated eastward to ~400 km during the Middle Cambrian (Palmer, 1971; Brady and Koepnick, 1979; Rees, 1986; Hintze, 1988; Aitken, 1997) (Fig. 2.1). Therefore, the HRE represents a half-graben structure that is bounded by the normal fault to the south, and composed of a trough with northern, and southern ramps. The trough runs parallel with the fault propagation direction, and represents the deepest part of the embayment. The northern ramp is a drowning platform that was formed as a southward sloping ramp, and the southern ramp was a high-slope-angle ramp that has syndepositional structures such as syndepositional folding, sliding and density flows (Chapter-I; Dickinson, 1981; Robison, 1982; Speed, 1982; Rees, 1986). The HRE depth and width, as well as fault displacement, increase toward the HRE mouth, where the HRE meets the Panthalassic Ocean deep water along the western edge of the Laurentian passive margin (Rees, 1986). The Laurentian landmass was rotated 90° counterclockwise during the Phanerozoic, and the normal fault was turned from the NW-SE to the NE-SW direction (Rees, 1986). In

this paper, today's coordinates used unless otherwise stated. Therefore, the easterly paleo-trade winds are referred to here as northerly trade winds (Fig. 2.1).

Based on detailed facies examination, the precise depositional setting of each of the three studied sections within the HRE was reported (Chapter-I). The GSSP is a shallow trough section, the Marjum Pass is a lower-slope section of the northern HRE ramp, and the Packrat section is a lower-slope section of the southern HRE ramp. The water depth increased from the GSSP through the Marjum Pass to the Packrat sections, because the width and depth of the HRE increase in the southwesterly direction.

2.3. Methods

Unoriented samples were collected from the three sections at 5 to 10 cm intervals. During sampling, all covered intervals were cleaned and brushed to the freshest surface possible. 20-40 gm of each sample were placed in small (~76.2 x 76.2 mm) pre-labeled zip-lock plastic bags and returned to the Rock Magnetism Laboratory at LSU for final preparation and measurement. All samples were run for χ and $CaCO_3$% to account for detrital and carbonate contents respectively. χ measurements were conducted using the Williams high-sensitivity χ Bridge in the rock magnetism laboratory at LSU; an extremely low, alternating field χ bridge that is calibrated relative to mass using standard salts (Swartzendruber, 1991). Carbonate digestion has been performed using the method of Jones and Kaiteris (1983). Refer to chapter I for more details about mass-specific χ and $CaCO_3$% measurements. Each measurement is assumed to represent relatively short period of time. The outcrop search for *P. atavus* was conducted for the Packrat and Marjum Pass sections, and this included additional microscopic examination of 194 Packrat samples in the laboratory following sampling.

2.4. Results and Interpretations

$CaCO_3$% and χ data are presented versus the height of each section in figures 2.2 and 2.3. These curves cover an interval that includes the Middle-Cambrian uppermost part of unnamed Stage Five and the lowermost part of the Drumian Stage. The nine correlation star points (CPs: CP1-CP9), the red arrows, and the five intervals (A to E) are placed on the two figures for correlation purposes. They highlight the peaks and troughs, direction of change, and different sealevel stages represented by χ and $CaCO_3$ curves. Each of these features were traced from the GSSP through the Marjum Pass and into the Packrat section and reported to be synchronous across the NE-SE HRE transect (Chapter I). Similarly, the three storm layers (I, II, and III; Figs. 2.2 and 2.3) which are deposited during three separate storm events, are synchronous and traced among the three sections (Chapter I).

Because the base of the Drumian Stage was defined by the FAD of *P. atavus* (Babcock et al., 2007), the *P. atavus* search was conducted in the field and laboratory for both the Marjum pass and the Packrat sections. At the Packrat section, careful examination of the outcrop and the nearby scree using field lens, and laboratory microscopic examination of 194 samples, yielded no *P. atavus* specimens. In addition, multiple specimens have been recovered from the Marjum Pass section at ~30 m above the base of the Wheeler formation. This level lies within at the base of the carbonate dominated layer, CP8 (Figs. 2.2 and 2.3). The stratigraphic position of the acme, FAD/LOOP of *P. atavus* is presented as thick color-coded lines (red and green) in figures 2.2 and 2.3. This position is based of the work of Robison (1982), Rowell (1982), Babcock and others (2007), and the *P. atavus* search conducted here.

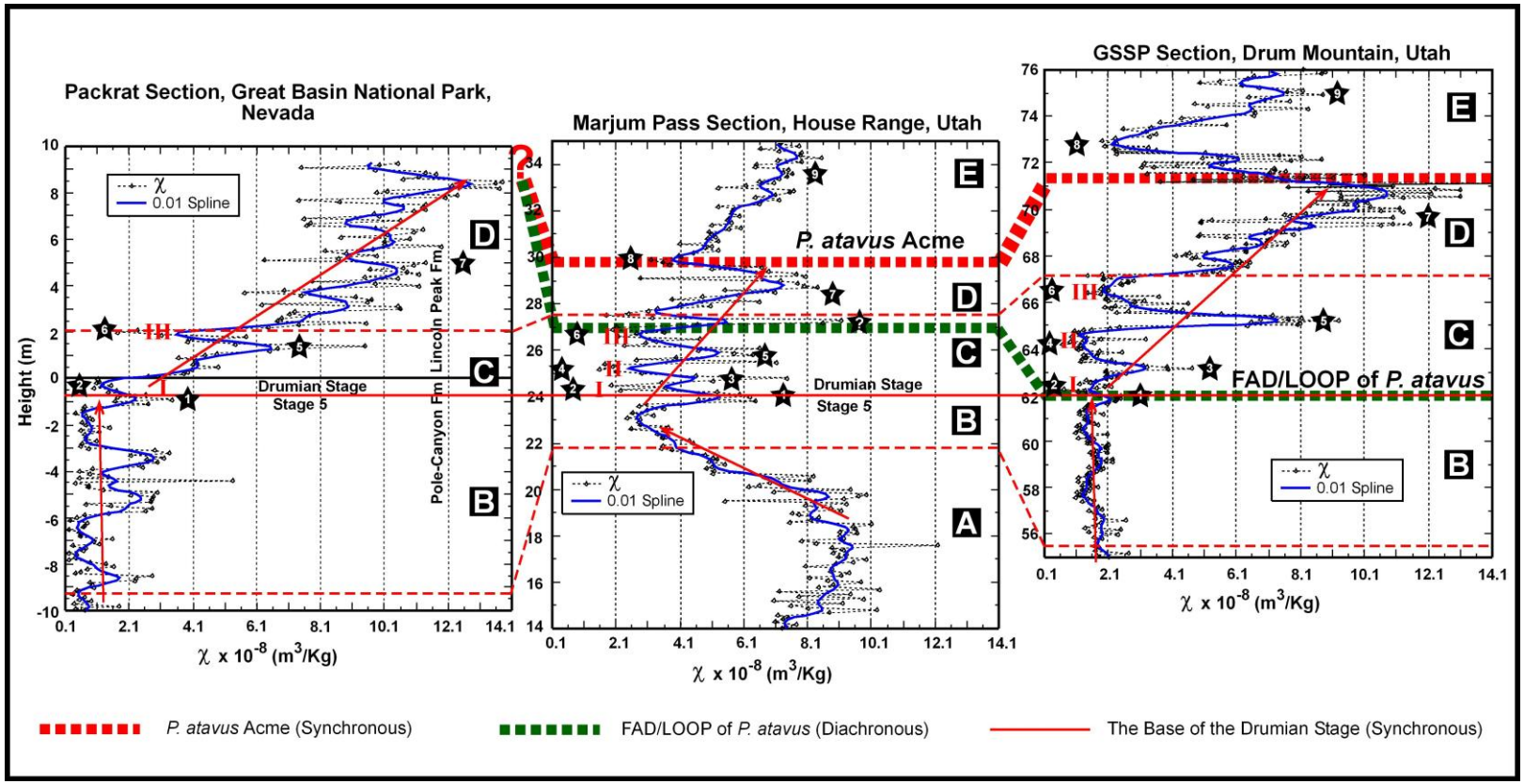

Figure 2.2. Three χ curves showing high-resolution correlation among the three studied sections(Modified from Chapter I). The height of these curves starts at the closest formation boundary; the base of the Wheeler Formation in the GSSP and Marjum Pass sections, and the base of the Lincoln Peak Formation in the Packrat section. The numbered stars represent correlation points (CPs) where the χ signal has high correlation potential among the three sections. Each CP represents either a peak or a trough on the χ curve. The base of the Drumian Stage was traced from the GSSP (Babcock et al., 2007) to the Packrat through the Marjum pass at the base of the first storm layer (CP2). The red dashed lines above and below the basal boundary of the Drumian Stage break the observed χ cycles into six intervals, A to E. The red arrows represent the direction of change of the χ curve. The stratigraphic position of the acme and the FAD/LOOP of *P. atavus* are presented as thick red and green dashed lines respectively**.**

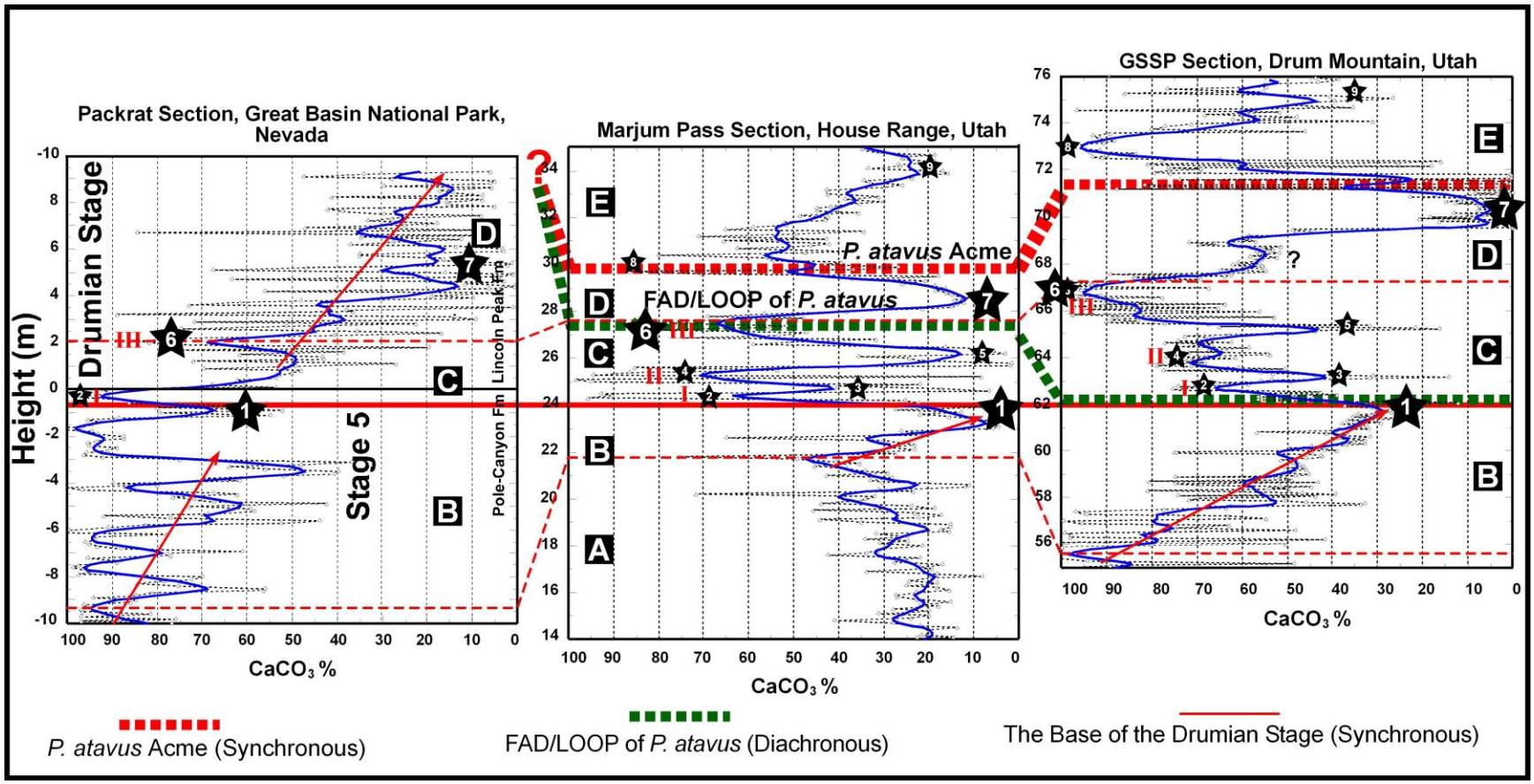

Figure 2.3 Three $CaCO_3$% curves showing high-resolution correlation among the three studied sections (modified from Chapter I). Similar to figure 2.2, the nine correlation star points (CPs: CP1-CP9), the red arrows, and the five intervals (A to E) are placed on the $CaCO_3$ curves for correlation purposes. The base of the Drumian Stage was traced from the GSSP (Babcock et al., 2007) to the Packrat through the Marjum pass at the base of the first storm layer (CP2). The stratigraphic position of the acme and the FAD/LOOP of *P. atavus* are presented as thick red and green dashed lines respectively**.**

2.5. Discussion

2.5.1 The base of the Drumian Stage

The three storm layers (I, II, and III; Figs. 2.2 and 2.6) represent lithostratigraphic markers that facilitate the correlation among the three studied sections and help in tracing the base of the Drumian Stage from the GSSP to the other two sections. The first layer (Figs. 2.6, 2.5, and 2.4) is favored over the other two succeeding storm layers because it has unmistakable χ and $CaCO_3$% signals and can be traced among the HRE sections. It is observed in the HRE trough, northern ramp, and southern ramp sections (Figs. 2.2 to 2.5). However, the second (II) and third (III) storm layers have either vanished or are decreased dramatically in thickness at the southern ramp Packrat section (Figs. 2.2 and 2.3).

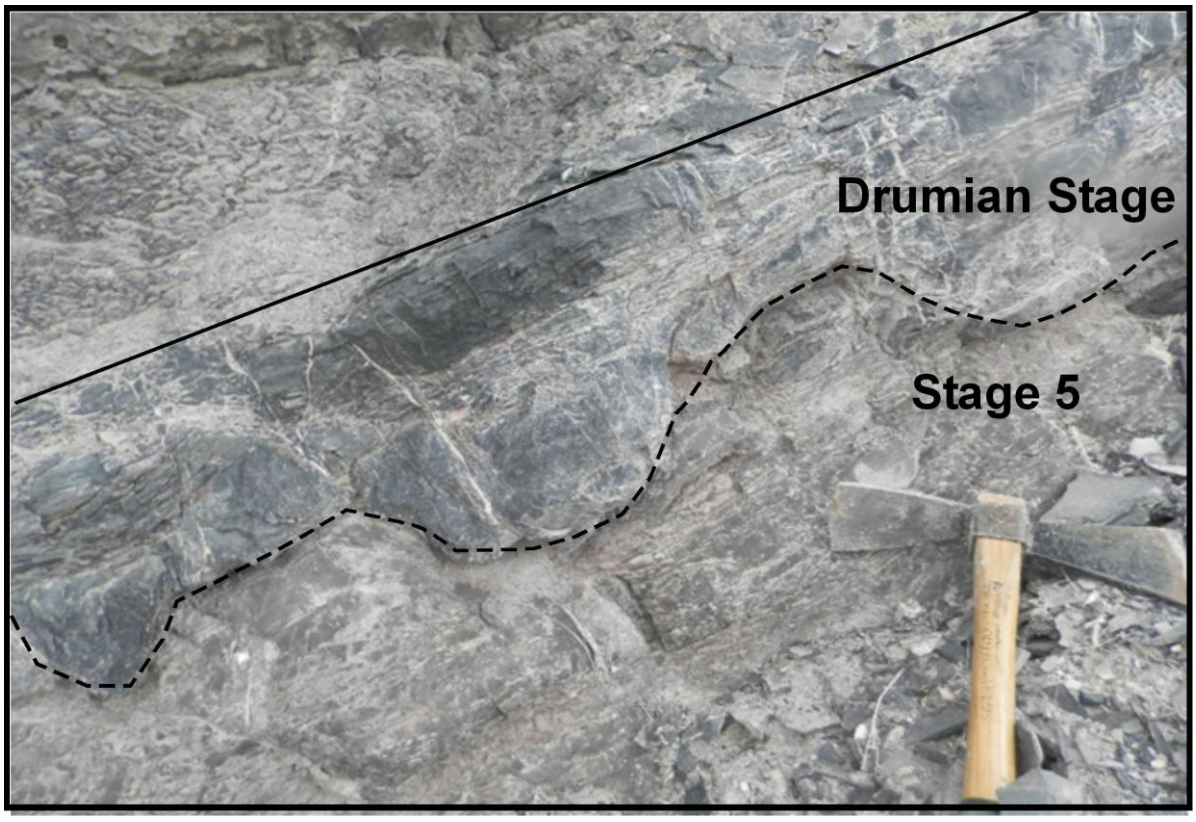

Figure 2.6. Photographs showing the basal boundary of the Drumian Stage at the GSSP section at 62 m above the base of the Wheeler Formation. Ripple marks predominate this erosional surface as it represents the base of the first storm layer, CP2 in figures 2.2 and 2.3. The black dashed line mark this erosional surface.

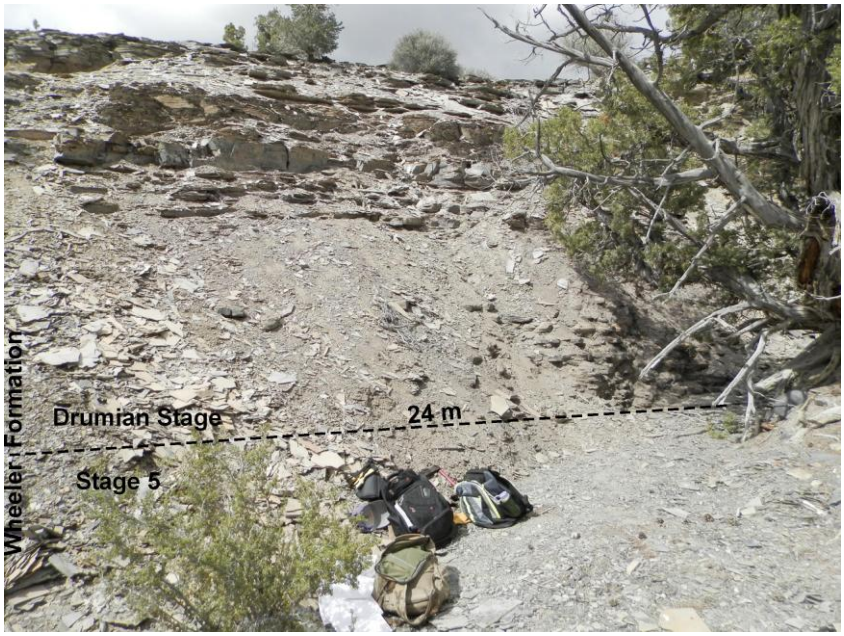

Figure 2.7. Photographs showing the basal boundary of the Drumian Stage at the Marjum Pass section as a black dashed line at 24 m above the base of the Wheeler Formation. The section represent the northern wall of east-west drainage. The back bags are on the drainage bed and the upstream is to the right, east.

Figure 2.8. Photographs showing the basal boundary of the Drumian Stage at the Packrat section as a black dashed line at 0.8 m below the base of the Lincoln Peak Formation. The dark grey layer above the dashed line represents the base of the Drumian stage first storm event (I), at CP2 in figures 2.9 and 2.3 that has high correlation potential among the three sections.

At the GSSP section, the basal boundary of the Drumian Stage was defined at 62 m above the base of Wheeler Formation, at base the first calcisiltite, storm,

layer (Fig. 2.6) (Chapter-I; Babcock et al., 2007; Brett et al., 2009). Consequently, it is traced to 24 m above the base of Wheeler Formation in the Marjum Pass section and ~0.8 m below the Pole-Canyon/Lincoln Peak formations boundary in the Packrat section (Figs. 2.2 and 2.3). These three points mark the base of the first storm layer that is synchronous among the three sections because it is formed within a very short time span. In addition, the storm layer is left undisturbed because bioturbation was insignificant during the middle Cambrian (Gingras and Konhauser, 2015). The synchronicity of the base of the Drumian Stage is supported by high-resolution chemostratigraphic ($\delta^{13}C$ and $\delta^{18}O$) correlation among the studied sections (Chapter-III; Babcock et al., 2007; Howley and Jiang, 2010). The base of the Drumian Stage was reported at 10, 6, 9.5 m below the maximum negative $\delta^{13}C$ excursion at the GSSP, Marjum Pass and Packrat sections respectively where the intervening intervals vary according to SAR (Chapter-III; Babcock et al., 2007; Howley and Jiang, 2010). This negative $\delta^{13}C$ excursion is known as the DrumIan Carbon isotope Excursion or DICE.

2.5.2 The FAD/LOOP of *Ptychagnostus atavus*

The FAD/LOOP of *P. atavus* is diachronous because it is observed at different stratigraphic positions within the three studied sections. At the GSSP section, the stratigraphic position of the FAD of *P. atavus* defines the base of the Drumian Stage at 62 m above the base of the Wheeler Formation, at the base of Storm Layer I (Babcock et al., 2007). At the Marjum Pass section, Robison (1982) reported the LOOP of *P. atavus* at 27 m above the base of the Wheeler Formation. This level is 3 m above the base of the Drumian Stage and lies within Storm Layer III, the third carbonate-dominated storm layer (Figs. 2.2 and 2.3). At the Packrat section, intensive search yielded no *P. atavus* specimens. This makes the work done by

Robison (1982) very important in estimating the position of the LOOP of *P. atavus* in the Packrat section. He reported *P. atavus* at 30 m above the base of Lincoln-Peak Formation. This level is 30.8 m above the base of the Drumian Stage and lies far above the collected section. Consequently, the FAD/LOOP of *P. atavus* is diachronous and lies at 0 m, 3 m and 30.8 m above the base of the Drumian Stage at the GSSP, Marjum Pass, and the Packrats sections, respectively (thick green dashed line; Figs. 2.2 and 2.3). Although the intervening interval increases basinward, it is very thick at the Packrat section and would require an intensive *P. atavus* search below the current reported LOOP and above the collected section to identify a LOOP that is expected to be closer to the actual FAD of *P. atavus* defined at the GSSP.

However, the acme of *P. atavus* is observed to be synchronous between the GSSP and the Marjum Pass sections. This acme is not tested in the Packrat section because the stratigraphic position of *P. atavus* lies above the collected section here. In this study, the search for *P. atavus* was conducted at the Marjum Pass section. Multiple specimens have been recovered from the base of the carbonate-dominated layer, CP8, at ~30 m above the base of the Wheeler Formation (Figs. 2.2 and 2.3). This layer was deposited during a time when sea level was falling and the carbonate factory was prograding, and is located 6 m above the base of the Drumian Stage FAD. It also overlies a detrital-dominated layer, CP7, which was deposited during a maximum sea level rise (Figs. 2.2 and 2.3). Noteworthy is the fact that the multiple recovered specimens from CP8, and CP7 have high correlation potential with the GSSP section (Figs. 2.2 and 2.3). At the GSSP section, a thin limestone coquina with *P. atavus* allochems was recorded at 71 m above the base of the Wheeler Formation (Robison, 1982; Babcock et al., 2007). This level represents the *P. atavus*

acme (Babcock et al., 2007) and lies at the base of carbonate-dominated layer, CP8, which overlies the detrital-dominated layer, CP7 (Figs. 2.2 and 2.3). By extending these markers into the Packrat section, *P. atavus* specimens are expected to be recovered from a carbonate-dominated layer located not too far from the top of the collected section. If proven, the Packrat section would be a good candidate for selection as an alternative Drumian GSSP.

In the GSSP and the Marjum Pass sections, the acme of *P. atavus* is synchronous, and is observed to lie at the base of CP8. This layer, along with underlying layer CP7, was deposited during normal sedimentation, as opposed to storm processes. However the FAD/LOOP of *P. atavus* is diachronous and recorded within carbonate-dominated layers that were deposited during storm events. Even though each storm layer is considered as a chronostratigraphic marker that is synchronous among the HRE sections, it represents reworked sediments and includes reworked *P. atavus* specimens. It is likely that *P. atavus* was living close to the shelf edge of the western Laurentian passive margin. Because the HRE edge, slope, and basinal areas represent an inward extension of their counterparts into the western Laurentian passive margin (Rees, 1986), they are influenced by the same physical processes working on the extensive carbonate platform. During storm events, *P. atavus* was washed off the shelf edge and deposited in slope and basinal areas within reworked sediments. This accounts for the existence of *P. atavus* within the first and third storm event in the GSSP and Marjum Pass sections, respectively. Because the storm sediments are sourced from the northern carbonate platform, the LOOP of *P. atavus* is not observed within the first storm layer in the Packrat section where its carbonates are sourced from the southern carbonate platform.

The HRE paleogeographic setting, ocean circulation pattern, the location of each section, the intensity of the turbidity current, and the slope angle of the seafloor dictate the downslope reach of the carbonate sediments and the stratigraphic position of the FAD/LOOP of *P. atavus* in each section. The paleogeographic setting of the HRE expedites the delivery of *P. atavus* into the HRE during these storm events because it extends more than 400 km into the western Laurentian carbonate platform perpendicular to the trade wind direction (Rees, 1986; Elrick and Snider, 2002). The paleo trade winds likely control the wind pattern, and hence, the shelf currents in the study area (Elrick and Snider, 2002). Rees (1986) mentioned that the existence of pelagic Agnostoid trilobites within anoxic deep-water environments indicates that the HRE water was open to marine currents. Therefore, *P. atavus* is carried by shelf currents or turbidity currents along with carbonate sediments into the HRE. During the storm events, the intensity of the accompanied turbidity currents dictates the downslope grain-size distribution and hence the down reach of *P. atavus*. Proximal sections that are close to the northern HRE edge are expected to have their FAD/LOOP at lower stratigraphic position than distal sections.

2.5.3 A Drumian GSSP alternative

Unfortunately, the FAD at the GSSP was defined at the base of the first storm layer that is composed of reworked sediments and reworked *P. atavus* species (Fig. 2.6). In addition, the stratigraphic position (LOOP) of *P. atavus* is getting higher basinward as the depth and width increase toward the HRE mouth. In western Laurentia, the lowest stratigraphic occurrence of *P. atavus* is expected to be within unnamed Stage Five in the northern HRE edge sections; carbonate-dominated sections. The base of the Drumian Stage was constrained by χ, $CaCO_3$%, and the DICE within the HRE. (See chapter III for more details about DICE as a tool used to

constrain the base of the Drumian Stage). To this end, speculation arises about the validity of the FAD/LOOP of *P. atavus* as a biostratigraphic marker being used to constrain the base of the Drumian Stage when high-resolution correlation is required. Is *P. atavus* a reliable index in defining the Drumian GSSP? This speculation is extended to question the validity of Stratotype Ridge to host the Drumian GSSP section. Is it possible to define the GSSP for the base of the Drumian Stage based on a reworked species at the base of reworked sediments that has an erosional base? If not, do we need to redefine the Drumian GSSP? If yes, do we have an alternative that shows continuous sedimentation and has neither reworked sediments nor reworked *P. atavus* nor erosional base at its GSSP level?

It is the opinion of the authors of this paper that the Drumian GSSP should be redefined to a section that is not frequently interrupted by storm layers and has continuous sedimentation with a decent SAR that assures events separation. However, the new GSSP should be defined using the FAD of *P. atavus,* because it has a narrow stratigraphic range and worldwide geographic distribution (Robison, 1982; Rowell et al., 1982; Robison, 1994; Peng and Robison, 2000; Peng et al., 2004; Babcock et al., 2007). In addition to the FAD of *P. atavus,* other data sets should be developed for the GSSP, such as magnetic polarity, χ, carbonate content, definition of the stable isotope DICE anomaly, other stable isotopic data, elemental geochemistry, and other data where appropriate.

If one were choosing such a succession from the sections studied here, the Packrat section is favored over the Marjum Pass section as a candidate for this GSSP, because, 1) it is least affected by storm events and storm deposits. Storm layers observed in other sections here, have either disappeared in the Packrat section or are reduced dramatically in thickness above the Pole-Canyon/Lincoln

Peak formation boundary. 2) The Packrat section exhibits higher SARs that insure expanded section and thus better event separation (e.g., intervals B and D, Figs. 2.2 and 2.3). Interval D exhibits well-defined short-term cycles during sealevel rise (Fig. 2.3), while these cycles merge in the Marjum Pass section. 3) The Packrat section records sea level fluctuations more effectively than does the Marjum Pass or current GSSP section. The steady χ increase above the base of the Drumian Stage reflects a steady sea level rise that reaches a maximum at the top of the interval D (Figs. 2.2 and 2.3). Even though the Packrat locality exhibits syndepositional folding and sliding surfaces, the intervals that were collected are not significantly affected by this deformation.

2.5.4 Global occurrence of *P. atavus*

The facies changes that coincide with the FAD/LOOP of *P. atavus* within HRE slope and basinal sections is supported globally by multiple studies (Peng and Robison, 2000; Peng et al., 2004; Zhu et al., 2004). Here, the FAD/LOOP of *P. atavus* is observed within carbonate-dominated sediment layers that either formed during storm events and intercalate with detrital-dominated layers, or formed during sea level falls and basinward progradation of shelf carbonate sediments over slope and basinal detrital-dominated intervals. Even though the location of each section studied here dictates the carbonate/detrital ratios within the carbonate- and/or the detrital-dominated intervals, χ and $CaCO_3$% analysis of high-resolution samples account for these lithological variations (Figs. 2.2 and 2.3). In south China, the facies change in the Wangcun section at the LOOP of *P. atavus,* from black shale with increasing amounts of dark gray, to thin-bedded limestone interbeds, to dark gray, thin-bedded limestone lacking black shale interbeds within the lower member of the overlying Huaqiao Formation (Peng and Robison, 2000; Peng et al., 2004; Zhu

et al., 2004) (Fig. 2.10). Consequently, factors that account for the LOOP of *P. atavus* in slope and basinal sections of western Laurentia, likely also hold true for the equivalent aged slope sections of the south China region. For global correlation to be successful, high-resolution studies between the slope and basinal sections of western Laurentia and southern China, using abiotic techniques such as χ, $CaCO_3$%, and stable isotopic analyses, are needed.

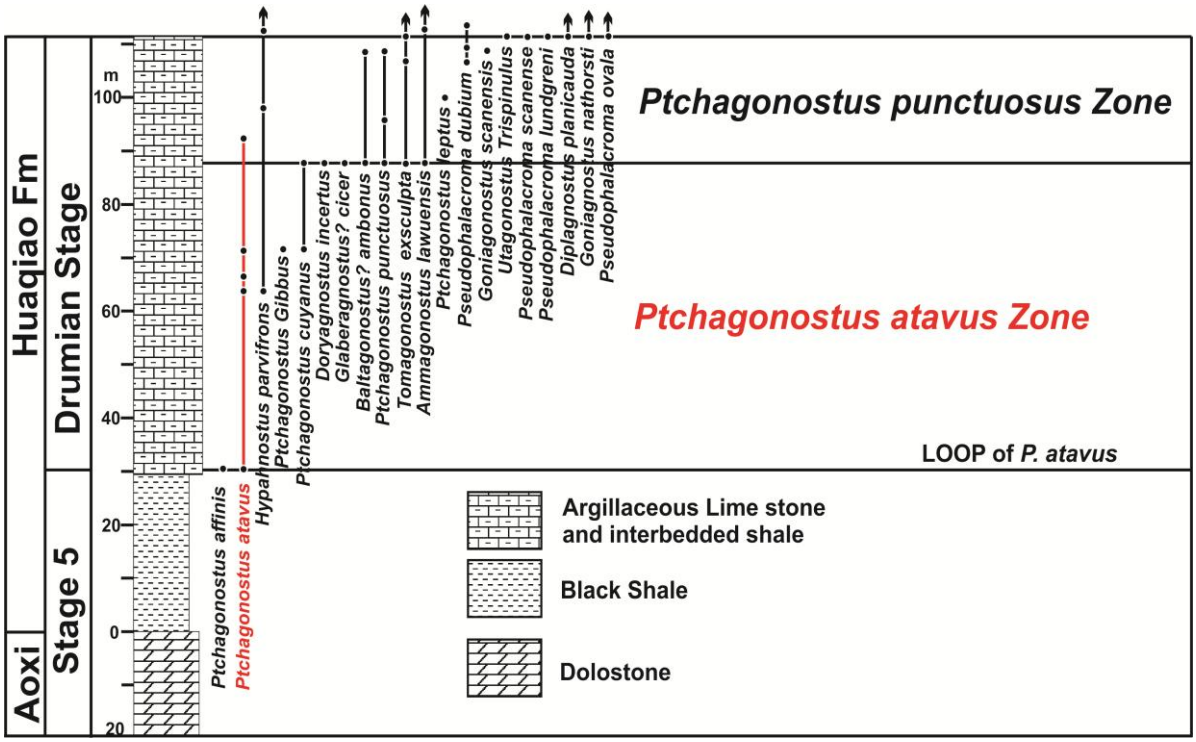

Figure 2.10. A biostratigraphic chart representing bizones and the associated facies at the base of the Middle-Cambrian Drumian Stage in the Wangcun section, western Hunan Province, China (modified from Peng and Robison, 2000; Peng et al., 2009). The LOOP of *P. atavus* resides at the base of the carbonate-rich interval that overlie a detrital-dominated layer close to the Aoxi/Huaqiao formation boundary. This signal is similar to its counterpart at the HRE sections.

2.6. Conclusions

Field observations along with closely-spaced sampling provide high resolution correlation among three Middle Cambrian succession deposited in the House Range Embayment (HRE), formed along the western margin of Laurentia during the Cambrian. These high-resolution data sets help unravel multiple key geological elements that would be difficult to explain with coarse correlation, widely-spaced

sampling techniques. The base of the Drumian Stage is traced from the Global boundary Stratotype Section and Point (GSSP) into two other HRE sections by using the base of the lowest storm-deposited turbidite layer as the 1st (I) event horizon. This layer is a lithostratigraphic marker unit that helps to constrain not only the basal boundary of the Drumian Stage, defined by the First Appearance Datum (FAD) of the Agnostoid trilobite, *P. atavus* at the GSSP, but also the Lowest Occurrence Observed Point (LOOP) of *P. atavus* and the DrumIan Carbon Isotope Excursion (DICE) within other HRE slope and basinal localities. The first storm layer (I) is found in the GSSP HRE shallow trough section, and can be traced into the Marjum Pass downslope section on the HRE northern ramp, and into the downslope Packrat section on the HRE southern ramp. The thickness of this layer is expected to be minimal far from the GSSP, or even to vanish in the downslope sections of the northern ramp close to the HRE mouth, where the HRE has its greatest depth and width. However, this using magnetic susceptibility (χ), CaCO3%, and $\delta^{13}C$ and $\delta^{18}O$ stable isotope data, Layer I was unambiguously identified in the Marjum Pass and Packrat successions.

In the GSSP and the Marjum Pass sections, the acme of *P. atavus* is synchronous and observed at the base of a carbonate-dominated layer, CP8. This layer, along with the underlying CP7 layer, were deposited during normal sedimentation process. However, the FAD/LOOP of *P. atavus* is found to be diachronous in the HRE and recorded within carbonate-dominated storm layers. Unfortunately, the GSSP was defined at the base of the first storm layer that has an erosional base and is composed of reworked sediments and reworked *P. atavus* specimens. Consequently, it is argued here that the base of the Drumian Stage should be redefined. The Packrat section in the Snake Range within Great Basin

National Park, eastern-most Nevada, USA, represents a good candidate for a new GSSP location, because it is least affected by the storm deposits in the HRE, has high sediment accumulation rates that assure better event separation, and therefore records sea level fluctuations more effectively.

Globally, the Lowest Occurrence Observed Point (LOOP) of *P. atavus* occurs within carbonate-dominated facies in the slope and basinal sections of western Laurentia and southern China. These facies were formed either during storm events and intercalate with detrital-dominated layers, or during sea level falls and basinward progradation of shelf carbonate-dominated sediments over slope and basinal detrital-dominated intervals.

2.7. References

Aitken, J.D., 1997. Stratigraphy of the Middle Cambrian plat-formal succession, southern Rocky Mountains. Geol. Surv. Can. , 398: 322

Babcock, L.E., Rees, M.N., Robison, R.A., Langenburg, E.S., Peng, S., 2004. Potential Global Standard Stratotype-section and Point (GSSP) for a Cambrian stage boundary defined by the first appearance of the trilobite Ptychagnostus atavus, Drum Mountains, Utah, USA. Geobios, 37(2): 149-158.

Babcock, L.E., Robison, R.A., Rees, M.N., Peng, S., Saltzman, M.R., 2007. The global boundary stratotype section and point (GSSP) of the Drumian Stage (Cambrian) in the Drum Mountains, Utah, USA. Episodes, 30(2): 85-95.

Brady, M.J., Koepnick, R.B., 1979. A Middle Cambrian platform-to-basin transition, House Range, West central Utah. Geology Studies, 26, Part 1: 1-7.

Brett, C.E., Allison, P.A., DeSantis, M.K., Liddell, W.D., Kramer, A., 2009. Sequence stratigraphy, cyclic facies, and lagerstätten in the Middle Cambrian Wheeler and Marjum Formations, Great Basin, Utah. Palaeogeography, Palaeoclimatology, Palaeoecology, 277(1-2): 9-33.

Cowie, J.W., 1986. Guidelines for boundary stratotypes. Episodes, 9(2): 78-82.

Cowie, J.W., Ziegler, W., Boucot, A.J., Bassett, M.G., Remane, J., 1986. Guidelines and statutes of the International Commission on Stratigraphy (ICS), 83. Courrier Forschungsinst. Senckenberg, 1-14 pp.

Dickinson, W.R., 1981. Plate tectonics and the continental margin of California. in Ernst, W.G., ed., The Geotectonic Development of California, Prentice-Hall, Upper Saddle River, New Jersey: 1–28.

Elrick, M., Snider, A.C., 2002. Deep-water stratigraphic cyclicity and carbonate mud mound development in the Middle Cambrian Marjum Formation, House Range, Utah, USA. Sedimentology, 49(5): 1021-1047.

Ergaliev, G.K., Ergaliev, F.G., 2001. Middle Cambrian trilobites and stages of the Malyi Karatau Ridge (southern Kazakhstan). in Peng, S.C., Babcock, L.E., and Zhu, M.Y., eds., Cambrian System of South China, University of Science and Technology of China Press, Hefei: 256.

Geyer, G., Shergold, J., 2000. The quest for internationally recognized divisions of Cambrian time. Episodes, 23(3): 188-195.

Gingras, M., Konhauser, K., 2015. The Cambrian evolution of burrowing species is thought to have facilitated sediment mixing. However, sediment fabrics suggest that bioturbation remained insignificant until the appearance of more efficient sediment mixer in Silurian Nature Geoscience, 8: 825-826.

Gradstein, F.M., Ogg, J.G., Schmitz, M.D., Ogg, G.M., 2012. The geologic time scale 2012. Elsevier : Oxford, United Kingdom, United Kingdom.

Hintze, L.F., 1988. Geologic history of Utah. Brigham Young University geology studies. Special publication: 7. Provo, Utah : Dept. of Geology, Brigham Young University, c1988.

Howley, R.A., Jiang, G., 2010. The Cambrian Drumian carbon isotope excursion (DICE) in the Great Basin, western United States. Palaeogeography, Palaeoclimatology, Palaeoecology, 296(1-2): 138-150.

Howley, R.A., Rees, M.N., Jiang, G., 2006. Research paper: Significance of Middle Cambrian mixed carbonate-siliciclastic units for global correlation: southern Nevada, USA. Palaeoworld, 15: 360-366.

Jones, G.A., Kaiteris, P., 1983. A vacuum-gasometric technique for rapid and precise analysis of calcium carbonate in sediments and soils. Journal of Sedimentary Petrology, 53(2): 655-660.

Palmer, A.R., 1971. The Cambrian of the Great Basin and adjacent areas, western United States. Wiley-Intersci., London-New York, International, pp. 1-78.

Peng, S. et al., 2009. The Global Boundary Stratotype Section and Point (GSSP) of the Guzhangian Stage (Cambrian) in the Wuling Mountains, northwestern Hunan, China. Episodes, 32(1): 41-55.

Peng, S., Robison, R.A., 2000. Agnostid biostratigraphy across the Middle-Upper Cambrian boundary in Hunan, China. Paleontological Society : Lawrence, KS, United States, United States.

Peng, S.C., Babcock, L.E., H.L., L., 2004. Polymerid Trilobites from the Cambrian of Northwestern Hunan, China. Volume 1: Corynexochida, Lichida, and Asaphida. Science Press, Beijing: 333.

Pham, K.N., 2001. On the Cambrian sediments in North Vietnam. in Peng, S.C., Babcock, L.E., and Zhu, M.Y., eds., Cambrian System of South China, University of Science and Technology of China Press, Hefei: 297.

Rees, M.N., 1986. A fault-controlled trough through a carbonate platform; the Middle Cambrian House Range Embayment. Geological Society of America Bulletin, 97(9): 1054-1069.

Remane, J. et al., 1996. Revised guidelines for the establishment of global chronostratigraphic standards by the International Commission on Stratigraphy (ICS). Episodes, 19(3): 77-81.

Robison, R.A., 1982. Some Middle Cambrian agnostoid trilobites from western North America. Journal of Paleontology, 56(1, Part 1): 132-160.

Robison, R.A., 1994. Agnostoid trilobites from the Henson Gletscher and Kap Stanton formations (Middle Cambrian), North Greenland. Grønlands Geologiske Undersøgelse Bulletin(169): 25–77.

Robison, R.A., 1999. Base of Ptychagnostus atavus Zone, candidate stratotype for base of unnamed international series. in Palmer, A.R., ed., Laurentia 99. V Field Conference of the Cambrian Stage Subdivision Working Group, International Subcommission on Cambrian Stratigraphy, Institute for Cambrian Studies, Boulder, Colorado: 15–17.

Rowell, A.J., Robison, R.A., Strickland, D.K., 1982. Aspects of Cambrian Agnostoid Phylogeny and Chronocorrelation. Society of Economic Paleontologists and Mineralogists and the Paleontological Society, pp. 161.

Speed, R.C., 1982. Evolution of the sialic margin in the central Western United States. AAPG Memoir, 34: 457-468.

Swartzendruber, L.J., 1991. Properties, units and constants in magnetism. Journal of Magnetism and Magnetic Materials, 100: 573-575.

Zhu, M.-Y., Zhang, J.-M., Li, G.-X., Yang, A.-H., 2004. Evolution of C isotopes in the Cambrian of China: implications for Cambrian subdivision and trilobite mass extinctions. Geobios, 37(2): 287-301.

CHAPTER III: HIGH-RESOLUTION STABLE ISOTOPE ($\delta^{13}C$ AND $\delta^{18}O$) CORRELATION AMONG THE HOUSE RANGE EMBAYMENT AND PLATFORM SECTIONS ACROSS THE BASE OF THE CAMBRIAN DRUMIAN STAGE, WESTERN LAURENTIA

Globally, the stratigraphic position of the Middle Cambrian DrumIan Carbon isotope Excursion (DICE) is observed to fall below, above, and to straddle the First Appearance Datum (FAD) of *Ptychagnostus atavus*, the Agnostoid trilobite that defines the base of the Drumian Stage (Babcock et al., 2004; Zhu et al., 2004; Zhu et al., 2006; Babcock et al., 2007; Howley and Jiang, 2010). In addition, the interval over which the DICE occurs is variable among marine slope and platform sections. Coarsely sampled data sets fail to provide an explanation for these inconsistencies. This study provides high-resolution correlation among three slope and basinal sections from the House Range Embayment (HRE) along the western Laurentian margin, where hundreds of samples have been analyzed to test the DICE synchronicity regionally within the HRE. Published chemostratigraphic data (Howley, 2010; Howley and Jiang, 2010) are used to extend this test into carbonate platform sections located to the south of the HRE.

It is concluded that the DICE is a chronostratigraphic marker that constrains the base of the Drumian Stage in the embayment and platform sections, except for where stable isotope values are suppressed by incoming heavy-isotopic platform carbonates. Here it is argued that the DICE maximum negative $\delta^{13}C$ excursion is locally synchronous and should be used for correlation among multiple coeval western Laurentia successions, because the DICE event marks the maximum sea level rise that follows the defined base of the Drumian Stage. However, the onset and the end of the DICE event are diachronous among the studied sections, and should not be used as stratigraphic datum when high-resolution correlation is desired.

The DICE event is interpreted to result from respiration and remineralization of organic matter that is included in the Middle Cambrian Oxygen Minimum Zone (OMZ). It is inferred that the OMZ was well-developed either, 1) only across the base of the Drumian Stage and imprinted the HRE and southern platform sections during this particular sea level rise rather than earlier or later sea level rises, or 2) during the entire Middle-Cambrian and sea level rose to an unprecedented level across the base of the Drumian Stage, elevating the OMZ to high levels, and allowing organic matter respiration through mixing with oxygen-rich surface water. The DICE event is observed on the southern HRE platform because HRE poorly-oxygenated, organic-rich, deep water was brought to the carbonate platform by trade wind driven surface currents.

The base of the Drumian Stage is argued to lie below the DICE on the southern platform at one of the erosional surfaces that have been observed by Howley and Jiang (2010), close to the maximum $\delta^{13}C$ excursion. High-resolution χ, Total Organic Carbon (TOC), and carbonate percent analysis are needed for the platform sections to examine which of these surfaces represent the Drumian Stage basal boundary.

3.1. Introduction

The DICE and the First Appearance Datum (FAD) of *P. atavus*, that have been observed in the Global boundary Stratotype Section and Point (GSSP) of the Cambrian Drumian Stage in the Drum Mountain of western Utah, are considered to be a worldwide chemostratigraphic and biostratigraphic markers that helps to constrain the base of the Drumian Stage (Peng and Robison, 2000; Babcock et al., 2004; Peng et al., 2004; 2007; Howley and Jiang, 2010). However, the precise stratigraphic position for LOOPs of *P. atavus* and DICE are tentative and uncertain.

The LOOP of *P. atavus* is reported to be diachronous and is recorded within carbonate-dominated storm deposits regionally within the HRE (Chapter II). Globally, the DICE is actually either below, above, or it straddles the LOOP of *P. atavus,* even in sections that exhibit similar depositional environments. For example, in south China a negative carbon isotopic excursion is observed below the LOOP of *P. atavus* in the Huaqiao Formation within a section at Wangcun (Zhu et al., 2004). In the USA, the DICE is located 72 m above the base of the Wheeler Formation within the GSSP section, which is 10 m above the FAD of *P. atavus* (Babcock et al., 2005; Babcock et al., 2007). In addition, Zhu et al. (2006) reported that the LOOP of *P. atavus* is associated with the end of the DICE, where the DICE event is shown to straddle the base of the Drumian Stage in the Cambrian $\delta^{13}C$ composite curve. In Southern Sweden, the DICE is maximum in a thin limestone bed above the base of *P. atavus;* this based on organic $\delta^{13}C$ values (Ahlberg et al., 2009).

Both the GSSP and Wangcun sections have similar depositional environments because they are slope sections of the western Laurentian carbonate platform (Rees, 1986) and the Yangtze carbonate platform in China (Zhang et al., 2001) respectively. In addition, carbonates shed off the two platforms, and terrigenous materials are fed by ocean currents to both localities (Chapter-I; Zhang et al., 2001). Still, the stratigraphic positions of the negative $\delta^{13}C$ excursions and *P. atavus* are reversed. Without providing a reasonable explanation for the stratigraphic uncertainty of these two worldwide important markers within slope and basinal sections, their correlation and extrapolation into shallow shelf areas will be difficult.

In western Laurentian slope and basinal sections, the DICE chemostratigraphic interpretations are improving as high-resolution data sets are obtained. In 2003, the DICE was missed during sequence stratigraphic and

geochemical studies on the Wheeler Formation at the GSSP and at Marjum Pass (Langenburg). In Babcock and others (2004; 2007), the DICE was poorly-represented by only one data point in the GSSP section. Howley and Jiang (2010) reported the DICE onset at 7 m above the FAD of *P. atavus* at the GSSP and 3 m above the LOOP of *P. atavus* at the Marjum Pass section, based on 2 and 4 data points, respectively. However, inconsistency still exists among these studies due to inadequate chemostratigraphic resolution.

The present study provides high-resolution correlation among three HRE slope and basinal sections where hundreds of samples have been analyzed to test DICE synchronicity regionally within the HRE across the base of the Drumian Stage. These studied sections are, 1) the GSSP section, Drum Mountain, Utah, 2) the Marjum Pass section, House range, Utah, and 3) the Packrat section, Great Basin National Park, Snake Range, Nevada. In addition, this work is extended to three southern carbonate platform sections, Wah Wah, Panaca Hills and Desert Range, using the chemostratigraphic work of Howley and Jiang (2010) and Howley (2010).

3.2. Geological background

Laurentia is the name for the North American continent that formed during the late Neoproterozoic by the breakup of the Rodina Supercontinent (Rees, 1986). An extensive carbonate belt covered the passive margin of western Laurentia during the Middle-Cambrian. This carbonate belt is known as the Great American Carbonate Bank (GACB), and was built up mainly from algal and/or microbial carbonate-rich sediment (Palmer, 1971; Brady and Koepnick, 1979; Aitken, 1997). The GACB was bounded by Panthalassic deep-water sediments to the west and by shoreline sediments to the east (Rees, 1986). A normal fault cut through this extensive carbonate belt and propagated eastward for ~400 km, creating the HRE (Rees,

1986; Hintze, 1988) (Fig. 3.1). The HRE represents a half-graben structure that is bounded by the normal fault to the south, and composed of trough, northern and southern ramps. The trough is the deepest part of the embayment that is parallel to the fault propagation direction; the northern ramp is a drowning platform that formed as a southward sloping ramp; and the southern ramp is a high-slope-angle ramp that has syndepositional structures, including syndepositional folding, sliding and density flow (Chapter-I; Rees, 1986). The HRE depth and width, as well as fault displacement, increase westward and reach to their maximum at the HRE mouth, where the HRE meets Panthalassic Ocean deep-water at the western edge of the Laurentian passive margin (Rees, 1986).

The Middle-Cambrian Wheeler Formation is known to have multiple intervals of high fossil preservation potential (Gaines and Droser, 2005; Gaines et al., 2005; Halgedahl et al., 2009). This exceptional preservation is the result of low bioturbated, clay-rich, and low permeability facies that were deposited under poorly oxygenated, organic-rich, bottom water conditions (Gaines et al., 2005). In the GSSP section, a detrital-rich and carbonate-poor interval has been observed in the lower Wheeler Formation, at ~71 m above its base (Chapter-II). A similar interval has been observed in the Drum Mountains in the upper Wheeler Formation, at ~230 m above its base (Halgedahl et al., 2009). This interval is called a “hot zone” and has similar magnetic susceptibility (χ) and $CaCO_3$% signals. It is likely that these two intervals were formed under similar depositional environments even though the exceptional soft-bodied preservations that have been documented in the upper Wheeler hot zone, is not observed in the lower Wheeler interval. Instead, a thin limestone coquina that is composed almost entirely of *P. atavus* allochems has been observed in the lower interval (Babcock et al., 2007). Although the Middle-Cambrian HRE sequence

was subjected to four compressional events during the Paleozoic and Mesozoic, and extensional periods during the Cenozoic that displaced and distorted its original configuration, the studied sections lie in areas that have little deformation (Dickinson, 1981; Robison, 1982; Speed, 1982; Rees, 1984; Rees, 1986).

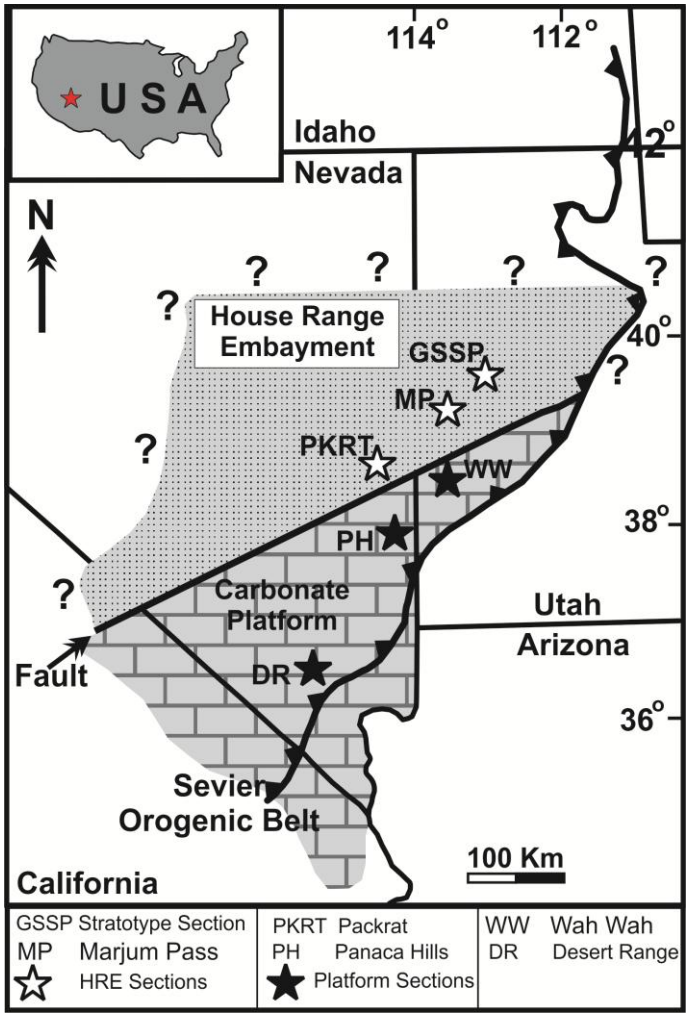

Figure 3.1. Non-palinspastic reconstruction map showing the location of the studied House Range Embayment (HRE) sections (GSSP, Marjum Pass and Packrat) as open stars and Platform sections (Wah Wah, Panaca Hills and Desert range) as black fill stars (modified from Palmer, 1971; Elrick and Snider, 2002; Howley et al., 2006). A NE–SW normal fault separates the Laurentian carbonate shelf facies of the southern platform from the slope, mixed siliciclastic-carbonate facies of the HRE.

3.3. Methods

In HRE slope and basinal sections, 372 samples were selected for isotopic analysis; this includes 103 samples from the GSSP, 97 samples from Marjum Pass, and 172 samples from the Packrat sections. The sampling interval ranges between

0.1 m and 0.5 m. Stable isotope analysis of carbonates ($\delta^{13}C$ and $\delta^{18}O$) were performed at Oxy-Anion Stable Isotope Consortium (OASIC) laboratory at LSU. Samples were calibrated using two working standards for every 10 samples. The $\delta^{13}C$ and $\delta^{18}O$ of the working standards are 2.57 ‰ and -4.31‰, respectively, to the Vienna Pee Dee Belemnite "VPDB" standard. 200±20 µg of each sample was placed into a vial and flushed with 99.999% pure Helium for 2 minutes at a flow rate of 80 ml per minute. The sample was allowed to react with high concentrated phosphoric acid for 3 hours. The resulting CO_2 output was processed and run through a Thermo Finnigan MAT 253 mass spectrometer for analysis. The reader is referred to Howley and Jiang (2010) for the materials and methods used for the isotopic analyses for the southern carbonate platform sections from western Laurentia.

3.4. DICE results and Interpretation for HRE sections

$\delta^{13}C$ and $\delta^{18}O$ data are presented versus the height in each section in figures 3.2 to 3.6. These curves cover the interval from the Middle-Cambrian uppermost part of unnamed Stage Five into the lowermost part of the Drumian Stage. In this study, the base of the Drumian Stage was traced from the GSSP section through the Marjum Pass and into the Packrat sections, using data from the base of the first storm layer (Layer I) identified by (Chapter-I and II). Regression analysis between $\delta^{13}C$ and $\delta^{18}O$ shows very low correlation at each of the three sections, indicating only minimal alteration effects in these sections (Figs. 3.2-c to 3.4-c). However, individual data points that do exhibit high correlation among these sections have been eliminated to avoid alteration effects biasing interpretation in the stable isotope data. The raw data are presented as black dashed lines with all data points included while the blue solid lines represent their splines (Figs. 3.2 to 3.6). The red arrows show trends of change in $\delta^{13}C$ and $\delta^{18}O$ curves.

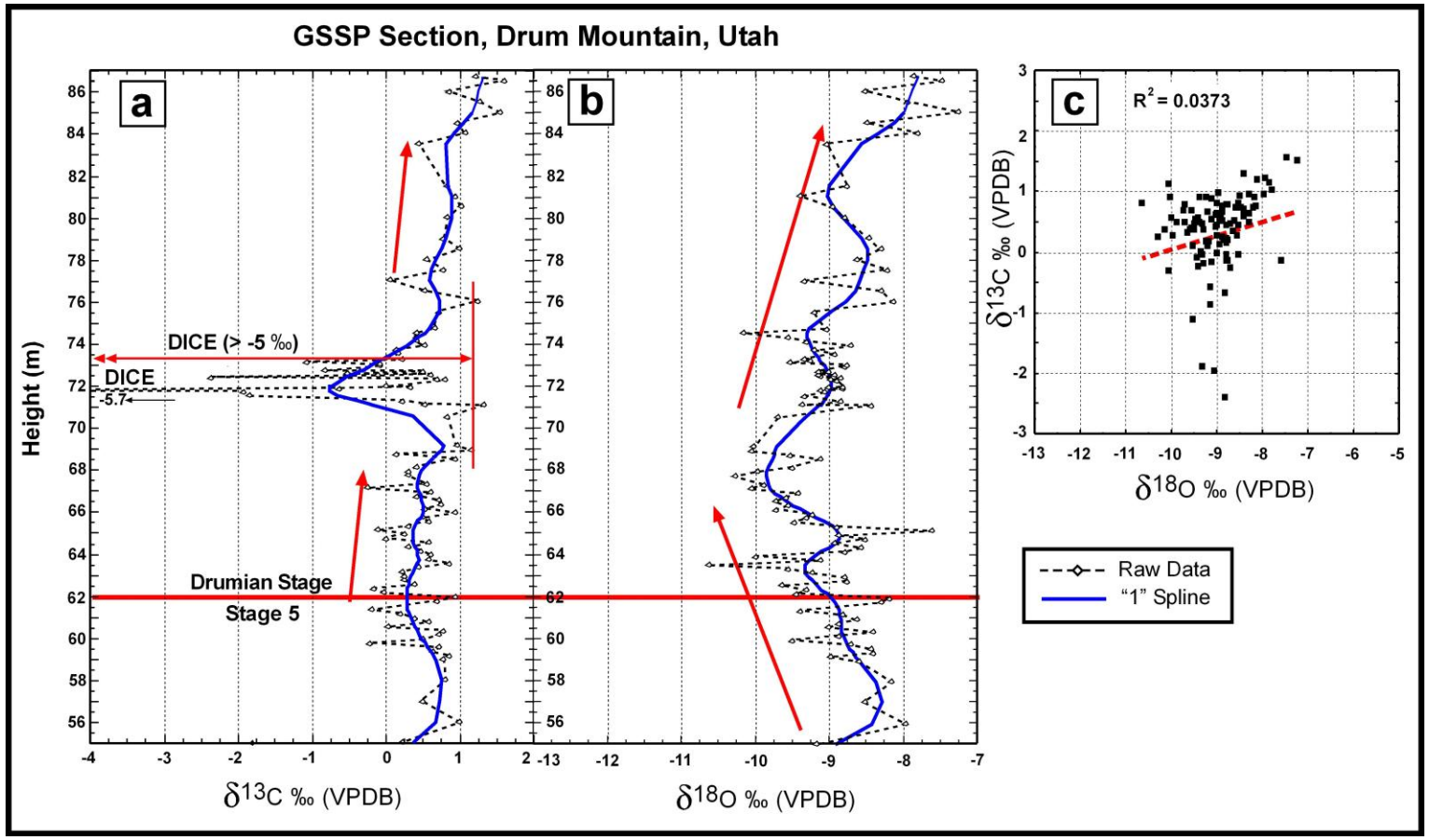

Figure 3.2. Three curves showing $\delta^{13}C$, $\delta^{18}O$ and their regression analysis obtained from the GSSP section showing the raw data as a black dashed line with data points included, and splined data as a solid blue line. (a) is the $\delta^{13}C$ curve. The maximum DICE excursion is shown by the double-headed arrow. (b) is the $\delta^{18}O$ curve. (c) represents the regression analysis between $\delta^{13}C$ and $\delta^{18}O$ with regression line and its coefficient (R^2) included. The base of the Drumian Stage is defined at 62 m in the section (Chapter-I; Babcock et al., 2007). The height of the GSSP is measured from the base of the Wheeler Formation.

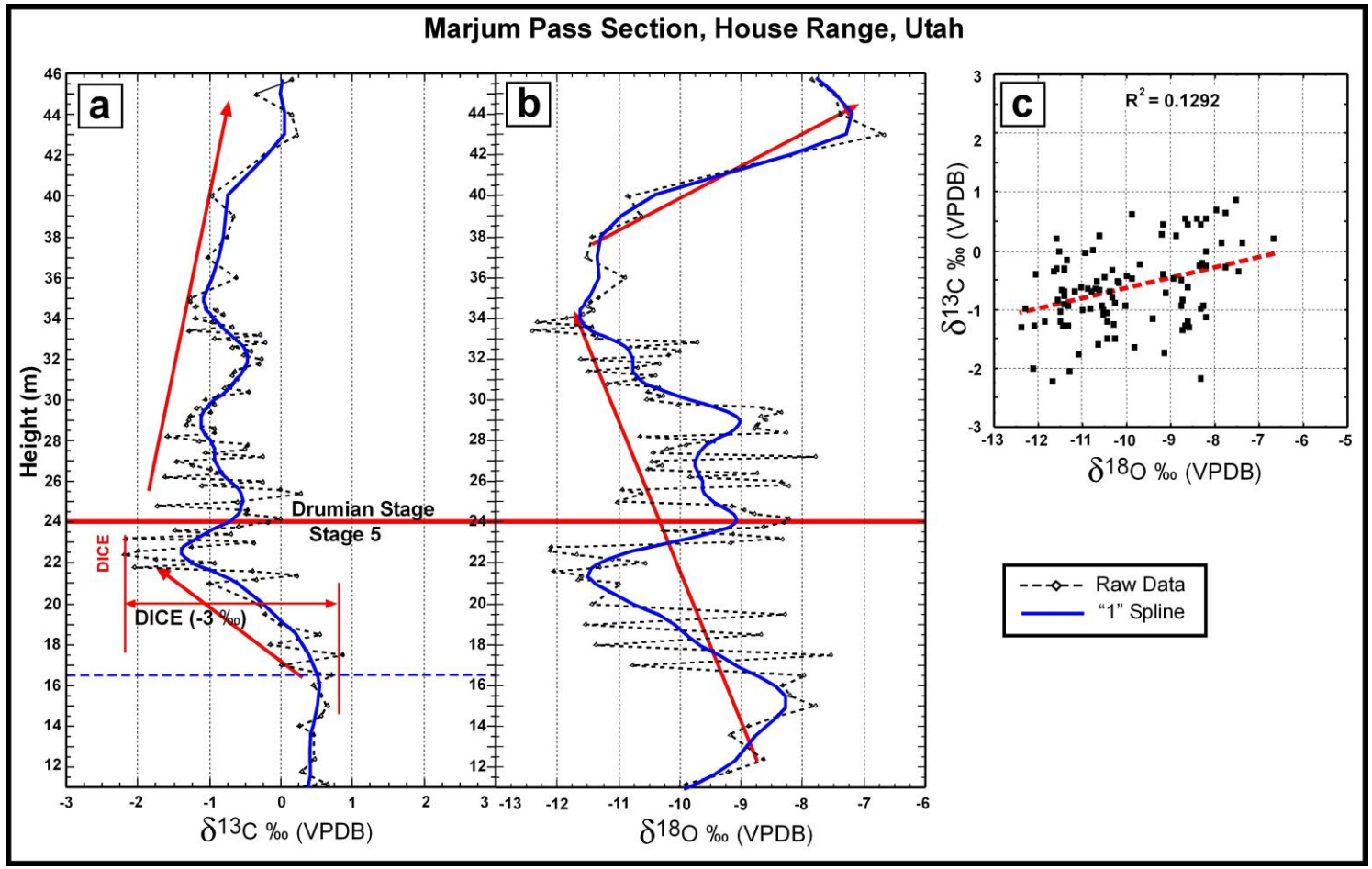

Figure 3.3. Three curves showing the isotopic results obtained from the Marjum Pass section. The features on the three curves, (a to c), are illustrated in the caption of figure 3.2. The base of Drumian Stage here is defined at 24 m (Chapter-II). The height of the Marjum Pass section is measured from the base of the Wheeler Formation.

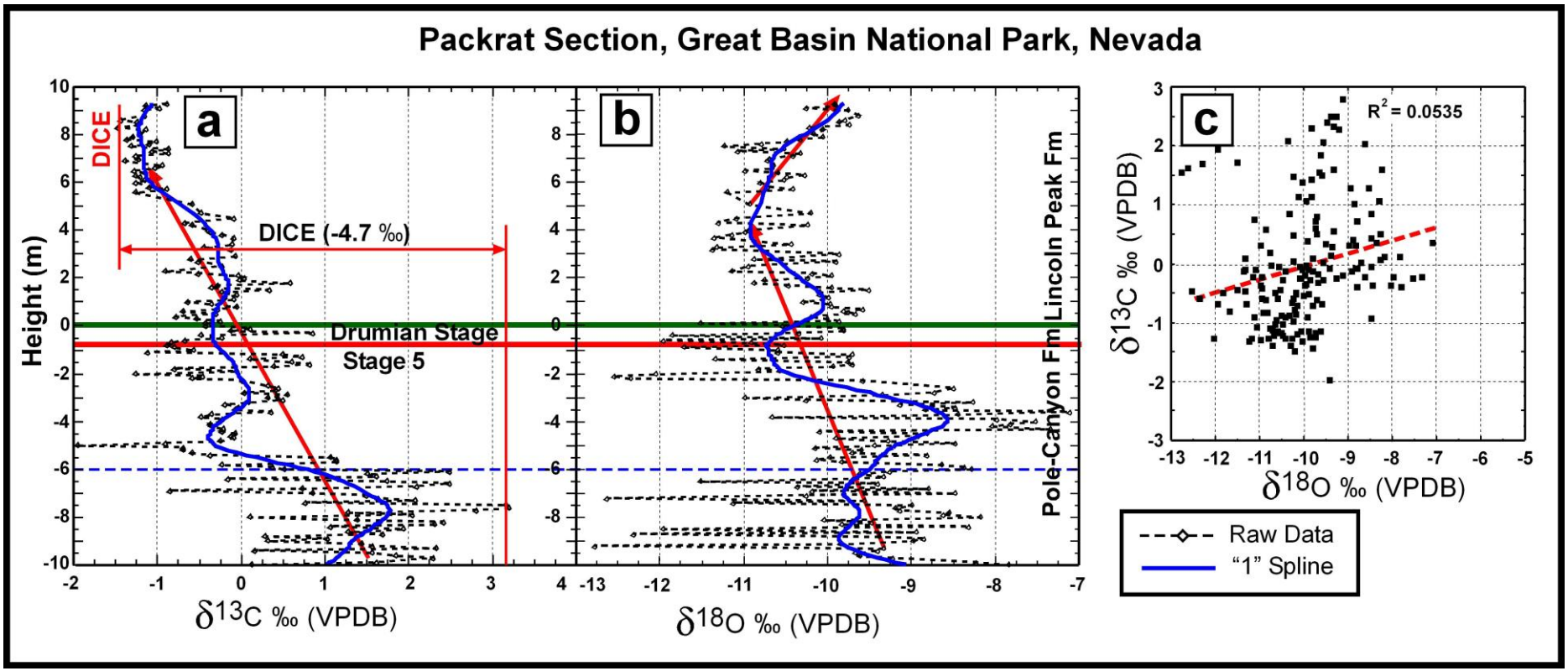

Figure 3.4. Three curves showing the isotopic results obtained from the Packrat section. The features on the three curves (a to c) are illustrated in the caption of figure 3.2. The base of Drumian Stage is defined at ~0.8 m (Chapter II) below the base of the Lincoln Peak Formation.

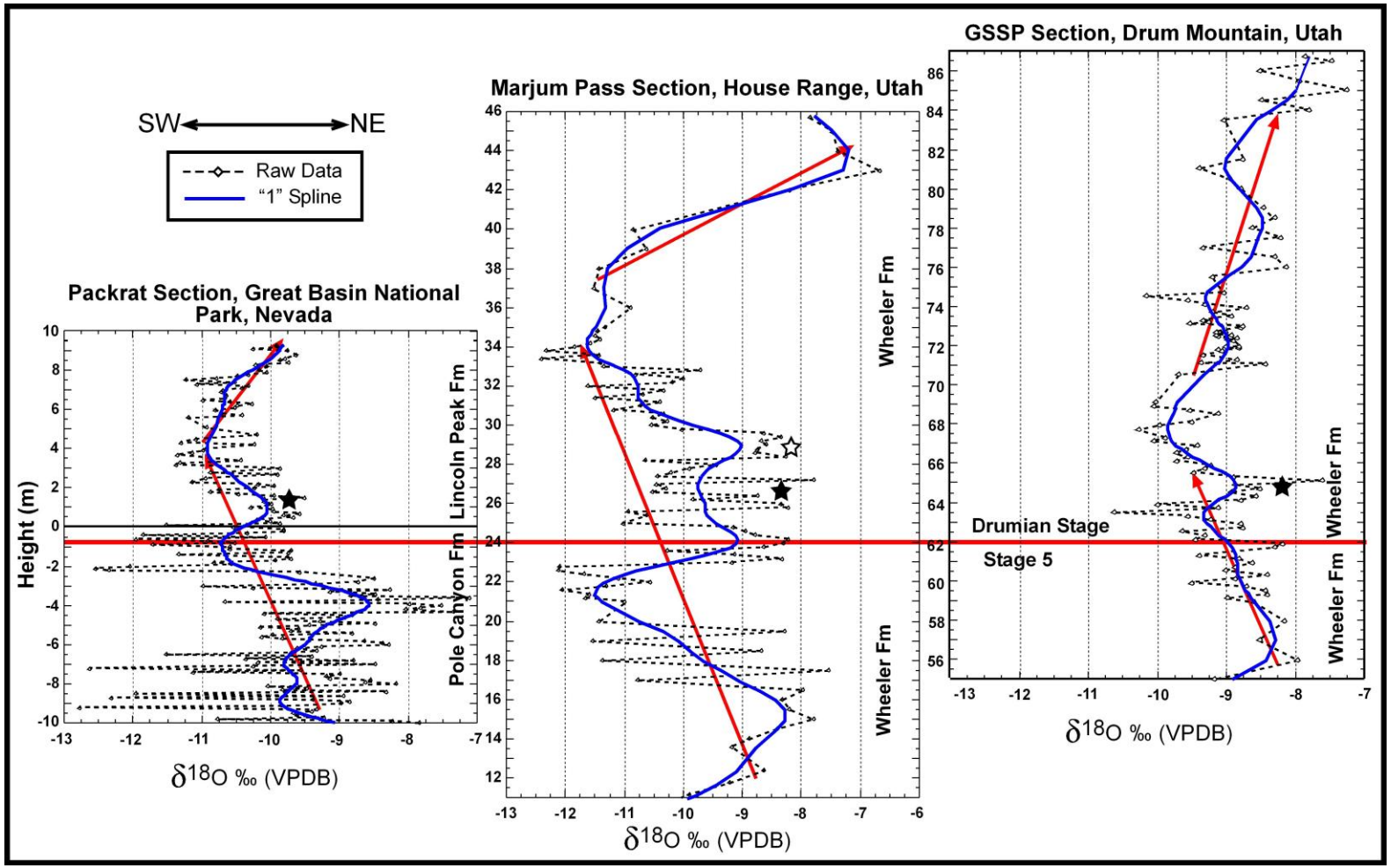

Figure 3.5. Three $\delta^{18}O$ curves showing high-resolution correlation among the three HRE sections; GSSP, Marjum Pass and Packrat. The black filled stars represent heavy isotopic intervals (peaks) above the base of the Drumian Stage. These have high correlation potential among the three sections and coincide with storm deposits. The open star at the Marjum pass section represents a heavy isotopic peak that coincides with a sea level fall and carbonate progradation to the embayment. The red arrows represent long-term changes in the $\delta^{18}O$ curves.

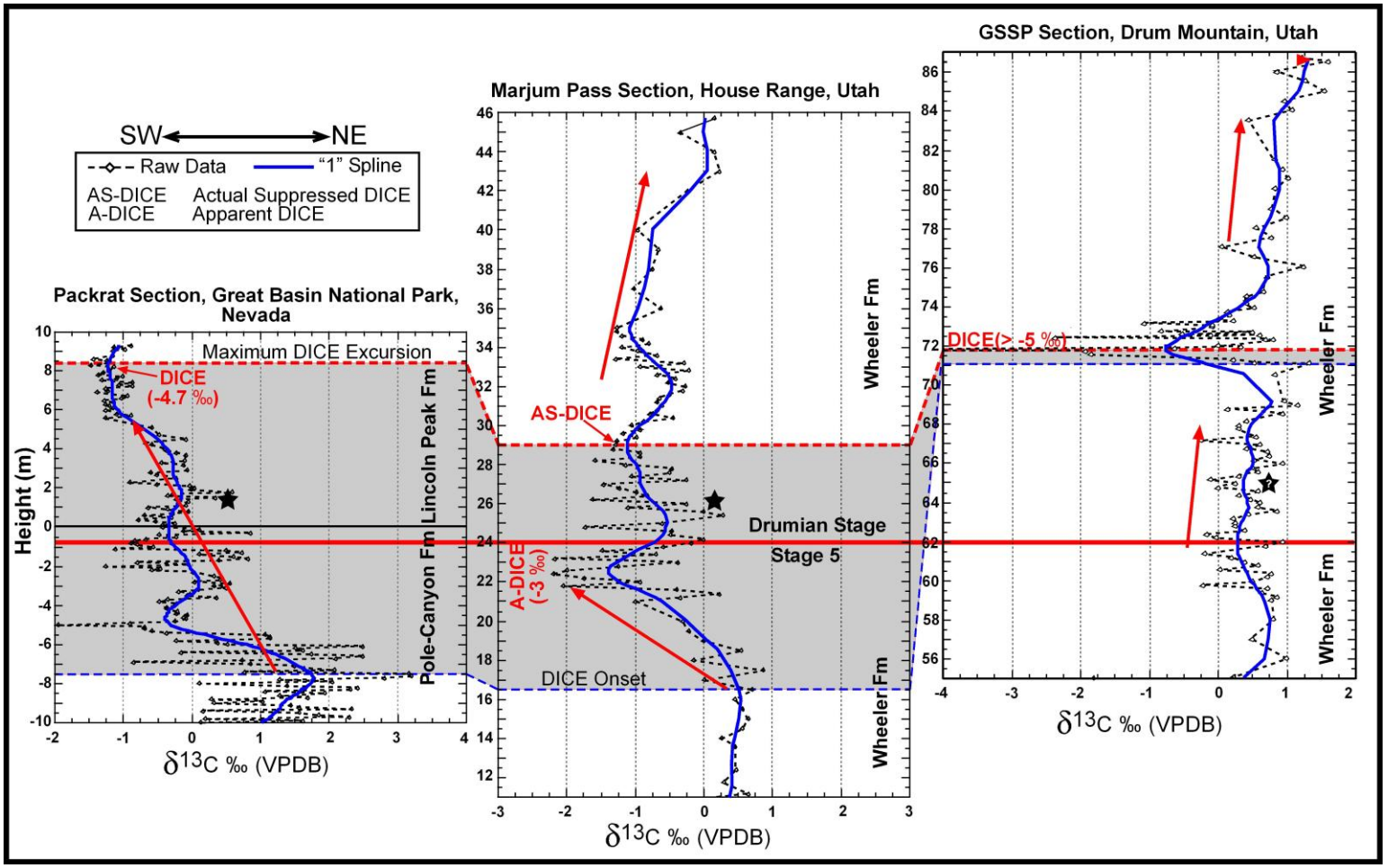

Figure 3.6. Three $\delta^{13}C$ curves showing high-resolution correlation among the HRE sections; GSSP, Marjum Pass and Packrat. Black filled stars represent heavy isotopic intervals (peaks) above the base of the Drumian Stage at the Packrat and Marjum Pass sections. The DICE maximum excursion and its onset are represented by the dashed red and blue lines respectively. The A-DICE is the apparent DICE and the AS-DICE represent the Actual Suppressed DICE. This carbonate layer suppresses the DICE signal because it has heavy isotopic values than its containing facies. The red arrows represent long-term changes in the $\delta^{13}C$ curves.

Most of $\delta^{18}O$ values exhibit ~4 ‰ ranges in all three sections except for the GSSP section where it shows ~2 ‰ range. $\delta^{18}O$ represent negative long-term excursion that is highlighted by the red arrows and correlates among the three sections (Fig. 3.5). However, the Packrat section does not show the following $\delta^{18}O$ increase because it is stratigraphically shorter than the other two sections. Multiple peaks are superimposed on the long-term decreasing trends, red arrows, showing a distinctive peak (black star) above the base of the Drumian Stage in all three sections (Fig. 3.5). This Peak is more prominent in the Marjum Pass section, showing higher amplitude and covering longer interval than its equivalents in GSSP and the Packrat sections. Another unique peak is observed at 4 m below the Pole-Canyon/Lincoln-Peak formations boundary in the Packrat section (Figs. 3.4-b and 3.5). This peak marks a debris flow that originated from up-ramp, shallower areas on the southern HRE ramp (Chapter-I), and isn't found in the other two sections.

$\delta^{13}C$ values have slightly more variability among the three sections than do $\delta^{18}O$ values (Fig. 3.6). In the GSSP section, $\delta^{13}C$ values range between 0‰ and 1‰ except at ~72 m above the base of the Wheeler Formation, where values fall to more than -5‰. $\delta^{13}C$ ranges between -2.2‰ and 0.8‰ in the Marjum Pass section, and between -1.5‰ and 3.2‰ in the Packrat section. $\delta^{13}C$ long-term changes also vary form one section to the other (Fig. 3.6). The GSSP section shows overall minor increases that are interrupted by a sharp, -5‰ $\delta^{13}C$ excursion at 72 m. In the Marjum Pass section, $\delta^{13}C$ decreases from ~0.8‰ at 16.5 m to reach a minimum (-2.2‰) at ~23 m above the base of Wheeler Formation, 1 m below the base of the Drumian Stage. Values then increase to ~0‰ at the top of the section. The Packrat section has a unique $\delta^{13}C$ signal, where values decrease gradually from ~3.2‰, at 7.5 m

below the Lincoln-Peak/Pole-Canyon formations boundary, to a minimum (-1.5‰) at 8.5 m above the same boundary, an overall shift of nearly -4.7‰ (Fig. 3.6). This signal started below and ended above the base of the Drumian Stage. Above the base of the Drumian Stage, $\delta^{13}C$ values exhibit heavy isotopic peaks (black star) in the Packrat and Marjum Pass sections, but this peak is absent in the GSSP section.

In summary, the position of the maximum negative $\delta^{13}C$ excursion varies in the three sampled sections relative to the base of the Drumian stage. It is located at 10 m and ~9.5 m above the base of the Drumian Stage in the GSSP and the Packrat sections, respectively, and 1 m below the same stage boundary at the Marjum Pass section. Moreover, the interval over which $\delta^{13}C$ decreases to its minimum values decreases along the HRE to the southwest from ~1 m (71 to 72) at the GSSP, to 6.5 m (16.5 to 23) at the Marjum Pass Section, to 16.5 m (-7.5 to 8.5) at the Packrat section (Figs. 3.1 and 3.6). Accordingly, the overall negative excursion is sharp in the GSSP section, moderate in the Marjum Pass section, and gradual in the Packrat section (Fig. 3.6). Furthermore, this interval straddles the base of the Drumian Stage in the Packrat section, is below the boundary in the Marjum Pass section, and above it in the GSSP section.

This negative $\delta^{13}C$ excursion was reported to be synchronous and represent the DICE in the GSSP and Marjum Pass sections (Babcock et al., 2004; 2007; Howley and Jiang, 2010), irrespective of its relation to the base of the Drumian stage or the LOOP of *P. atavus* in the Marjum Pass section. The DICE excursion is argued here to include the negative carbon isotope excursion observed in the Packrat section at ~9.5 m above the base of the Drumian Stage, because the three sections are well correlated based on χ and $CaCO_3$% signals as demonstrated by (Chapter-I). In addition, the Packrat $\delta^{13}C$ negative excursion lies within the expected range.

3.5. Discussion

Isotopic values for slope and basinal sections tend to fluctuate according to the major facies changes during sea level rise across the base of the Drumian Stage. In chapter-I the lithological variations among the three sections reported here have been studied in detail using χ and $CaCO_3$%. This results in tracing a series of layers across the HRE. $\delta^{13}C$ and $\delta^{18}O$ values covary with such lithologic variations and tend toward heavier values when higher $CaCO_3$% layers are encountered. These carbonate-rich layers were deposited either during storm events or during the carbonate platform progradation that follows maximum sea level rise (Chapter-I). In addition, $\delta^{18}O$ response to these carbonate dominated layers is more conspicuous than $\delta^{13}C$. Marjum Pass curve, for example, shows prominent $\delta^{18}O$ flat peak above the base of the Drumian Stage that is >3‰ heavier than its bounding $\delta^{18}O$ values, while $\delta^{13}C$ of the same interval is only ~1‰ heavier than its bounding $\delta^{13}C$ values and superimposed on the long-term $\delta^{13}C$ increase (Fig. 3.3).

Laterally, $\delta^{13}C$, like $\delta^{18}O$, behaves differently for the same layers at different localities. The shallow sections that are very close to the HRE northern edge (GSSP) or deep sections that are very close to the HRE trough (Packrat) have less isotopic variations than the lower-slope section of the northern HRE ramp (Marjum Pass). Above the base of the Drumian Stage, both the GSSP and Packrat sections show lower amplitude $\delta^{18}O$ and $\delta^{13}C$ peaks than their equivalent in Marjum pass section (Figs. 3.5 and 3.6). Another $\delta^{18}O$ peak is observed at 4 m below the Pole Canyon/Lincoln Peak formations boundary in the Packrat section. This peak coincides with the debris flow layer that originated from shallower areas on the southern HRE ramp. This $\delta^{13}C$ peak is less well defined and is only observed in the Packrat section (Chapter-I).

The overall lithological composition varies among the three studied sections. The GSSP is a carbonate-dominated section; Marjum Pass is a detrital-dominated section, and the Packrat section is mixed, being carbonate-dominated during Stage 5 and detrital-dominated during the Drumian Stage (Chapter-I). Higher carbonate percentages shift $\delta^{13}C$ signal to heavier values, delay the DICE onset to higher stratigraphic position, and accelerate the DICE ending to lower stratigraphic position within carbonate-dominated sections more than in detrital-dominated sections. Therefore, the DICE begins stratigraphically earlier in the Marjum Pass section and later in the GSSP and Packrat sections (Fig. 3.6). Likewise, it ends earlier in the GSSP section, and has its highest termination in the Packrat section because the Packrat is more detrital above the base of the Drumian Stage than the other two sections (Chapter-I). In addition, the $\delta^{13}C$ negative excursion tends to be more gradual and cover longer stratigraphic intervals within sections that are not frequently interrupted by deposition of carbonate-dominated layers (i.e., Packrat), versus those dominated by carbonate layers (i.e., GSSP) (Fig. 3.6). The DICE negative excursion is gradual in the Packrat section, moderate in the Marjum Pass section and very rapid in the GSSP section.

Multiple explanations have been provided for the DICE negative $\delta^{13}C$ excursion. Meteoric diagensis due to fresh-water supply, carbon recycling in restricted basins, and/or significant diagenetic modifications below sequence boundaries may account for $\delta^{13}C$ negative excursions (Allan and Matthews, 1982; Holmden et al., 1998; Panchuk et al., 2006; Theiling et al., 2007; Howley and Jiang, 2010). However, based on the results presented here, the most acceptable explanation for the DICE event is respiration and remineralization of organic matter (Patterson and Walter, 1994; Howley and Jiang, 2010) that is stored within the

Oxygen Minimum Zone (OMZ). It is likely that the OMZ was well developed across the base of the Drumian Stage within slope and basinal areas of the passive margin of western Laurentia. Accordingly, the HRE deep-water was poorly oxygenated, and the oxygen level decreased with depth until it reached minimum, dysoxic or possibly even anoxic levels, in the OMZ. Oxidation of organic matter is known to pump lighter carbon (^{12}C) into containing and surrounding water masses (Lloyd, 1964; Patterson and Walter, 1994; Panchuk et al., 2006). This process leads to $\delta^{13}C$ depletion of the dissolved inorganic carbon (DIC) in containing ocean water faster than other processes (Panchuk et al., 2006). In modern semi-restricted marine environments such as Florida Bay and the Bahamian Banks, $\delta^{13}C$ in sediments is observed to be more than 4‰ below the surrounding open-ocean water (Lloyd, 1964; Patterson and Walter, 1994). Ocean water above the HRE appears to have been stratified during deposition of the lower Wheeler Formation (Rees, 1986; Gaines and Droser, 2003; Gaines et al., 2005). However, the Laurentian shallow-water carbonate platform was deposited under well oxygenated conditions, because it is an extensive carbonate belt that was built up mainly from algal and/or microbial carbonate sediment (Palmer, 1971; Brady and Koepnick, 1979; Aitken, 1997).

It is known that the OMZ existed during the deposition of the Middle-Cambrian Wheeler Formation, and the low oxygen content of the HRE deep water is supported by multiple studies. The uninterrupted lamination of fine-grained shale and flaggy limestone facies, along with the abundance of carbon remains, indicate deposition under quiet and low dysoxic or even anoxic bottom water (Rees, 1986). However, the existence of pelagic agnostoid trilobites indicate that the HRE water was open to the marine currents (Rees, 1986). Also, the preservation of suspension laminae and the rare occurrences of unidirectional marks such as current-oriented fossils, and

sole and tool marks, suggest deposition under quiet and poorly oxygenated water within the OMZs (Rogers, 1984; Elrick and Snider, 2002). The abundance of organic preservation of nonmineralized macrofossils through meters-thick-intervals indicates the prevalence of anoxic events during the deposition of much of the Wheeler Formation (Gaines and Droser, 2003; Gaines et al., 2005). The opportunistic trilobite, Elrathia kingii, is observed in a few localities in the Middle-Cambrian Wheeler Formation where it inhabits the exaerobic zone; the boundary between dysoxic and anoxic deep-water zones (Savrda and Bottjer, 1987; Gaines and Droser, 2003). Burgess Shale-type deposits that contain well preserved assemblages of soft-bodied and nonmineralized fossils, *konservat-lagerstatten,* have been observed in the middle and upper Wheeler Formation in the House Range and Drum Mountains (Gaines et al., 2005; Halgedahl et al., 2009). This exceptional preservation is known to occur in low-energy dysoxic or anoxic deep water at maximum sea level rise, where low permeability clay-rich layers are deposited within a well-developed OMZ (Gaines et al., 2005; Halgedahl et al., 2009). A similar clay-rich, carbonate-poor interval is observed within the lower Wheeler Fm. above the base of the Drumian Stage (CP7, Figs. 3 and 4; Chapter-I). The Maximum DICE excursion is observed very close to this interval in the GSSP and Packrat sections.

Clearly, HRE slope and basinal areas were affected by poorly oxygenated deep water because they represent the inward extension of slope and basinal areas of the passive margin of western Laurentia (Rees, 1986). Carbonate isotopic values depend on the source of carbonates in the sections studied here. Carbonate sediments that originated in the well-oxygenated shallow water of shelf and upper slope areas, have heavier $\delta^{13}C$ and $\delta^{18}O$ values than those that originated close to or in the OMZ in downslope and trough areas. The latter refers to the pelagic carbonate

particles that are formed and deposited within the ^{12}C-rich HRE water. The DIC of HRE deep-water is expected to have much lower $\delta^{13}C$ values than the DIC of near-by shallow, well oxygenated, northern-platform water. Therefore, HRE-sourced carbonates are affected by the respiration and remineralization of organic matter, and their $\delta^{13}C$ and $\delta^{18}O$ are shifted toward lighter, more negative values than are northern-platform-sourced carbonates.

The onset of the DICE depends on the, 1) depth and location of each locality, 2) sea level, and 3) circulation pattern within the HRE. Shallow localities that are very close to the HRE northern edge, are flooded with carbonates that have heavier $\delta^{13}C$ and $\delta^{18}O$ than downslope and deep trough localities that are far from the HRE edge. As sea level rises, the OMZ gradually encroaches into the HRE toward the northeast, parallel to the HRE trough. Respiration and remineralization are initiated when the given locality is encroached upon by the organic matter included within the OMZ. Once the DICE is initiated, $\delta^{13}C$ continues to decrease as the OMZ gradually approaches each locality. The $\delta^{13}C$ decrease continuum is disturbed and suppressed by either rapid sea level falls or storm events. $\delta^{13}C$ is observed to increase during these circumstances because the HRE is flooded by isotopically heavier platform carbonates that are formed under shallow, well-oxygenated water. Turbidity currents carry the agitated sediments during storm events, and surface water currents deliver platform carbonate sediments to the HRE during times of sea level fall. This is aided by the carbonate factory advance over the HRE edge (Elrick and Snider, 2002).

The isotopic difference between storm layers and the containing sediments above the base of the Drumian Stage depends on the location of each section. This difference is less prominent in lower slope sediments of the southern ramp (Packrat),

and shallow sections that are close to the northern platform (GSSP section), because storm derived sediments are sourced from close-by areas that exhibit similar isotopic values (Fig. 3.6). However, this is more prominent in lower-slope sections of the northern ramp (Marjum Pass section), because storm sediments conserve their original isotopic signal down to deep dysoxic or anoxic water (Fig. 3.6). At the GSSP section, the storm layers and the containing sediment originated from the same shallow areas and were delivered over short distances, either by shelf currents that deliver the containing sediments or by storms as storm deposits. In the Packrat section, sediments were either eroded from areas that experienced dysoxic conditions, or were delivered by exhausted turbidity currents. These turbidity currents weakened as they move downslope, and the included sediments are buried within other $\delta^{13}C$ depleted sediments. In the Marjum Pass section, these storm deposits were formed in shallow well-oxygenated shelf water and then delivered to slope and basinal localities where the containing sediments were formed in the deep, poorly-oxygenated water of the HRE. As a consequence, the Marjum Pass section was isotopically more sensitive to facies changes than were the other two sections. In addition, the negative $\delta^{13}C$ excursion was likely dampened due to incoming, isotopically-heavy, carbonates (storm deposits). Given that the Marjum Pass section has its maximum negative $\delta^{13}C$ excursion, DICE, below the base of the Drumian Stage, while the other two sections have their maximum negative $\delta^{13}C$ excursion, DICE, ~10 m above the stage boundary (Fig. 3.6).

It is argued here that the Marjum Pass DICE event, which lies at 1 m below the base of the Drumian Stage, represents an Apparent DICE (A-DICE – Fig. 3.6) where the actual DICE is located 6 m above the base of the Drumian Stage, at ~30 m above the base of the Wheeler Formation (Fig. 3.6). This actual DICE was

probably suppressed by incoming, isotopically-heavy carbonates that were delivered to the HRE during the onset of the rapid sea level fall that follow the maximum sea level rise at that time. This Actual Suppressed DICE (AS-DICE) is stratigraphically synchronous with the maximum negative carbon isotope excursion, DICE, events observed in the other two sections. In addition, the AS-DICE coincide with the synchronous *P. atavus* acme in Marjum Pass section and the GSSP (Chapter-II). The interval between the base of the Drumian Stage and the DICE, or AS-DICE, event varies in thickness among the three studied sections due to the sediment accumulation rate (SAR) at each site. Therefore, the DICE event is a viable chronostratigraphic marker that precisely constrains the base of the Drumian Stage regionally in the HRE, however, it was occasionally suppressed by the flux of isotopically-heavy shelf carbonates that were delivered to sites during sea level fall and/or storm events.

3.6. DICE correlation between Laurentian platform and basinal sections

The DICE or AS-DICE anomaly provides a reasonably good chronostratigraphic marker that precisely constrains the base of the Drumian Stage when used along with other high-resolution data sets such as χ and $CaCO_3$% content within the HRE (for more details, see Chapter-I). The DICE in the Middle-Cambrian carbonate platform sections is still enigmatic and its stratigraphic position relative to slope and basinal DICE stratigraphic position is uncertain. The complex lithological relationship between HRE and platform sections, as well as the absence of agnostoid trilobites on the shelf, add more challenges when correlating between basinal and platform sections (Howley and Jiang, 2010).

Those published $\delta^{13}C$ data for the DICE interval on the southern Laurentian carbonate platform (Howley, 2010; Howley and Jiang, 2010) are used here for

comparison. This data set represents three southern platform sections (Wah Wah, Panaca Hills and Desert Range). Sparry cement samples, most sample replicas, and the individual data points that show high correlation potential between $\delta^{13}C$ and $\delta^{18}O$ have been removed in figure 3.7 (modified from Howley, 2010; Howley and Jiang, 2010). The height of each section is adjusted to the closest formations or members boundary. The base of the Papoose Lake/Banded Mountain members boundary, Medow Valley/Condor members boundary, and Eye of Needle Limestone/Pierson Cove Formations boundary are held as three stratigraphic datums for Desert Range, Panaca Hills, and Wah Wah sections, respectively (Fig. 3.7). These data, along with our high-resolution data set, are used to assess Laurentian platform to basin correlation. This work also aims to provide a reasonable explanation for the existence of the DICE on carbonate platform sections (Figs. 3.6 and 3.7).

The platform-to-basin $\delta^{13}C$ data sets are presented in figures 3.6 and 3.7. DICE thickness is observed to change through these six sections. In slope and basinal sections, the DICE thickness is highest close to the HRE mouth and decreases in the northeasterly direction as the width and depth of the HRE decreases (Fig. 3.6). Even though, the Packrat section doesn't cover the entire DICE interval, it is clear that it has the highest DICE thickness because the interval over which $\delta^{13}C$ decreases to its minimum is about three times its equivalent in the Marjum Pass section (Fig. 3.6). DICE records its lowest thickness in the GSSP section, although it was reported to be an expanded section and have high SARs (Babcock et al., 2007; Howley and Jiang, 2010) (Fig. 3.6). In the southern platform sections, the DICE thickness is observed to decrease away from the HRE from Wah Wah through Panaca Hills to Desert Range sections (Figs. 3.1 and 3.7). Even

though the DICE increasing limb in Desert Range section is poorly represented, the thickness of the DICE decreasing limb is observed to decrease away from the HRE (Fig. 3.7). In summary, DICE thickness decreases away from the HRE mouth in slope and basinal sections, and away from the southern edge of the HRE in southern carbonate platform sections.

Circulation pattern, sea level changes, and paleogeographic configuration are the factors that account for the existence of DICE on the carbonate platform when the OMZ was well developed in slope and basinal areas around the base of the Drumian Stage. Ocean surface currents that were driven by the trade winds, likely drove the HRE poorly-oxygenated, $\delta^{13}C$-depleted water to the southern carbonate platform. This water imprinted the platform carbonates with low $\delta^{13}C$ and $\delta^{18}O$ values due to respiration and remineralization of included organic matter. This hypothesis is supported by, 1) the upwelling of HRE deep dysoxic water that is known to increase during sea level rise (Howley and Jiang, 2010), and 2) the Coriolis Effect that deflects northeastward moving HRE bottom water to the right, southward, parallel to trade winds direction.

The HRE paleogeographic configuration helps the surface currents to drag the ^{12}C-rich, poorly-oxygenated HRE water to the southern carbonate platform where it mixes with the platform well-oxygenated water. The HRE is a fault-controlled embayment that cuts through the Laurentian carbonate platform and extends more than 400 km in the northeasterly direction, perpendicular to the trade wind direction (Rees, 1986) (Fig. 3.1). Because the OMZ rises close to HRE edges during maximum sea level rise, mixing occurs between the poorly oxygenated organic rich the HRE deep water and well oxygenated surface water. The mixing ratio increases during sea level rise and peaks and is expected to peak at maximum sea level rise

and records the DICE maximum negative excursion in all platform sections. It is likely that this ratio decreases southward away from the HRE due to additional mixing with the southern platform shallow water. The DICE minimum $\delta^{13}C$ values are likely to be synchronous within the embayment and platform sections. The Marjum Pass section is an exception because the actual DICE is suppressed by incoming heavier isotopic-value carbonates. High-resolution χ, Total Organic Carbon (TOC), and $CaCO_3$% content analyses make it possible to examine the extent to which OMZ is elevated during maximum sea level rise across the platform DICE.

The absence of $\delta^{13}C$ depleted values within the GSSP carbonate-dominated intervals at the time when it is recorded within the Marjum Pass and the Packrat section, explains DICE absence in northern platform sections (Fig. 3.6). These carbonates are shed off the northern carbonate platform by shelf currents that were driven by trade winds, and flooded sections that were close to the HRE northern edge during carbonate factory progradation and sea level fall (Chapter-I; Elrick and Snider, 2002). Accordingly, the DICE interval is expected to shrink even more within HRE sections that are very close to the northern edge. Because DICE can be easily missed in these sections, high-resolution sampling is required when the DICE is targeted. However, the DICE is recorded within the carbonate-dominated southern platform sections because the paleogeographic configuration of the embayment allowed HRE $\delta^{13}C$ depleted water to be dragged over the southern platform by the same shelf currents and therefore imprint their isotopic signal.

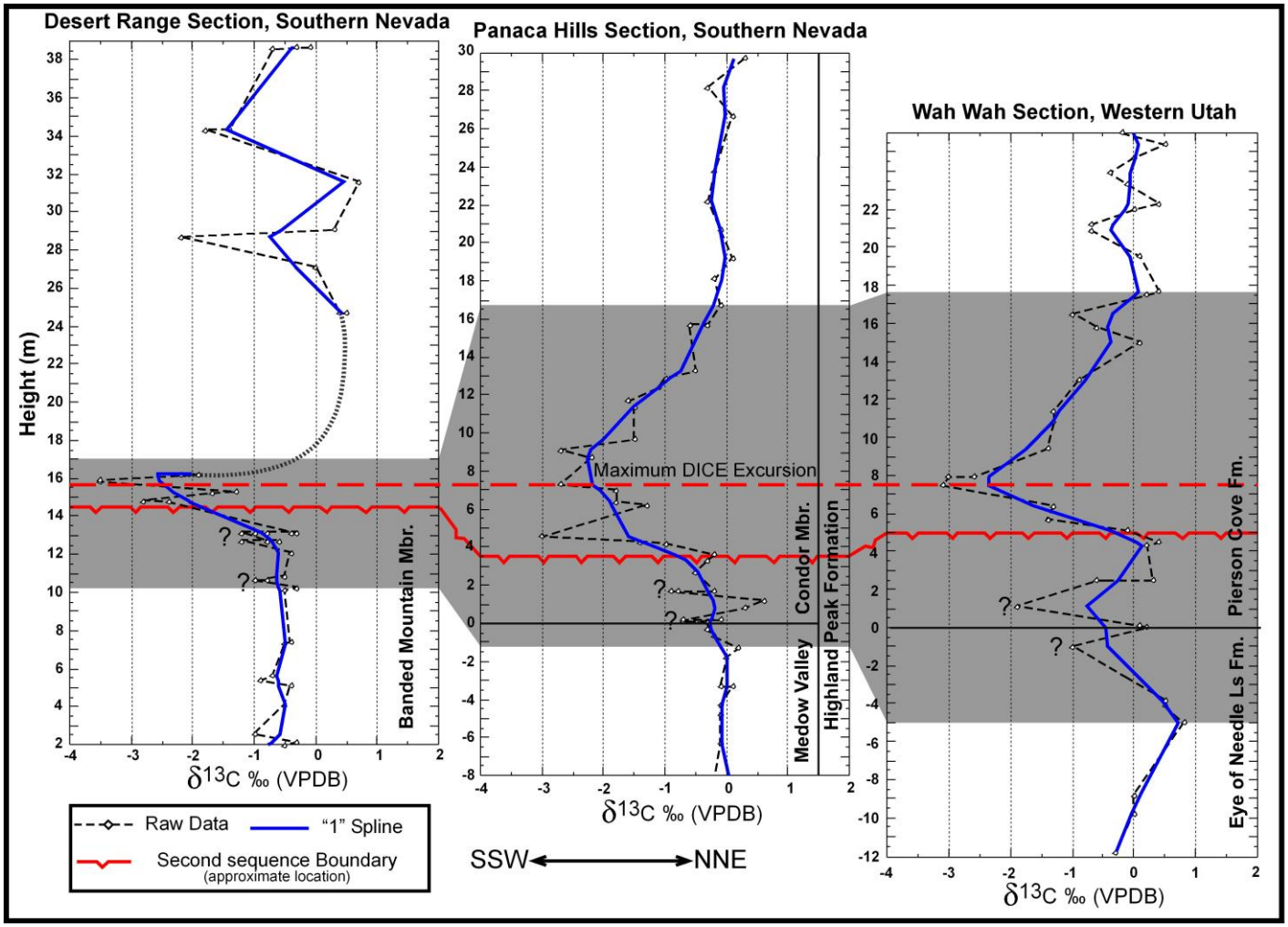

Figure 3.7. Three curves showing high-resolution correlation among the platform sections; Wah Wah, Panaca Hills and Desert Range, data modified and redrawn from Howley (2010) and Howley and Jiang (2010). The DICE range is expressed as grey shaded boxes that are correlated among the three sections. In addition, the DICE maximum excursion and the second unconformity are also represented.

3.7. The base of the Drumian Stage on the Laurentian carbonate platform

The basal boundary of the Drumian Stage is placed at the base of the first of three storms layers in slope and basinal sections (Chapter-I). This boundary marks an erosional surface that lies below the maximum negative $\delta^{13}C$ excursion, DICE, at the GSSP section. The GSSP is reported to be a shallow trough section that is very close to the carbonate platform edge (Chapter-I). The high-energy turbidity currents that were initiated by the first storm event accounts for the formation of the Drumian eroded base. It was driven by the seafloor slope-angle and the density difference between the current and surrounding HRE seawater (Chapter-I). It is expected that the same storm event should have created a synchronous, more intensive, erosional surface on the carbonate self below the maximum negative $\delta^{13}C$ excursion, DICE minimum $\delta^{13}C$ values. Multiple erosional surfaces, including the second sequence boundary, have been observed below the DICE in the southern carbonate platform sections (Howley and Jiang, 2010), where the three storm deposits are observed in the HRE sections. Any of these erosional surfaces is likely to represent the base of the Drumian Stage. Because both the base of the Drumian Stage and the maximum negative $\delta^{13}C$ excursion are synchronous in the HRE and platform sections, the interval between them fluctuates among all sections depending upon the SAR. While HRE results are based on high-resolution sampling, this has not been performed on southern platform sections. Therefore, high-resolution correlation is needed to determine which erosional surface in the southern platform sections represents the base of the Drumian Stage.

Tracing the base of the Drumian Stage to an erosional surface on the southern carbonate platform of the HRE is supported by multiple arguments. First, it is placed at an erosional surface in the GSSP section. Second, multiple erosional

surfaces have been reported below the maximum DICE excursion in southern platform sections (Howley and Jiang, 2010), while three storm deposits are observed below this maximum excursion in HRE sections (Chapter-I). Third, the first storm event is expected to be strong enough to produce an extensive erosional surface, which might have produced lag deposits on the carbonate platform because the turbidity current delivered calcisiltite sediments to the GSSP section. In addition, the first storm layer is observed in the Packrat section where the two succeeding storm layers are either diminished or were not deposited at all (Chapter-I). Even though some grainstone/packstone lag deposits are observed associated with platform erosional surfaces (Howley and Jiang, 2010), more petrographical work is needed to identify those lag deposits within or slightly below the DICE event.

3.8. Regional to global DICE correlation

The DICE signal marks a global event because the DICE is observed in the platform and slope sections in northern and southern China (Zhu et al., 2004). In the Wangcun slope section in China, a negative $\delta^{13}C$ excursion starts within the Aoxi Formation and reaches its minimum values within the lower member of the overlying Huaqiao Formation (Fig. 8 modified from Zhu et al., 2004). In addition, the LOOP of *P. atavus* there marks the base of a $\delta^{13}C$ increase that coincides with a lithological change (Fig. 3.8). The associated facies and $\delta^{13}C$ signal are similar to those found in HRE sections. The facies changes in the Wangcun section begin with black shale with increasing amounts of dark gray, thin-bedded limestone interbeds, changing to dark gray, thin-bedded limestone, that lacks black shale interbeds, close to the LOOP of *P. atavus* (Peng et al., 2004) (Fig. 3.8).

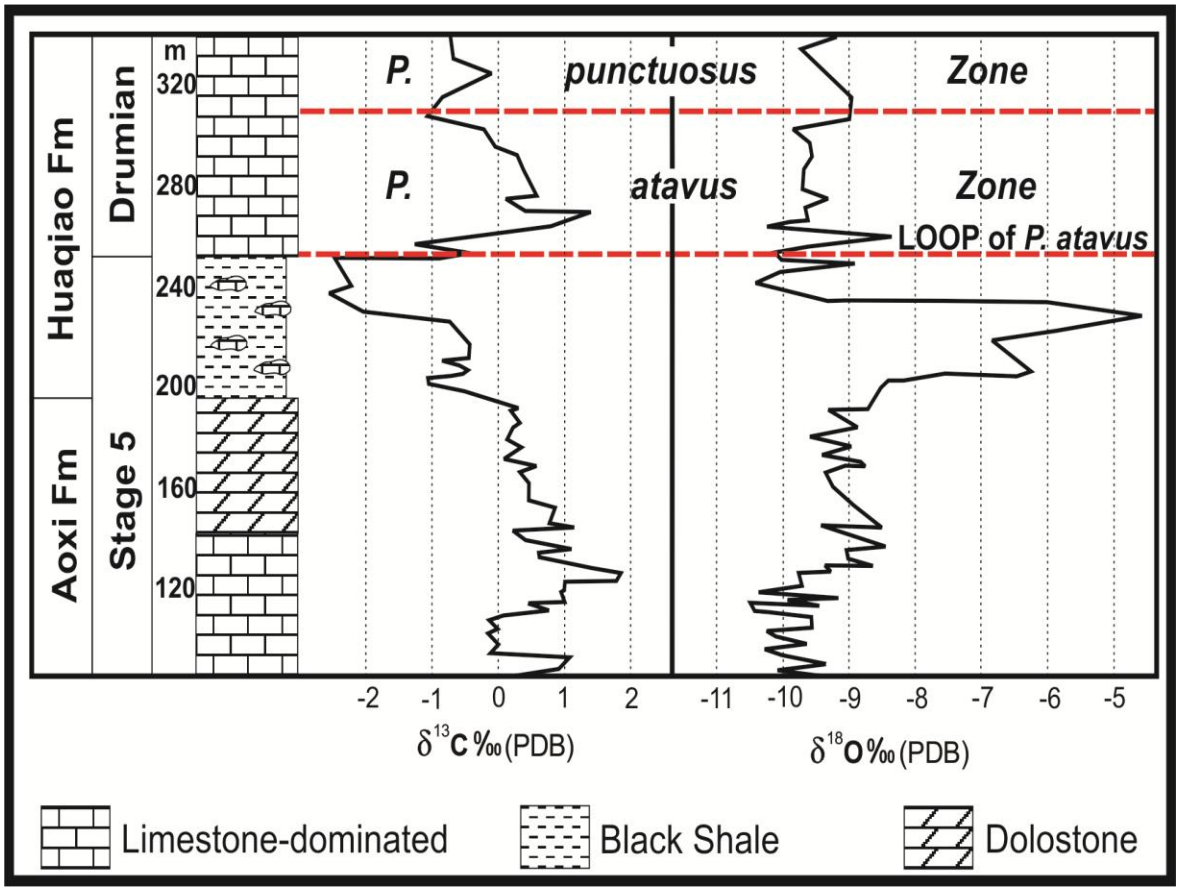

Figure 3.8. Chemostratigraphic diagram of the Middle-Cambrian Wangcun section, western Hunan Province, China showing $\delta^{13}C$ and $\delta^{18}O$ data, and the associated facies and bizones (modified from Zhu et al., 2004). The Lowest Observed Occurrence Point (LOOP) of *Ptychagnostus atavus* lies at the base of a carbonate-rich interval where $\delta^{13}C$ increases rapidly to reach pre-DICE levels. The Maximum DICE excursion is observed within a clay-rich interval, at the base of the carbonate-rich interval. This signal is similar to its counterpart in HRE sections.

In HRE sections, $\delta^{13}C$ decreases to reach its minimum within detrital-dominated facies, and increases within carbonate dominated facies. In addition, regional lithofacies and sedimentary pattern studies reveal that the broad, extensive Yangtze carbonate platform gave way to an ocean-facing-slope and poorly-oxygenated deep-water basin (Peng and Babcock, 2001). Consequently, the factors that account for the DICE existence in the platform and basinal sections of western Laurentia, likely held true for its existence on the platform and slope sections of south China region. High-resolution χ, $CaCO_3$%, and chemostratigraphic analyses are needed to confirm this hypothesis.

3.9. The DICE Model

The DICE model provides an explanation for the existence of DICE in HRE and platform sections of western Laurentia (Fig. 3.9). This model assumes, 1) the existence of a well-developed, organic-rich, OMZ across the base of the Drumian stage during a time of sea level rise, and 2) that the trade winds were the main driver of surface currents over the Laurentian carbonate platform. The existence of the OMZ and trade winds during the deposition of the Middle-Cambrian Wheeler Formation is supported by multiple studies (Rogers, 1984; Rees, 1986; Savrda and Bottjer, 1987; Elrick and Snider, 2002; Gaines and Droser, 2003; Gaines and Droser, 2005; Gaines et al., 2005; Halgedahl et al., 2009; Howley and Jiang, 2010).

During lowstand, HRE and platform water masses are considered as one water mass that is driven by northerly (using today's coordinates) trade winds (Fig. 3.9, stage 1). Therefore, the HRE was covered by shallow, well-oxygenated water where isotopically heavy, carbonate-dominated facies were formed. During sea level rise, the organic-rich OMZ encroached the HRE through the HRE mouth and mixed with the well-oxygenated platform water (Fig. 3.9, stage 2). Oxidation of the OMZ organic matter pumped light carbon (^{12}C) into HRE water and produced more $\delta^{13}C$-depleted water than existed in surrounding platform water. Carbonates formed in such an environment were more $\delta^{13}C$ depleted than those formed in a shallow, isotopically heavy northern platform environment.

The paleogeographic configuration of the HRE, being perpendicular to surface currents directions, and the upwelling that increased during sea level rise, expedite this process. Consequently, the negative $\delta^{13}C$ excursion is proportional to the degree of respiration and remineralization of the organic matter. During maximum sea level rise, maximum respiration occurs because the OMZ rises to its highest level at or

close to HRE edges (Fig. 3.9, stage 3). It is likely that the maximum negative $\delta^{13}C$ excursion occurs during this interval. These three steps are expected to have reversed and mark $\delta^{13}C$ increases during subsequent sea level falls.

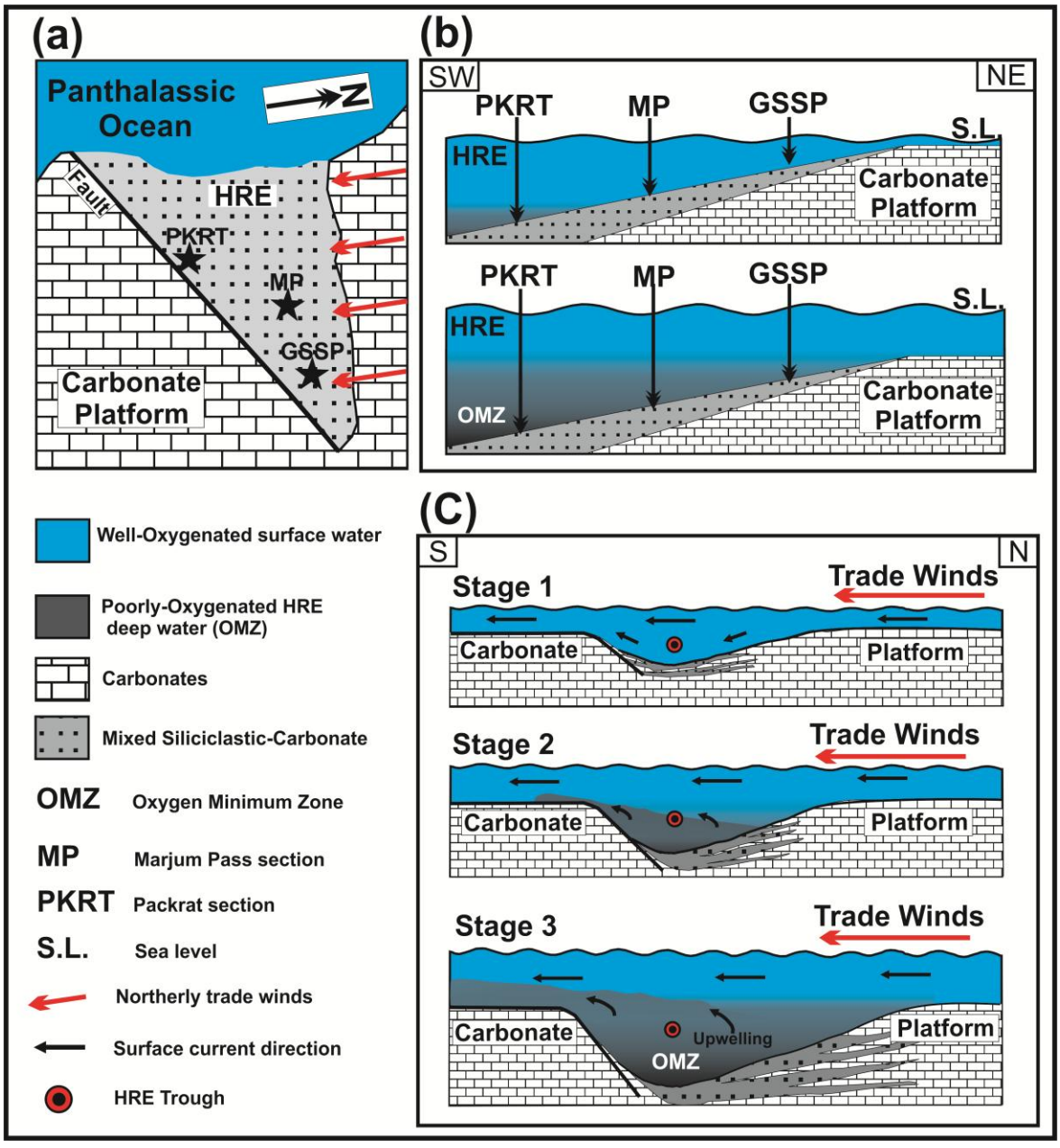

Figure 3.9. Hypothetical model illustrating the formation of the DICE interval in HRE and Platform sections of western Laurentia. The red dots represent the HRE trough. Both sea level and water depth increase from stage 1 to 3. The light blue color represents the shallow well-oxygenated water. The dark grey color represents deep, poorly oxygenated HRE water. The middle bright blue color represents mixed water from the two water-mass end members. Arrows show the direction in which shallow and deep-water masses move.

In HRE sections, the DICE starts when the locality is encroached upon by $\delta^{13}C$ depleted water, then maximizes at the point of maximum sea-level rise, where maximum respiration occurs, and ends during the subsequent sea-level fall when the OMZ abandons the locality, and $\delta^{13}C$-depleted water is replaced by $\delta^{13}C$-enriched water. In platform sections, $\delta^{13}C$-depleted water from the HRE is driven to the southern platform by surface currents and imprinted the platform carbonate with low $\delta^{13}C$ values. Therefore, the maximum DICE excursion is likely to be synchronous in the HRE and platform sections because their sites are controlled by the same factors during the maximum sea level rise. However, both the onset and the end of the DICE is observed to be diachronous among the studied sections when high-resolution correlation is applied. Because the depth and width of the HRE decreases in the northeasterly direction, the OMZ and $\delta^{13}C$-depleted waters encroach and/or abandon different localities at different times during sea level rise and/or fall. In addition, the DICE signal is sporadically suppressed during storm events because storms erode and deliver northern platform $\delta^{13}C$-rich carbonates to HRE $\delta^{13}C$-depleted carbonates. Thus, it is inferred here that the OMZ was well-developed within the slope and basinal areas of the shelf margin of western Laurentia and either, 1) short-lived only across the base of the Drumian Stage, imprinting HRE and southern platform sections during this particular sea level rise over any other sea level rise, or 2), long-lived during the Middle-Cambrian, and sea level rose to an unprecedented level during deposition of the base of the Drumian Stage, elevating the OMZ to unprecedented levels. This, in turn, allowed deep-water mixing with well-oxygenated shallow water, and initiated respiration and mineralization of the included organic matters. To examine which of these two hypotheses accounts for the global existence of the DICE event, high-resolution correlation among intervals of similar

depositional environments within the Wheeler Formation is required. Halgedahl et al. (2009) reported a similar clay-rich, carbonate-poor, interval in upper Wheeler Formation sediments, at ~230 m from its base. They called this interval the “hot zone” because it had exceptional preservation potential. The SAR in this “zone” indicates that it is more expanded than is the Drumian GSSP interval. In addition, it is also preceded by three carbonate layers that are similar to the three lower Wheeler Fm. storm layers.

3.10. Conclusions

The DICE is a chronostratigraphic marker that constrains the base of the Drumian Stage in the House Range Embayment (HRE) and surrounding southern carbonate platform sections. The DICE maximum excursion point should be used for correlation among Laurentian sections because it marks the maximum sea level rise after the base of the Drumian Stage. However, the onset and the end of the DICE are diachronous among the studied sections, and should not be used for stratigraphic correlation between multiple localities when high resolution is desired. The GSSP section provides the most practical example of the diachronicity of the DICE. The DICE in the GSSP section starts later and ends earlier than at other sections. Also, the GSSP is the last locality that was encroached upon by the Oxygen Minimum Zone (OMZ) during sea level rise, and the first to be abandoned during sea level fall. Consequently, the GSSP DICE covers a smaller interval than its equivalent in other sections. The location of the GSSP section dictates this effect. It is a shallow trough section that is flooded by heavier-isotopic carbonates during storm events, sea level fall, and early stages of sea level rise, while the other two HRE sections studied here reside in deeper poorly oxygenated, $\delta^{13}C$-depleted, water.

The maximum DICE excursion is observed only at maximum sea level rise that follows the base of the Drumian Stage in the HRE and the platform sections, unless occasionally suppressed by the incoming heavier-isotopic carbonates. Marjum Pass section provides a case for DICE suppression, where carbonate-dominated storm layers shift $\delta^{13}C$ signal temporarily toward heavier values.

The DICE is interpreted to result from respiration and remineralization of organic matter that is included in the OMZ. This process pumps light carbon into the HRE water mass and accounts for $\delta^{13}C$ depletion within the HRE and platform sections. It is inferred that the OMZ was well-developed, either 1) only across the base of the Drumian Stage and imprinted HRE and southern platform sections only during the sea level rise that occurred when the FAD of *P. atavus* also occurred, or 2), during the Middle-Cambrian, and sea level rose to an unprecedented level at the Drumian Stage FAD, elevating the OMZ to unprecedented levels. The DICE is observed on the southern platform because HRE poorly oxygenated, ^{12}C-rich deep water was dragged across the carbonate platform by surface currents that were driven by the trade winds. As a result, the base of the Drumian stage is expected to lie at the base of one of several erosional surfaces that lie below the maximum negative $\delta^{13}C$ excursion on the southern carbonate platform that were observed by Howley (2010). In addition, the DICE interval is likely to shrink in sections that are close to the HRE northern edge and disappear within the northern platform sections.

3.11. References

Ahlberg, P.E.R. et al., 2009. Cambrian high-resolution biostratigraphy and carbon isotope chemostratigraphy in Scania, Sweden: first record of the SPICE and DICE excursions in Scandinavia. Lethaia, 42(1): 2-16.

Aitken, J.D., 1997. Stratigraphy of the Middle Cambrian plat-formal succession, southern Rocky Mountains. Geol. Surv. Can. , 398: 322

Allan, J.R., Matthews, R.K., 1982. Isotope signatures associated with early meteoric diagenesis. Sedimentology, 29(6): 797-817.

Babcock, L.E., Peng, S., Geyer, G., Shergold, J.H., 2005. Changing perspectives on Cambrian chronostratigraphy and progress toward subdivision of the Cambrian System. Geosciences Journal [Seoul], 9(2): 101-106.

Babcock, L.E., Rees, M.N., Robison, R.A., Langenburg, E.S., Peng, S., 2004. Potential Global Standard Stratotype-section and Point (GSSP) for a Cambrian stage boundary defined by the first appearance of the trilobite *Ptychagnostus atavus*, Drum Mountains, Utah, USA. Geobios, 37(2): 149-158.

Babcock, L.E., Robison, R.A., Rees, M.N., Peng, S., Saltzman, M.R., 2007. The global boundary stratotype section and point (GSSP) of the Drumian Stage (Cambrian) in the Drum Mountains, Utah, USA. Episodes, 30(2): 85-95.

Brady, M.J., Koepnick, R.B., 1979. A Middle Cambrian platform-to-basin transition, House Range, West central Utah. Geology Studies, 26, Part 1: 1-7.

Dickinson, W.R., 1981. Plate tectonics and the continental margin of California. in Ernst, W.G., ed., The Geotectonic Development of California, Prentice-Hall, Upper Saddle River, New Jersey: 1–28.

Elrick, M., Snider, A.C., 2002. Deep-water stratigraphic cyclicity and carbonate mud mound development in the Middle Cambrian Marjum Formation, House Range, Utah, USA. Sedimentology, 49(5): 1021-1047.

Gaines, R.R., Droser, M.L., 2003. Paleoecology of the familiar trilobite Elrathia kingii; an early exaerobic zone inhabitant. Geology [Boulder], 31(11): 941-944.

Gaines, R.R., Droser, M.L., 2005. New approaches to understanding the mechanics of Burgess Shale-type deposits; from the micron scale to the global picture. Sedimentary Record, 3(2): 4-8.

Gaines, R.R., Kennedy, M.J., Droser, M.L., 2005. A new hypothesis for organic preservation of Burgess Shale taxa in the middle Cambrian Wheeler Formation, House Range, Utah. Palaeogeography, Palaeoclimatology, Palaeoecology, 220(1-2): 193-205.

Halgedahl, S.L., Jarrard, R.D., Brett, C.E., Allison, P.A., 2009. Geophysical and geological signatures of relative sea level change in the upper Wheeler Formation, Drum Mountains, west-central Utah; a perspective into exceptional preservation of fossils. Palaeogeography, Palaeoclimatology, Palaeoecology, 277(1-2): 34-56.

Hintze, L.F., 1988. Geologic history of Utah. Brigham Young University geology studies. Special publication: 7. Provo, Utah : Dept. of Geology, Brigham Young University, c1988.

Holmden, C., Creaser, R.A., Muehlenbachs, K., Leslie, S.A., Bergstrom, S.M., 1998. Isotopic evidence for geochemical decoupling between ancient epeiric seas

and bordering oceans; implications for secular curves. Geology [Boulder], 26(6): 567-570.

Howley, R.A., 2010. Sequence and chemostratigraphy of the Middle Cambrian succession in Nevada and Utah, United States.

Howley, R.A., Jiang, G., 2010. The Cambrian Drumian carbon isotope excursion (DICE) in the Great Basin, western United States. Palaeogeography, Palaeoclimatology, Palaeoecology, 296(1-2): 138-150.

Howley, R.A., Rees, M.N., Jiang, G., 2006. Research paper: Significance of Middle Cambrian mixed carbonate-siliciclastic units for global correlation: southern Nevada, USA. Palaeoworld, 15: 360-366.

Langenburg, E.S., 2003. The Middle Cambrian Wheeler Formation; sequence stratigraphy and geochemistry across a ramp-to-basin transition, United States.

Lloyd, R.M., 1964. Variations in the oxygen and carbon isotope ratios of Florida Bay mollusks and their environmental significance. Journal of Geology, 72(1): 84-111.

Palmer, A.R., 1971. The Cambrian of the Great Basin and adjacent areas, western United States. Wiley-Intersci., London-New York, International, pp. 1-78.

Panchuk, K.M., Holmden, C.E., Leslie, S.A., 2006. Local controls on carbon cycling in the Ordovician Midcontinent region of North America, with implications for carbon isotope secular curves. Journal of Sedimentary Research, 76(2): 200-211.

Patterson, W.P., Walter, L.M., 1994. Depletion of 13C in seawater sigmaCO2 on modern carbonate platforms: Significance for the carbon. Geology, 22(10): 885.

Peng, S., Robison, R.A., 2000. Agnostid biostratigraphy across the Middle-Upper Cambrian boundary in Hunan, China. Paleontological Society : Lawrence, KS, United States, United States.

Peng, S.C., Babcock, L.E., 2001. Cambrian of the Hunan-Guizhou region,nSouth China. In: Peng, S.C., Babcock, L.E., Zhu, M.Y. (Eds.), Cambrian System of South China. Press of University of Science and Technology of China, Hefei: 3–51.

Peng, S.C., Babcock, L.E., H.L., L., 2004. Polymerid Trilobites from the Cambrian of Northwestern Hunan, China. Volume 1: Corynexochida, Lichida, and Asaphida. Science Press, Beijing: 333.

Rees, M.N., 1984. A fault-controlled trough through a carbonate platform, Middle Cambrian House Range embayment, Utah and Nevada, United States.

Rees, M.N., 1986. A fault-controlled trough through a carbonate platform; the Middle Cambrian House Range Embayment. Geological Society of America Bulletin, 97(9): 1054-1069.

Robison, R.A., 1982. Some Middle Cambrian agnostoid trilobites from western North America. Journal of Paleontology, 56(1, Part 1): 132-160.

Rogers, J.C., 1984. Depositional environments and paleoecology of two quarry sites in the Middle Cambrian Marjum and Wheeler formations, House Range, Utah. Geology Studies, 31(1): 97-115.

Savrda, C.E., Bottjer, D.J., 1987. The exaerobic zone, a new oxygendeficient marine biofacies. Nature Geoscience, 327: 54-56.

Speed, R.C., 1982. Evolution of the sialic margin in the central Western United States. AAPG Memoir, 34: 457-468.

Theiling, B.P., Railsback, L.B., Holland, S.M., Crowe, D.E., 2007. Heterogeneity in geochemical expression of subaerial exposure in limestones, and its implications for sampling to detect exposure surfaces. Journal of Sedimentary Research, 77(2): 159-169.

Zhang, J.M., Li, G.X., Zhu, M.Y., Yang, A.H., 2001. Middle and Upper Cambrian slope deposits in the Waiergang section, Taoyuan County, northwestern Hunan Province. Acta Palaeontologica Sinica, 40: 173–200.

Zhu, M.-Y., Babcock, L.E., Peng, S.-C., 2006. Advances in Cambrian stratigraphy and paleontology: Integrating correlation techniques, paleobiology, taphonomy and paleoenvironmental reconstruction. Palaeoworld, 15(3-4): 217-222.

Zhu, M.-Y., Zhang, J.-M., Li, G.-X., Yang, A.-H., 2004. Evolution of C isotopes in the Cambrian of China: implications for Cambrian subdivision and trilobite mass extinctions. Geobios, 37(2): 287-301.

RECOMMENDATIONS

It is recommended that samples from other sections, which are distributed within the house range embayment be collected. The targeted sections should cover a longer interval, with the aim of tracing the lithostratigraphic markers, including storm layers, throughout the rest of the HRE. The goal would be to obtain facies distribution of these sediments and to differentiate between normal and storm deposits in an interval that is characterized by tectonic quiescence (Howley, 2010). This would demarcate the down-slope reach of the storm deposits, and hence, the limits of the reworked *P. atavus* specimens. It is concluded in this dissertation that the storm sediments are likely absent or have negligible thicknesses in the downslope sections of the northern ramp. Therefore, they represent better alternative successions to the current GSSP section. Unlike the three studied, syndepositional structures, erosional surfaces, and reworked sediments is expected to be at their minimal because their long distance from the northern HRE edge and small slope angle. In addition, they are expected to have high sediment accumulation rates of detrital dominated facies that assure event separation and have less lithological variations than the studied sections. Moreover, the DICE is expected to have more conspicuous signal and cover longer interval. These conditions are met on the southwest part of the embayment where the HRE has its maximum depth and width, and the fault had its maximum displacement. Steptoe Ranch in northern Egan Range (nEs), Muncy Creek in Northern Schell Creek Range (nSCm), Radio Tower in southern Egan Range (sE), and Patterson Pass in southern Schell Creek Range (sSC) are recommended successions for future studies (Figs. 2, 3 and 5; Rees, 1986). Intensive search for *P. atavus* and stable isotope analysis, $\delta^{13}C$ and $\delta^{18}O$, are recommended along with χ and

$CaCO_3$ to establish high-resolution regional chronostratigraphic correlation. This correlation can be extended globally to the Wangcun section in China because it has remarkable similarity with the studied sections. In conclusion, the depositional environment differences should account for χ, $\delta^{13}C$ and $CaCO_3$% variations among these sections.

APPENDICES

Tabulated below are the mass-specific magnetic susceptibility (χ), carbonate contents ($CaCO_3$%), and stable isotopes ($\delta^{13}C$ and $\delta^{18}O$) measurements and their splines for the Global Boundary Stratotype Section and Point (GSSP) of the base of the Drumian Stage that have been placed on Stratotype Ridge (39°30.705´ N, 112º59.489´ W) in the Drum Mountains, western Utah (Babcock et al., 2007), and two equivalent marine sedimentary successions. The equivalent sections are (1) the Marjum Pass section that was collected at the House Range (39°14'30.13" N, 113°22'30.61" W), western Utah, and (2) the Packrat section that was collected along the North Fork of the Big Wash (38°54’00.63926” N, 114°13’25.05219” W), Great Basin National Park, southern Snake Range, White Pine County, eastern Nevada. These data sets cover an interval that includes the Middle-Cambrian upper most part of unnamed Stage Five and the lowermost part of the Drumian Stage in the House Range Embayment (HRE). The height was adjusted to the closest formations boundary, the base of the Wheeler Formation at the GSSP and the Marjum Pass sections, and the base of the Lincoln Peak Formation at the Packrat section.

4.1. Mass-Specific Magnetic Susceptibility (χ) Measurements

4.1.1. The GSSP section, Drum Mountain, Western Utah

Serial	Sample #	Height (m)	χ (m3/Kg)	0.01 Spline
1	DM -25	55	2.11E-08	2.11E-08
2	DM -24	55.1	1.73E-08	2.07E-08
3	DM -23	55.2	2.73E-08	2.03E-08
4	DM -22	55.3	1.69E-08	1.94E-08
5	DM -21	55.4	1.82E-08	1.85E-08
6	DM -20	55.5	1.67E-08	1.79E-08
7	DM -19	55.6	1.73E-08	1.76E-08
8	DM -18	55.7	1.74E-08	1.78E-08
9	DM -17	55.8	1.89E-08	1.81E-08
10	DM -16	55.9	1.64E-08	1.86E-08
11	DM -15	56	2.39E-08	1.90E-08
12	DM -14	56.1	1.48E-08	1.90E-08
13	DM -13	56.2	2.49E-08	1.89E-08
14	DM -12	56.3	1.38E-08	1.87E-08
15	DM -11	56.4	1.67E-08	1.88E-08
16	DM -10	56.5	1.85E-08	1.93E-08
17	DM -09	56.6	2.63E-08	1.97E-08
18	DM -08	56.7	1.70E-08	1.94E-08
19	DM -07	56.8	1.94E-08	1.87E-08
20	DM -06	56.9	1.69E-08	1.80E-08
21	DM -05	57	1.49E-08	1.75E-08
22	DM -04	57.1	1.90E-08	1.70E-08
23	DM -03	57.2	1.77E-08	1.64E-08
24	DM -02	57.3	1.60E-08	1.56E-08
25	DM -01	57.4	1.28E-08	1.46E-08
26	DM 01	57.5	1.64E-08	1.42E-08
27	DM 02	57.55	1.46E-08	1.37E-08
28	DM 03	57.6	1.08E-08	1.34E-08
29	DM 04	57.65	1.31E-08	1.31E-08
30	DM 05	57.7	1.19E-08	1.30E-08
31	DM 06	57.75	1.38E-08	1.30E-08
32	DM 07	57.8	1.12E-08	1.32E-08
33	DM 08	57.85	1.48E-08	1.34E-08
34	DM 09	57.9	1.33E-08	1.36E-08
35	DM 10	57.95	1.26E-08	1.39E-08
36	DM 11	58	1.51E-08	1.41E-08
37	DM 12	58.05	1.79E-08	1.42E-08
38	DM 13	58.1	1.26E-08	1.43E-08
39	DM 14	58.15	1.54E-08	1.43E-08
40	DM 15	58.2	1.48E-08	1.42E-08

41	DM 16	58.25	1.16E-08	1.42E-08
42	DM 17	58.3	1.45E-08	1.41E-08
43	DM 18	58.35	1.49E-08	1.42E-08
44	DM 19	58.4	1.51E-08	1.42E-08
45	DM 20	58.45	1.15E-08	1.44E-08
46	DM 21	58.5	1.58E-08	1.46E-08
47	DM 22	58.55	1.44E-08	1.49E-08
48	DM 23	58.6	1.43E-08	1.53E-08
49	DM 24	58.65	1.66E-08	1.58E-08
50	DM 25	58.7	1.52E-08	1.63E-08
51	DM 26	58.75	1.75E-08	1.67E-08
52	DM 27	58.8	1.87E-08	1.72E-08
53	DM 28	58.85	1.95E-08	1.75E-08
54	DM 29	58.9	1.49E-08	1.78E-08
55	DM 30	58.95	1.83E-08	1.81E-08
56	DM 31	59	1.73E-08	1.84E-08
57	DM 32	59.05	1.75E-08	1.86E-08
58	DM 33	59.1	2.24E-08	1.87E-08
59	DM 34	59.15	1.68E-08	1.88E-08
60	DM 35	59.2	2.02E-08	1.88E-08
61	DM 36	59.25	2.23E-08	1.86E-08
62	DM 37	59.3	1.66E-08	1.84E-08
63	DM 38	59.35	1.74E-08	1.81E-08
64	DM 39	59.4	1.61E-08	1.80E-08
65	DM 40	59.45	1.71E-08	1.79E-08
66	DM 41	59.5	1.52E-08	1.80E-08
67	DM 42	59.55	2.07E-08	1.81E-08
68	DM 43	59.6	1.74E-08	1.83E-08
69	DM 44	59.65	1.66E-08	1.85E-08
70	DM 45	59.7	2.07E-08	1.86E-08
71	DM 46	59.75	2.03E-08	1.86E-08
72	DM 47	59.8	2.02E-08	1.83E-08
73	DM 48	59.85	2.11E-08	1.79E-08
74	DM 49	59.9	1.54E-08	1.73E-08
75	DM 50	59.95	1.44E-08	1.67E-08
76	DM 51	60	1.60E-08	1.62E-08
77	DM 52	60.05	1.43E-08	1.57E-08
78	DM 53	60.1	1.65E-08	1.53E-08
79	DM 54	60.15	1.16E-08	1.50E-08
80	DM 55	60.2	1.43E-08	1.48E-08
81	DM 56	60.25	1.56E-08	1.45E-08
82	DM 57	60.3	2.06E-08	1.43E-08
83	DM 58	60.35	1.40E-08	1.39E-08
84	DM 59	60.4	1.06E-08	1.36E-08

85	DM 60	60.45	1.29E-08	1.33E-08
86	DM 61	60.5	1.21E-08	1.31E-08
87	DM 62	60.55	1.23E-08	1.31E-08
88	DM 63	60.6	1.38E-08	1.32E-08
89	DM 64	60.65	1.11E-08	1.35E-08
90	DM 65	60.7	1.18E-08	1.38E-08
91	DM 66	60.75	1.79E-08	1.41E-08
92	DM 67	60.8	1.64E-08	1.44E-08
93	DM 68	60.85	1.49E-08	1.45E-08
94	DM 69	60.9	1.48E-08	1.45E-08
95	DM 70	60.95	1.37E-08	1.45E-08
96	DM 71	61	1.41E-08	1.45E-08
97	DM 72	61.05	1.38E-08	1.44E-08
98	DM 73	61.1	1.51E-08	1.44E-08
99	DM 74	61.15	1.20E-08	1.43E-08
100	DM 75	61.2	1.92E-08	1.43E-08
101	DM 76	61.25	1.50E-08	1.42E-08
102	DM 77	61.3	1.18E-08	1.42E-08
103	DM 78	61.35	1.38E-08	1.44E-08
104	DM 79	61.4	1.40E-08	1.47E-08
105	DM 80	61.45	1.36E-08	1.53E-08
106	DM 81	61.5	1.60E-08	1.60E-08
107	DM 82	61.55	1.48E-08	1.70E-08
108	DM 83	61.6	1.45E-08	1.81E-08
109	DM 84	61.65	2.08E-08	1.93E-08
110	DM 85	61.7	2.12E-08	2.03E-08
111	DM 86	61.75	2.29E-08	2.11E-08
112	DM 87	61.8	2.35E-08	2.15E-08
113	DM 88	61.85	2.47E-08	2.15E-08
114	DM 89	61.9	2.34E-08	2.10E-08
115	DM 90	61.95	2.46E-08	2.01E-08
116	DM 91	62	1.82E-08	1.89E-08
117	DM 92	62.05	1.39E-08	1.77E-08
118	DM 93	62.1	1.63E-08	1.65E-08
119	DM 94	62.15	1.17E-08	1.57E-08
120	DM 95	62.2	1.34E-08	1.52E-08
121	DM 96	62.25	7.10E-09	1.51E-08
122	DM 97	62.3	1.72E-08	1.53E-08
123	DM 98	62.35	1.99E-08	1.57E-08
124	DM 99	62.4	2.20E-08	1.61E-08
125	DM 100	62.45	2.11E-08	1.63E-08
126	DM 101	62.5	1.18E-08	1.65E-08
127	DM 102	62.55	1.51E-08	1.68E-08
128	DM 103	62.6	1.71E-08	1.73E-08

129	DM 104	62.65	1.42E-08	1.80E-08
130	DM 105	62.7	2.00E-08	1.90E-08
131	DM 106	62.75	2.20E-08	2.01E-08
132	DM 107	62.8	2.40E-08	2.14E-08
133	DM 108	62.85	2.04E-08	2.28E-08
134	DM 109	62.9	2.08E-08	2.44E-08
135	DM 110	62.95	2.66E-08	2.62E-08
136	DM 111	63	2.01E-08	2.80E-08
137	DM 112	63.05	2.02E-08	2.99E-08
138	DM 113	63.1	3.96E-08	3.15E-08
139	DM 114	63.15	4.69E-08	3.24E-08
140	DM 115	63.2	3.93E-08	3.23E-08
141	DM 116	63.25	3.30E-08	3.12E-08
142	DM 117	63.3	3.17E-08	2.93E-08
143	DM 118	63.35	2.58E-08	2.69E-08
144	DM 119	63.4	2.30E-08	2.43E-08
145	DM 120	63.45	1.23E-08	2.18E-08
146	DM 121	63.5	2.20E-08	1.97E-08
147	DM 122	63.55	1.28E-08	1.80E-08
148	DM 123	63.6	1.37E-08	1.69E-08
149	DM 124	63.65	1.41E-08	1.62E-08
150	DM 125	63.7	1.74E-08	1.58E-08
151	DM 126	63.75	1.33E-08	1.57E-08
152	DM 127	63.8	1.76E-08	1.56E-08
153	DM 128	63.85	2.50E-08	1.54E-08
154	DM 129	63.9	1.82E-08	1.50E-08
155	DM 130	63.95	1.16E-08	1.44E-08
156	DM 131	64	1.13E-08	1.39E-08
157	DM 132	64.05	1.24E-08	1.34E-08
158	DM 133	64.1	1.31E-08	1.32E-08
159	DM 134	64.15	1.24E-08	1.31E-08
160	DM 135	64.2	6.42E-09	1.32E-08
161	DM 136	64.25	1.63E-08	1.35E-08
162	DM 137	64.3	9.18E-09	1.38E-08
163	DM 138	64.35	1.31E-08	1.41E-08
164	DM 139	64.4	3.25E-08	1.41E-08
165	DM 140	64.45	1.86E-08	1.37E-08
166	DM 141	64.5	1.42E-08	1.29E-08
167	DM 142	64.55	9.31E-09	1.23E-08
168	DM 143	64.6	1.28E-08	1.20E-08
169	DM 144	64.65	1.18E-08	1.24E-08
170	DM 145	64.7	1.16E-08	1.39E-08
171	DM 146	64.75	1.02E-08	1.67E-08
172	DM 147	64.8	1.30E-08	2.11E-08

173	DM 148	64.85	1.57E-08	2.71E-08
174	DM 149	64.9	2.13E-08	3.46E-08
175	DM 150	64.95	2.43E-08	4.31E-08
176	DM 151	65	6.45E-08	5.20E-08
177	DM 152	65.05	8.01E-08	6.02E-08
178	DM 153	65.1	8.08E-08	6.67E-08
179	DM 154	65.15	6.58E-08	7.12E-08
180	DM 155	65.2	9.28E-08	7.35E-08
181	DM 156	65.25	7.70E-08	7.35E-08
182	DM 157	65.3	6.87E-08	7.16E-08
183	DM 158	65.35	8.14E-08	6.80E-08
184	DM 159	65.4	4.53E-08	6.31E-08
185	DM 160	65.45	7.23E-08	5.76E-08
186	DM 161	65.5	5.63E-08	5.16E-08
187	DM 162	65.55	2.35E-08	4.58E-08
188	DM 163	65.6	2.72E-08	4.08E-08
189	DM 164	65.65	4.41E-08	3.66E-08
190	DM 165	65.7	4.04E-08	3.33E-08
191	DM 166	65.75	2.17E-08	3.07E-08
192	DM 167	65.8	1.99E-08	2.90E-08
193	DM 168	65.85	2.30E-08	2.82E-08
194	DM 169	65.9	2.83E-08	2.79E-08
195	DM 170	65.95	4.60E-08	2.77E-08
196	DM 171	66	2.94E-08	2.73E-08
197	DM 172	66.05	2.12E-08	2.68E-08
198	DM 173	66.1	3.20E-08	2.61E-08
199	DM 174	66.15	2.01E-08	2.53E-08
200	DM 175	66.2	2.01E-08	2.44E-08
201	DM 176	66.25	3.66E-08	2.34E-08
202	DM 177	66.3	2.28E-08	2.23E-08
203	DM 178	66.35	1.84E-08	2.12E-08
204	DM 179	66.4	1.43E-08	2.03E-08
205	DM 180	66.45	1.64E-08	1.97E-08
206	DM 181	66.5	1.99E-08	1.96E-08
207	DM 182	66.55	2.09E-08	1.97E-08
208	DM 183	66.6	1.86E-08	2.00E-08
209	DM 184	66.65	2.07E-08	2.05E-08
210	DM 185	66.7	1.93E-08	2.11E-08
211	DM 186	66.75	2.51E-08	2.17E-08
212	DM 187	66.8	2.49E-08	2.22E-08
213	DM 188	66.85	2.70E-08	2.26E-08
214	DM 189	66.9	2.74E-08	2.28E-08
215	DM 190	66.95	2.88E-08	2.32E-08
216	DM 191	67	1.94E-08	2.38E-08

217	DM 192	67.05	1.94E-08	2.51E-08
218	DM 193	67.1	2.13E-08	2.73E-08
219	DM 194	67.15	1.44E-08	3.06E-08
220	DM 195	67.2	1.90E-08	3.50E-08
221	DM 196	67.25	5.59E-08	4.00E-08
222	DM 197	67.3	5.38E-08	4.50E-08
223	DM 198	67.35	5.10E-08	4.94E-08
224	DM 199	67.4	5.98E-08	5.32E-08
225	DM 200	67.45	5.73E-08	5.61E-08
226	DM 201	67.5	5.94E-08	5.81E-08
227	DM 202	67.55	6.44E-08	5.93E-08
228	DM 203	67.6	4.97E-08	5.98E-08
229	DM 204	67.65	6.26E-08	5.97E-08
230	DM 205	67.7	6.06E-08	5.91E-08
231	DM 206	67.75	6.51E-08	5.78E-08
232	DM 207	67.8	6.21E-08	5.61E-08
233	DM 208	67.85	5.42E-08	5.42E-08
234	DM 209	67.9	4.72E-08	5.24E-08
235	DM 210	67.95	4.84E-08	5.11E-08
236	DM 211	68	4.21E-08	5.06E-08
237	DM 212	68.05	4.48E-08	5.10E-08
238	DM 213	68.1	4.64E-08	5.23E-08
239	DM 214	68.15	5.15E-08	5.44E-08
240	DM 215	68.2	6.39E-08	5.70E-08
241	DM 216	68.25	6.38E-08	5.96E-08
242	DM 217	68.3	6.39E-08	6.22E-08
243	DM 218	68.35	5.97E-08	6.45E-08
244	DM 219	68.4	6.98E-08	6.64E-08
245	DM 220	68.45	7.61E-08	6.79E-08
246	DM 221	68.5	6.39E-08	6.87E-08
247	DM 222	68.55	7.01E-08	6.90E-08
248	DM 223	68.6	7.67E-08	6.88E-08
249	DM 224	68.65	7.06E-08	6.81E-08
250	DM 225	68.7	7.08E-08	6.70E-08
251	DM 226	68.75	7.17E-08	6.59E-08
252	DM 227	68.8	5.78E-08	6.51E-08
253	DM 228	68.85	4.92E-08	6.50E-08
254	DM 229	68.9	4.97E-08	6.61E-08
255	DM 230	68.95	7.89E-08	6.80E-08
256	DM 231	69	6.98E-08	7.06E-08
257	DM 232	69.05	7.57E-08	7.36E-08
258	DM 233	69.1	7.12E-08	7.67E-08
259	DM 234	69.15	8.07E-08	7.97E-08
260	DM 235	69.2	7.55E-08	8.23E-08

261	DM 236	69.25	8.39E-08	8.43E-08
262	DM 237	69.3	1.06E-07	8.51E-08
263	DM 238	69.35	1.15E-07	8.45E-08
264	DM 239	69.4	1.10E-07	8.24E-08
265	DM 240	69.45	5.00E-08	7.98E-08
266	DM 241	69.5	4.99E-08	7.78E-08
267	DM 242	69.55	5.31E-08	7.72E-08
268	DM 243	69.6	7.03E-08	7.81E-08
269	DM 244	69.65	1.10E-07	8.01E-08
270	DM 245	69.7	7.78E-08	8.24E-08
271	DM 246	69.75	8.73E-08	8.52E-08
272	DM 247	69.8	7.59E-08	8.81E-08
273	DM 248	69.85	8.26E-08	9.12E-08
274	DM 249	69.9	1.13E-07	9.41E-08
275	DM 250	69.95	1.06E-07	9.64E-08
276	DM 251	70	9.08E-08	9.78E-08
277	DM 252	70.05	1.12E-07	9.85E-08
278	DM 253	70.1	1.03E-07	9.85E-08
279	DM 254	70.15	9.86E-08	9.82E-08
280	DM 255	70.2	8.38E-08	9.78E-08
281	DM 256	70.25	9.54E-08	9.78E-08
282	DM 257	70.3	1.02E-07	9.83E-08
283	DM 258	70.35	8.54E-08	9.93E-08
284	DM 259	70.4	9.87E-08	1.01E-07
285	DM 260	70.45	9.38E-08	1.03E-07
286	DM 261	70.5	1.13E-07	1.05E-07
287	DM 262	70.55	1.31E-07	1.07E-07
288	DM 263	70.6	9.37E-08	1.08E-07
289	DM 264	70.65	1.10E-07	1.08E-07
290	DM 265	70.7	1.22E-07	1.08E-07
291	DM 266	70.75	9.33E-08	1.08E-07
292	DM 267	70.8	8.32E-08	1.08E-07
293	DM 268	70.85	1.31E-07	1.07E-07
294	DM 269	70.9	1.23E-07	1.05E-07
295	DM 270	70.95	7.70E-08	1.03E-07
296	DM 271	71	1.10E-07	1.00E-07
297	DM 272	71.05	9.01E-08	9.67E-08
298	DM 273	71.1	1.42E-07	9.24E-08
299	DM 274	71.15	8.67E-08	8.73E-08
300	DM 275	71.2	3.73E-08	8.24E-08
301	DM 276	71.25	8.18E-08	7.85E-08
302	DM 277	71.3	4.73E-08	7.57E-08
303	DM 278	71.35	9.12E-08	7.39E-08
304	DM 279	71.4	6.32E-08	7.25E-08

305	DM 280	71.45	8.31E-08	7.13E-08
306	DM 281	71.5	1.01E-07	6.98E-08
307	DM 282	71.55	3.31E-08	6.77E-08
308	DM 283	71.6	7.14E-08	6.56E-08
309	DM 284	71.65	7.63E-08	6.32E-08
310	DM 285	71.7	7.30E-08	6.03E-08
311	DM 286	71.75	7.28E-08	5.72E-08
312	DM 287	71.8	3.51E-08	5.45E-08
313	DM 288	71.85	3.13E-08	5.27E-08
314	DM 289	71.9	4.25E-08	5.24E-08
315	DM 290	71.95	5.67E-08	5.33E-08
316	DM 291	72	3.20E-08	5.53E-08
317	DM 292	72.05	5.78E-08	5.79E-08
318	DM 293	72.1	7.80E-08	6.03E-08
319	DM 294	72.15	8.76E-08	6.17E-08
320	DM 295	72.2	5.56E-08	6.17E-08
321	DM 296	72.25	5.03E-08	6.04E-08
322	DM 297	72.3	8.14E-08	5.77E-08
323	DM 298	72.35	7.43E-08	5.38E-08
324	DM 299	72.4	2.37E-08	4.88E-08
325	DM 300	72.45	5.11E-08	4.36E-08
326	DM 301	72.5	2.35E-08	3.86E-08
327	DM 302	72.55	3.57E-08	3.41E-08
328	DM 303	72.6	2.27E-08	3.04E-08
329	DM 304	72.65	2.28E-08	2.74E-08
330	DM 305	72.7	3.35E-08	2.52E-08
331	DM 306	72.75	1.96E-08	2.36E-08
332	DM +01	72.85	2.36E-08	2.21E-08
333	DM +02	72.95	1.90E-08	2.27E-08
334	DM +03	73.05	2.31E-08	2.49E-08
335	DM +04	73.15	3.40E-08	2.77E-08
336	DM +05	73.25	3.57E-08	3.02E-08
337	DM +06	73.35	3.24E-08	3.22E-08
338	DM +07	73.45	2.55E-08	3.46E-08
339	DM +08	73.55	3.43E-08	3.81E-08
340	DM +09	73.65	5.79E-08	4.20E-08
341	DM +10	73.75	3.72E-08	4.56E-08
342	DM +11	73.85	5.01E-08	4.96E-08
343	DM +12	73.95	4.38E-08	5.44E-08
344	DM +13	74.05	6.66E-08	5.95E-08
345	DM +14	74.15	6.67E-08	6.35E-08
346	DM +15	74.25	6.61E-08	6.56E-08
347	DM +16	74.35	8.34E-08	6.59E-08
348	DM +17	74.45	5.18E-08	6.48E-08

349	DM +18	74.55	4.80E-08	6.50E-08
350	DM +19	74.65	7.75E-08	6.73E-08
351	DM +20	74.75	6.98E-08	7.04E-08
352	DM +21	74.85	6.46E-08	7.34E-08
353	DM +22	74.95	8.80E-08	7.57E-08
354	DM +23	75.05	7.66E-08	7.56E-08
355	DM +24	75.15	8.17E-08	7.31E-08
356	DM +25	75.25	6.81E-08	6.87E-08
357	DM +26	75.35	6.29E-08	6.43E-08
358	DM +27	75.45	4.95E-08	6.19E-08
359	DM +28	75.55	5.58E-08	6.28E-08
360	DM +29	75.65	6.44E-08	6.66E-08
361	DM +30	75.75	6.65E-08	7.11E-08
362	DM +31	75.85	8.74E-08	7.38E-08
363	DM +32	75.95	8.89E-08	7.18E-08
364	DM +33	76.05	8.19E-08	6.44E-08
365	DM +34	76.15	2.45E-08	5.43E-08
366	DM +35	76.25	3.92E-08	4.59E-08
367	DM +36	76.35	4.94E-08	4.04E-08
368	DM +37	76.45	2.76E-08	3.70E-08
369	DM +38	76.55	3.60E-08	3.58E-08
370	DM +39	76.65	3.48E-08	3.58E-08
371	DM +40	76.75	5.28E-08	3.58E-08
372	DM +41	76.85	2.70E-08	3.50E-08
373	DM +42	76.95	3.57E-08	3.45E-08
374	DM +43	77.05	2.30E-08	3.50E-08
375	DM +44	77.15	2.26E-08	3.67E-08
376	DM +45	77.25	8.38E-08	3.77E-08
377	DM +46	77.35	2.89E-08	3.55E-08
378	DM +47	77.45	1.77E-08	3.29E-08
379	DM +48	77.55	2.55E-08	3.29E-08
380	DM +49	77.65	2.18E-08	3.60E-08
381	DM +50	77.75	6.39E-08	4.07E-08
382	DM +51	77.85	2.72E-08	4.43E-08
383	DM +52	77.95	8.65E-08	4.61E-08
384	DM +53	78.05	2.40E-08	4.50E-08
385	DM +54	78.15	3.30E-08	4.43E-08
386	DM +55	78.25	3.52E-08	4.53E-08
387	DM +56	78.35	5.16E-08	4.69E-08
388	DM +57	78.45	8.16E-08	4.63E-08
389	DM +58	78.55	2.37E-08	4.22E-08
390	DM +59	78.65	3.31E-08	3.76E-08
391	DM +60	78.75	3.31E-08	3.39E-08
392	DM +61	78.85	2.63E-08	3.15E-08

393	DM +62	78.95	3.72E-08	3.03E-08
394	DM +63	79.05	2.98E-08	2.96E-08
395	DM +64	79.15	2.92E-08	2.94E-08
396	DM +65	79.25	2.68E-08	3.02E-08
397	DM +66	79.35	1.82E-08	3.22E-08
398	DM +67	79.45	3.45E-08	3.46E-08
399	DM +68	79.55	7.14E-08	3.48E-08
400	DM +69	79.65	2.61E-08	3.09E-08
401	DM +70	79.75	1.39E-08	2.56E-08
402	DM +71	79.85	1.31E-08	2.18E-08
403	DM +72	79.95	2.32E-08	2.06E-08
404	DM +73	80.05	1.40E-08	2.13E-08
405	DM +74	80.15	3.39E-08	2.32E-08
406	DM +75	80.25	1.84E-08	2.51E-08
407	DM +76	80.35	3.82E-08	2.67E-08
408	DM +77	80.45	1.70E-08	2.77E-08
409	DM +78	80.55	3.22E-08	2.84E-08
410	DM +79	80.65	3.08E-08	2.86E-08
411	DM +80	80.75	2.68E-08	2.81E-08
412	DM +81	80.85	2.86E-08	2.72E-08
413	DM +82	80.95	2.58E-08	2.58E-08
414	DM +83	81.05	2.25E-08	2.44E-08
415	DM +84	81.15	2.34E-08	2.33E-08
416	DM +85	81.25	2.24E-08	2.24E-08
417	DM +86	81.35	2.74E-08	2.17E-08
418	DM +87	81.45	1.33E-08	2.15E-08
419	DM +88	81.55	2.39E-08	2.22E-08
420	DM +89	81.65	1.94E-08	2.39E-08
421	DM +90	81.75	2.44E-08	2.59E-08
422	DM +91	81.85	3.50E-08	2.74E-08
423	DM +92	81.95	3.34E-08	2.73E-08
424	DM +93	82.05	2.27E-08	2.57E-08
425	DM +94	82.15	1.77E-08	2.35E-08
426	DM +95	82.25	2.18E-08	2.14E-08
427	DM +96	82.35	2.16E-08	1.93E-08
428	DM +97	82.45	1.78E-08	1.69E-08
429	DM +98	82.55	2.01E-08	1.42E-08
430	DM +99	82.65	8.37E-09	1.18E-08
431	DM +100	82.75	9.37E-09	1.08E-08
432	DM +101	82.85	8.20E-09	1.20E-08
433	DM +102	82.95	6.65E-09	1.59E-08
434	DM +103	83.05	1.42E-08	2.21E-08
435	DM +104	83.15	4.34E-08	2.84E-08
436	DM +105	83.25	4.05E-08	3.20E-08

437	DM +106	83.35	2.92E-08	3.19E-08
438	DM +107	83.45	4.21E-08	2.87E-08
439	DM +108	83.55	1.29E-08	2.36E-08
440	DM +109	83.65	1.43E-08	1.87E-08
441	DM +110	83.75	1.13E-08	1.55E-08
442	DM +111	83.85	1.48E-08	1.39E-08
443	DM +112	83.95	1.47E-08	1.35E-08
444	DM +113	84.05	1.07E-08	1.38E-08
445	DM +114	84.15	2.31E-08	1.43E-08
446	DM +115	84.25	8.61E-09	1.45E-08
447	DM +116	84.35	1.68E-08	1.48E-08
448	DM +117	84.45	1.42E-08	1.51E-08
449	DM +118	84.55	1.64E-08	1.56E-08
450	DM +119	84.65	1.44E-08	1.61E-08
451	DM +120	84.75	1.72E-08	1.66E-08
452	DM +121	84.85	1.79E-08	1.71E-08
453	DM +122	84.95	1.79E-08	1.73E-08
454	DM +123	85.05	1.62E-08	1.74E-08
455	DM +124	85.15	1.96E-08	1.74E-08
456	DM +125	85.25	1.66E-08	1.73E-08
457	DM +126	85.35	1.53E-08	1.74E-08
458	DM +127	85.45	1.68E-08	1.78E-08
459	DM +128	85.55	1.87E-08	1.85E-08
460	DM +129	85.65	2.16E-08	1.89E-08
461	DM +130	85.75	1.91E-08	1.89E-08
462	DM +131	85.85	1.91E-08	1.86E-08
463	DM +132	85.95	1.61E-08	1.81E-08
464	DM +133	86.05	1.81E-08	1.78E-08
465	DM +134	86.15	1.86E-08	1.74E-08
466	DM +135	86.25	1.55E-08	1.72E-08
467	DM +136	86.35	1.66E-08	1.71E-08
468	DM +137	86.45	1.88E-08	1.70E-08
469	DM +138	86.55	1.73E-08	1.69E-08
470	DM +139	86.65	1.48E-08	1.67E-08
471	DM +140	86.75	1.74E-08	1.66E-08

4.1.2. Marjum Pass Section, House Range, Western Utah

Serial	Sample #	Height (m)	χ (m3/Kg)	0.01 Spline
1	HR -124	0	6.50E-09	6.32E-09
2	HR -123	0.62	2.46E-08	2.55E-08
3	HR -122	1.24	5.38E-08	5.23E-08
4	HR -121	1.86	2.69E-08	2.81E-08
5	HR -120	2.48	2.18E-08	2.08E-08
6	HR -119	3.1	1.74E-08	1.88E-08
7	HR -118	3.72	5.06E-08	4.89E-08
8	HR -117	4.34	3.44E-08	3.57E-08
9	HR -116	4.96	4.47E-08	4.37E-08
10	HR -115	5.58	5.65E-08	5.80E-08
11	HR -114	6.2	9.64E-08	9.44E-08
12	HR -113	6.82	6.83E-08	6.98E-08
13	HR -112	7.44	7.15E-08	7.13E-08
14	HR -111	8.06	7.06E-08	7.00E-08
15	HR -110	8.68	4.48E-08	4.56E-08
16	HR -109	9.3	4.64E-08	4.60E-08
17	HR -108	9.92	4.69E-08	4.67E-08
18	HR -107	10.54	4.80E-08	4.87E-08
19	HR -106	11.16	7.25E-08	7.18E-08
20	HR -105	11.78	7.04E-08	7.02E-08
21	HR -104	12.4	7.19E-08	7.41E-08
22	HR -103	13.02	1.11E-07	8.93E-08
23	HR -102	13.6	7.58E-08	8.25E-08
24	HR -101	13.7	6.24E-08	7.66E-08
25	HR -100	13.8	5.43E-08	7.40E-08
26	HR -099	13.9	9.77E-08	7.42E-08
27	HR -098	14	7.30E-08	7.44E-08
28	HR -097	14.1	7.41E-08	7.42E-08
29	HR -096	14.2	7.73E-08	7.40E-08
30	HR -095	14.3	7.09E-08	7.40E-08
31	HR -094	14.4	7.32E-08	7.49E-08
32	HR -093	14.5	7.51E-08	7.69E-08
33	HR -092	14.6	7.18E-08	8.00E-08
34	HR -091	14.7	8.76E-08	8.35E-08
35	HR -090	14.8	1.03E-07	8.56E-08
36	HR -089	14.9	8.13E-08	8.56E-08
37	HR -088	15	7.59E-08	8.48E-08
38	HR -087	15.1	9.18E-08	8.43E-08
39	HR -086	15.2	7.06E-08	8.43E-08
40	HR -085	15.3	9.86E-08	8.50E-08
41	HR -084	15.4	7.82E-08	8.57E-08
42	HR -083	15.5	9.43E-08	8.65E-08

43	HR -082	15.6	7.20E-08	8.75E-08
44	HR -081	15.7	1.04E-07	8.90E-08
45	HR -080	15.8	8.45E-08	8.99E-08
46	HR -079	15.9	8.92E-08	9.03E-08
47	HR -078	16	9.78E-08	9.03E-08
48	HR -077	16.1	8.75E-08	8.96E-08
49	HR -076	16.2	8.15E-08	8.91E-08
50	HR -075	16.3	9.16E-08	8.90E-08
51	HR -074	16.4	9.39E-08	8.89E-08
52	HR -073	16.5	8.81E-08	8.85E-08
53	HR -072	16.6	8.86E-08	8.82E-08
54	HR -071	16.7	8.04E-08	8.86E-08
55	HR -070	16.8	9.01E-08	9.01E-08
56	HR -069	16.9	9.52E-08	9.18E-08
57	HR -068	17	9.92E-08	9.29E-08
58	HR -067	17.1	9.06E-08	9.31E-08
59	HR -066	17.2	9.32E-08	9.31E-08
60	HR -065	17.3	8.89E-08	9.33E-08
61	HR -064	17.4	9.23E-08	9.40E-08
62	HR -063	17.5	8.84E-08	9.48E-08
63	HR -062	17.6	1.22E-07	9.48E-08
64	HR -061	17.7	8.38E-08	9.28E-08
65	HR -060	17.8	7.90E-08	9.11E-08
66	HR -059	17.9	9.23E-08	9.10E-08
67	HR -058	18	9.13E-08	9.19E-08
68	HR -057	18.1	9.66E-08	9.31E-08
69	HR -056	18.2	9.11E-08	9.38E-08
70	HR -055	18.3	9.61E-08	9.39E-08
71	HR -054	18.4	9.50E-08	9.28E-08
72	HR -053	18.5	1.01E-07	9.02E-08
73	HR -052	18.6	7.53E-08	8.66E-08
74	HR -051	18.7	8.18E-08	8.38E-08
75	HR -050	18.8	8.43E-08	8.22E-08
76	HR -049	18.9	7.83E-08	8.16E-08
77	HR -048	19	7.64E-08	8.22E-08
78	HR -047	19.1	9.15E-08	8.33E-08
79	HR -046	19.2	8.84E-08	8.37E-08
80	HR -045	19.3	8.04E-08	8.35E-08
81	HR -044	19.4	9.32E-08	8.31E-08
82	HR -043	19.5	5.51E-08	8.35E-08
83	HR -042	19.6	9.22E-08	8.57E-08
84	HR -041	19.7	9.70E-08	8.75E-08
85	HR -040	19.8	9.94E-08	8.68E-08
86	HR -039	19.9	7.06E-08	8.38E-08

87	HR -038	20	9.45E-08	7.99E-08
88	HR -037	20.1	6.25E-08	7.57E-08
89	HR -036	20.2	6.58E-08	7.31E-08
90	HR -035	20.3	6.90E-08	7.21E-08
91	HR -034	20.4	8.16E-08	7.15E-08
92	HR -033	20.5	6.76E-08	6.96E-08
93	HR -032	20.6	8.26E-08	6.60E-08
94	HR -031	20.7	5.12E-08	6.09E-08
95	HR -030	20.8	5.15E-08	5.63E-08
96	HR -029	20.9	4.92E-08	5.33E-08
97	HR -028	21	5.10E-08	5.20E-08
98	HR -027	21.1	5.52E-08	5.16E-08
99	HR -026	21.2	5.03E-08	5.13E-08
100	HR -025	21.3	5.26E-08	5.06E-08
101	HR -024	21.4	5.13E-08	4.91E-08
102	HR -023	21.5	4.88E-08	4.68E-08
103	HR -022	21.6	4.45E-08	4.40E-08
104	HR -021	21.7	3.84E-08	4.14E-08
105	HR -020	21.8	3.53E-08	3.98E-08
106	HR -019	21.9	3.58E-08	3.94E-08
107	HR -018	22	4.51E-08	3.95E-08
108	HR -017	22.1	4.37E-08	3.91E-08
109	HR -016	22.2	3.56E-08	3.79E-08
110	HR -015	22.3	3.57E-08	3.64E-08
111	HR -014	22.4	3.38E-08	3.49E-08
112	HR -013	22.5	3.66E-08	3.34E-08
113	HR -012	22.6	2.56E-08	3.21E-08
114	HR -011	22.7	3.73E-08	3.09E-08
115	HR -010	22.8	2.84E-08	2.97E-08
116	HR -009	22.9	2.81E-08	2.86E-08
117	HR -008	23	2.84E-08	2.78E-08
118	HR -007	23.1	2.44E-08	2.75E-08
119	HR -006	23.2	3.27E-08	2.78E-08
120	HR -005	23.3	2.59E-08	2.86E-08
121	HR -004	23.4	3.06E-08	3.03E-08
122	HR -003	23.5	3.61E-08	3.29E-08
123	HR -002	23.6	2.81E-08	3.68E-08
124	HR -001	23.7	3.03E-08	4.23E-08
125	HR 001	23.8	6.46E-08	4.83E-08
126	HR 002	23.9	4.69E-08	5.23E-08
127	HR 003	24	6.31E-08	5.34E-08
128	HR 004	24.1	5.96E-08	5.09E-08
129	HR 005	24.2	5.26E-08	4.56E-08
130	HR 006	24.3	2.23E-08	3.98E-08

131	HR 007	24.4	3.63E-08	3.65E-08
132	HR 008	24.5	1.96E-08	3.68E-08
133	HR 009	24.6	3.53E-08	4.04E-08
134	HR 010	24.7	5.13E-08	4.46E-08
135	HR 011	24.8	7.45E-08	4.57E-08
136	HR 012	24.9	4.59E-08	4.17E-08
137	HR 013	25	2.91E-08	3.47E-08
138	HR 014	25.1	2.10E-08	2.82E-08
139	HR 015	25.2	1.58E-08	2.49E-08
140	HR 016	25.3	1.98E-08	2.58E-08
141	HR 017	25.4	1.72E-08	3.06E-08
142	HR 018	25.5	7.10E-08	3.72E-08
143	HR 019	25.6	2.71E-08	4.27E-08
144	HR 020	25.7	3.99E-08	4.78E-08
145	HR 021	25.8	6.38E-08	5.18E-08
146	HR 022	25.9	5.79E-08	5.30E-08
147	HR 023	26	4.66E-08	5.13E-08
148	HR 024	26.1	6.59E-08	4.72E-08
149	HR 025	26.2	2.38E-08	4.15E-08
150	HR 026	26.3	3.01E-08	3.68E-08
151	HR 027	26.4	3.34E-08	3.37E-08
152	HR 028	26.5	4.73E-08	3.14E-08
153	HR 029	26.6	2.14E-08	2.93E-08
154	HR 030	26.7	2.72E-08	2.85E-08
155	HR 031	26.8	3.61E-08	2.97E-08
156	HR 032	26.9	2.00E-08	3.35E-08
157	HR 033	27	2.10E-08	4.05E-08
158	HR 034	27.1	4.65E-08	4.95E-08
159	HR 035	27.2	8.57E-08	5.58E-08
160	HR 036	27.3	9.15E-08	5.49E-08
161	HR 037	27.4	3.22E-08	4.72E-08
162	HR 038	27.5	1.80E-08	3.86E-08
163	HR 039	27.6	2.47E-08	3.37E-08
164	HR 040	27.7	3.10E-08	3.32E-08
165	HR 041	27.8	3.41E-08	3.60E-08
166	HR 042	27.9	5.05E-08	4.04E-08
167	HR 043	28	4.08E-08	4.46E-08
168	HR 044	28.1	6.60E-08	4.82E-08
169	HR 045	28.2	3.84E-08	5.09E-08
170	HR 046	28.3	4.80E-08	5.44E-08
171	HR 047	28.4	5.94E-08	5.91E-08
172	HR 048	28.5	7.09E-08	6.42E-08
173	HR 049	28.6	5.51E-08	6.87E-08
174	HR 050	28.7	8.42E-08	7.23E-08

175	HR 051	28.8	7.97E-08	7.35E-08
176	HR 052	28.9	7.77E-08	7.20E-08
177	HR 053	29	7.26E-08	6.89E-08
178	HR 045	29.1	2.85E-08	6.66E-08
179	HR 055	29.2	8.02E-08	6.66E-08
180	HR 056	29.3	7.74E-08	6.62E-08
181	HR 057	29.4	6.88E-08	6.35E-08
182	HR 058	29.5	5.10E-08	5.86E-08
183	HR 059	29.6	6.66E-08	5.25E-08
184	HR 060	29.7	3.75E-08	4.60E-08
185	HR 061	29.8	3.57E-08	4.10E-08
186	HR 062	29.9	3.20E-08	3.88E-08
187	HR 063	30	4.13E-08	3.93E-08
188	HR 064	30.1	4.07E-08	4.14E-08
189	HR 065	30.2	4.53E-08	4.42E-08
190	HR 066	30.3	5.28E-08	4.67E-08
191	HR 067	30.4	4.89E-08	4.81E-08
192	HR 068	30.5	5.09E-08	4.86E-08
193	HR 069	30.6	4.10E-08	4.89E-08
194	HR 070	30.7	5.31E-08	4.95E-08
195	HR 071	30.8	4.96E-08	5.02E-08
196	HR 072	30.9	5.20E-08	5.10E-08
197	HR 073	31	5.10E-08	5.20E-08
198	HR 074	31.1	5.02E-08	5.31E-08
199	HR 075	31.2	5.62E-08	5.43E-08
200	HR 076	31.3	6.00E-08	5.52E-08
201	HR 077	31.4	5.11E-08	5.56E-08
202	HR 078	31.5	5.71E-08	5.60E-08
203	HR 079	31.6	5.59E-08	5.64E-08
204	HR 080	31.7	5.62E-08	5.68E-08
205	HR 081	31.8	5.97E-08	5.71E-08
206	HR 082	31.9	5.73E-08	5.72E-08
207	HR 083	32	5.77E-08	5.76E-08
208	HR 084	32.1	5.78E-08	5.84E-08
209	HR 085	32.2	5.28E-08	6.01E-08
210	HR 086	32.3	6.58E-08	6.27E-08
211	HR 087	32.4	6.62E-08	6.55E-08
212	HR 088	32.5	7.20E-08	6.78E-08
213	HR 089	32.6	6.48E-08	6.93E-08
214	HR 090	32.7	7.07E-08	7.00E-08
215	HR 091	32.8	7.53E-08	6.97E-08
216	HR 092	32.9	7.67E-08	6.82E-08
217	HR 093	33	5.32E-08	6.63E-08
218	HR 094	33.1	6.19E-08	6.58E-08

219	HR 095	33.2	7.03E-08	6.68E-08
220	HR 096	33.3	6.57E-08	6.86E-08
221	HR 097	33.4	7.22E-08	7.06E-08
222	HR 098	33.5	7.43E-08	7.23E-08
223	HR 099	33.6	7.63E-08	7.30E-08
224	HR 100	33.7	7.34E-08	7.27E-08
225	HR 101	33.8	7.51E-08	7.19E-08
226	HR 102	33.9	6.46E-08	7.13E-08
227	HR 103	34	6.48E-08	7.20E-08
228	HR 104	34.1	7.93E-08	7.39E-08
229	HR 105	34.2	7.18E-08	7.59E-08
230	HR 106	34.3	8.52E-08	7.74E-08
231	HR 107	34.4	7.85E-08	7.76E-08
232	HR 108	34.5	7.91E-08	7.66E-08
233	HR 109	34.6	7.21E-08	7.49E-08
234	HR 110	34.7	6.62E-08	7.34E-08
235	HR 111	34.8	7.83E-08	7.24E-08
236	HR 112	34.9	7.22E-08	7.13E-08
237	HR 113	35	6.60E-08	7.02E-08
238	HR 114	35.1	7.30E-08	6.94E-08
239	HR 115	35.2	6.85E-08	6.85E-08
240	HR 116	35.3	6.97E-08	6.77E-08
241	HR 117	35.4	6.72E-08	6.75E-08
242	HR 118	35.5	5.84E-08	6.83E-08
243	HR 119	35.6	7.54E-08	7.05E-08
244	HR 120	35.7	6.90E-08	7.31E-08
245	HR 121	35.8	8.17E-08	7.55E-08
246	HR 122	35.9	7.32E-08	7.69E-08
247	HR 123	36	8.68E-08	7.70E-08
248	HR 124	36.1	7.53E-08	7.54E-08
249	HR 125	36.2	6.88E-08	7.32E-08
250	HR 126	36.3	7.02E-08	7.12E-08
251	HR 127	36.4	6.49E-08	7.01E-08
252	HR 128	36.5	7.16E-08	6.97E-08
253	HR 129	36.6	7.73E-08	6.94E-08
254	HR 130	36.7	6.55E-08	6.88E-08
255	HR 131	36.8	6.23E-08	6.87E-08
256	HR 132	36.9	7.56E-08	6.94E-08
257	HR 133	37	6.77E-08	7.04E-08
258	HR 134	37.1	6.84E-08	7.17E-08
259	HR 135	37.2	7.62E-08	7.33E-08
260	HR 136	37.3	7.69E-08	7.45E-08
261	HR 137	37.4	7.76E-08	7.49E-08
262	HR 138	37.5	6.99E-08	7.48E-08

263	HR 139	37.6	7.39E-08	7.48E-08
264	HR 140	37.7	7.83E-08	7.47E-08
265	HR 141	37.8	7.06E-08	7.43E-08
266	HR 142	37.9	8.02E-08	7.37E-08
267	HR 143	38	6.95E-08	7.28E-08
268	HR 144	38.1	7.06E-08	7.21E-08
269	HR 145	38.2	7.25E-08	7.19E-08
270	HR 146	38.3	6.55E-08	7.22E-08
271	HR 147	38.4	8.30E-08	7.27E-08
272	HR 148	38.5	7.15E-08	7.27E-08
273	HR 149	38.6	6.94E-08	7.25E-08
274	HR 150	38.7	6.87E-08	7.26E-08
275	HR 151	38.8	7.88E-08	7.28E-08
276	HR 152	38.9	7.33E-08	7.25E-08
277	HR 153	39	7.10E-08	7.18E-08
278	HR 154	39.1	7.17E-08	7.10E-08
279	HR 155	39.2	6.84E-08	7.03E-08
280	HR 156	39.3	6.76E-08	7.03E-08
281	HR 157	39.4	6.37E-08	7.06E-08
282	HR 158	39.5	9.47E-08	7.09E-08
283	HR 159	39.6	5.94E-08	7.00E-08
284	HR 160	39.7	6.04E-08	6.97E-08
285	HR 161	39.8	7.12E-08	7.08E-08
286	HR 162	39.9	7.52E-08	7.24E-08
287	HR 163	40	7.51E-08	7.37E-08
288	HR 164	40.1	7.65E-08	7.39E-08
289	HR 165	40.2	7.92E-08	7.29E-08
290	HR 166	40.3	6.62E-08	7.12E-08
291	HR 167	40.4	6.35E-08	6.99E-08
292	HR 168	40.5	7.15E-08	6.95E-08
293	HR 169	40.6	6.54E-08	6.96E-08
294	HR 170	40.7	7.63E-08	6.97E-08
295	HR 171	40.8	8.06E-08	6.89E-08
296	HR 172	40.9	4.94E-08	6.75E-08
297	HR 173	41	7.81E-08	6.70E-08
298	HR 174	41.1	5.97E-08	6.73E-08
299	HR 175	41.2	5.84E-08	6.87E-08
300	HR 176	41.3	8.55E-08	7.08E-08
301	HR 177	41.4	7.40E-08	7.18E-08
302	HR 178	41.5	7.28E-08	7.17E-08
303	HR 179	41.6	6.96E-08	7.15E-08
304	HR 180	41.7	6.68E-08	7.20E-08
305	HR 181	41.8	6.83E-08	7.38E-08
306	HR 182	41.9	8.06E-08	7.67E-08

307	HR 183	42	8.25E-08	7.95E-08
308	HR 184	42.1	7.62E-08	8.16E-08
309	HR 185	42.2	8.89E-08	8.25E-08
310	HR 186	42.3	8.76E-08	8.16E-08
311	HR 187	42.4	8.12E-08	7.90E-08
312	HR 188	42.5	7.20E-08	7.60E-08
313	HR 189	42.6	6.32E-08	7.40E-08
314	HR 190	42.7	8.09E-08	7.38E-08
315	HR 191	42.8	7.32E-08	7.50E-08
316	HR 192	42.9	7.70E-08	7.73E-08
317	HR 193	43	7.66E-08	8.08E-08
318	HR 194	43.1	8.14E-08	8.53E-08
319	HR 195	43.2	1.00E-07	8.96E-08
320	HR 196	43.3	9.74E-08	9.25E-08
321	HR 197	43.4	8.35E-08	9.41E-08
322	HR 198	43.5	1.01E-07	9.53E-08
323	HR 199	43.6	9.78E-08	9.57E-08
324	HR 200	43.7	9.21E-08	9.56E-08
325	HR 201	43.8	9.36E-08	9.56E-08
326	HR 202	43.9	9.20E-08	9.59E-08
327	HR 203	44	9.48E-08	9.62E-08
328	HR 204	44.1	1.06E-07	9.55E-08
329	HR 205	44.2	1.09E-07	9.28E-08
330	HR 206	44.3	6.87E-08	8.90E-08
331	HR 207	44.4	8.32E-08	8.70E-08
332	HR 208	44.5	8.58E-08	8.72E-08
333	HR 209	44.6	9.02E-08	8.87E-08
334	HR 210	44.7	9.67E-08	9.04E-08
335	HR 211	44.8	9.16E-08	9.17E-08
336	HR 212	44.9	8.70E-08	9.28E-08
337	HR 213	45	9.62E-08	9.37E-08
338	HR 214	45.1	1.01E-07	9.41E-08
339	HR 215	45.2	9.24E-08	9.38E-08
340	HR 216	45.3	9.48E-08	9.34E-08
341	HR 217	45.4	8.40E-08	9.39E-08
342	HR 218	45.5	9.83E-08	9.58E-08
343	HR 219	45.6	9.95E-08	9.86E-08
344	HR 220	45.7	1.03E-07	1.02E-07

4.1.3. Packrat Section, Eastern Nevada

Serial	Sample #	Height (m)	χ (m^3/Kg)	Spline 0.01
1	PKRT 1A	-10	6.99E-09	7.60E-09
2	PKRT 2A	-9.9	3.96E-09	8.18E-09
3	PKRT 3A	-9.8	1.77E-08	8.50E-09
4	PKRT 4A	-9.7	3.75E-09	8.04E-09
5	PKRT 5A	-9.6	8.97E-09	7.22E-09
6	PKRT 6A	-9.5	5.30E-09	6.26E-09
7	PKRT 7A	-9.4	6.90E-09	5.44E-09
8	PKRT 8A	-9.3	3.32E-09	5.00E-09
9	PKRT 9A	-9.2	4.79E-09	5.31E-09
10	PKRT 10A	-9.1	4.34E-09	6.52E-09
11	PKRT 11A	-9	1.00E-08	8.62E-09
12	PKRT 12A	-8.9	9.34E-09	1.13E-08
13	PKRT 13A	-8.8	8.67E-09	1.43E-08
14	PKRT 14A	-8.7	2.26E-08	1.70E-08
15	PKRT 15A	-8.6	2.30E-08	1.81E-08
16	PKRT 16A	-8.5	2.81E-08	1.71E-08
17	PKRT 17A	-8.4	4.25E-09	1.45E-08
18	PKRT 18A	-8.3	5.91E-09	1.22E-08
19	PKRT 19A	-8.2	7.98E-09	1.11E-08
20	PKRT 20A	-8.1	1.63E-08	1.06E-08
21	PKRT 21A	-8	1.37E-08	9.51E-09
22	PKRT 22A	-7.9	8.58E-09	7.80E-09
23	PKRT 23A	-7.8	2.04E-09	5.97E-09
24	PKRT 24A	-7.7	4.09E-09	4.72E-09
25	PKRT 25A	-7.6	4.68E-09	4.20E-09
26	PKRT 26A	-7.5	2.09E-09	4.38E-09
27	PKRT 27A	-7.4	6.63E-09	5.19E-09
28	PKRT 28A	-7.3	7.28E-09	6.31E-09
29	PKRT 29A	-7.2	3.23E-09	7.59E-09
30	PKRT30A	-7.1	1.17E-08	8.90E-09
31	PKRT 31A	-7	9.70E-09	9.65E-09
32	PKRT 32A	-6.9	1.56E-08	9.47E-09
33	PKRT 33A	-6.8	5.83E-09	8.33E-09
34	PKRT 34A	-6.7	5.75E-09	6.90E-09
35	PKRT 35A	-6.6	5.23E-09	5.70E-09
36	PKRT 36A	-6.5	1.87E-09	4.99E-09
37	PKRT 37A	-6.4	6.71E-09	4.83E-09
38	PKRT 38A	-6.3	7.08E-09	4.91E-09
39	PKRT 39A	-6.2	7.64E-09	5.15E-09
40	PKRT 40A	-6.1	2.25E-09	5.89E-09
41	PKRT 41A	-6	4.57E-09	7.75E-09

42	PKRT 42A	-5.9	7.15E-09	1.09E-08
43	PKRT 43A	-5.8	1.43E-08	1.47E-08
44	PKRT 44A	-5.7	2.61E-08	1.80E-08
45	PKRT 45A	-5.6	2.83E-08	1.98E-08
46	PKRT 46A	-5.5	1.51E-08	2.04E-08
47	PKRT 47A	-5.4	7.33E-09	2.13E-08
48	PKRT 48A	-5.3	2.77E-08	2.31E-08
49	PKRT 49A	-5.2	2.81E-08	2.45E-08
50	PKRT 50A	-5.1	2.86E-08	2.47E-08
51	PKRT 51A	-5	2.15E-08	2.33E-08
52	PKRT 52A	-4.9	2.97E-08	2.07E-08
53	PKRT 53A	-4.8	1.28E-08	1.74E-08
54	PKRT 54A	-4.7	8.36E-09	1.51E-08
55	PKRT 55A	-4.6	8.05E-09	1.48E-08
56	PKRT 56A	-4.5	4.21E-09	1.61E-08
57	PKRT 57A	-4.4	5.33E-08	1.72E-08
58	PKRT 01	-4.3	5.43E-09	1.59E-08
59	PKRT 02	-4.2	1.46E-08	1.37E-08
60	PKRT 03	-4.1	8.47E-09	1.22E-08
61	PKRT 04	-4	5.48E-09	1.25E-08
62	PKRT 05	-3.9	9.50E-09	1.50E-08
63	PKRT 06	-3.8	2.54E-08	1.91E-08
64	PKRT 07	-3.7	2.38E-08	2.32E-08
65	PKRT 08	-3.6	2.98E-08	2.63E-08
66	PKRT 09	-3.5	2.63E-08	2.82E-08
67	PKRT 10	-3.4	3.17E-08	2.86E-08
68	PKRT 11	-3.3	2.13E-08	2.76E-08
69	PKRT 12	-3.2	3.35E-08	2.53E-08
70	PKRT 13	-3.1	2.91E-08	2.11E-08
71	PKRT 14	-3	8.38E-09	1.59E-08
72	PKRT 15	-2.9	5.91E-09	1.15E-08
73	PKRT 16	-2.8	6.17E-09	8.84E-09
74	PKRT 17	-2.7	1.06E-08	7.64E-09
75	PKRT 18	-2.6	7.44E-09	7.32E-09
76	PKRT 19	-2.5	7.48E-09	7.54E-09
77	PKRT 20	-2.4	7.10E-09	8.09E-09
78	PKRT 21	-2.3	1.14E-08	8.74E-09
79	PKRT 22	-2.2	5.87E-09	9.17E-09
80	PKRT 23	-2.1	1.48E-08	9.32E-09
81	PKRT 24	-2	7.38E-09	8.93E-09
82	PKRT 25	-1.9	6.26E-09	8.31E-09
83	PKRT 26	-1.8	9.29E-09	7.70E-09
84	PKRT 27	-1.7	8.77E-09	7.05E-09
85	PKRT 28	-1.6	7.27E-09	6.50E-09

86	PKRT 29	-1.5	3.94E-09	6.52E-09
87	PKRT 30	-1.4	7.20E-09	7.65E-09
88	PKRT 31	-1.3	6.71E-09	1.01E-08
89	PKRT 32	-1.2	7.20E-09	1.38E-08
90	PKRT 33	-1.1	2.70E-08	1.80E-08
91	PKRT 34	-1	1.64E-08	2.12E-08
92	PKRT 35	-0.9	3.45E-08	2.30E-08
93	PKRT 36	-0.8	1.74E-08	2.27E-08
94	PKRT 37	-0.7	2.61E-08	2.10E-08
95	PKRT 38	-0.6	1.46E-08	1.83E-08
96	PKRT 39	-0.5	1.71E-08	1.55E-08
97	PKRT 40	-0.4	9.91E-09	1.33E-08
98	PKRT 41	-0.3	1.54E-08	1.22E-08
99	PKRT 42	-0.2	1.09E-08	1.25E-08
100	PKRT 43	-0.1	1.16E-08	1.48E-08
101	PKRT 44	0	1.11E-08	1.92E-08
102	PKRT 45	0.1	2.70E-08	2.55E-08
103	PKRT 46	0.2	3.79E-08	3.20E-08
104	PKRT 47	0.3	3.95E-08	3.72E-08
105	PKRT 48	0.4	4.07E-08	4.07E-08
106	PKRT 49	0.5	4.87E-08	4.23E-08
107	PKRT 50	0.6	4.11E-08	4.25E-08
108	PKRT 51	0.7	4.23E-08	4.21E-08
109	PKRT 52	0.8	4.16E-08	4.25E-08
110	PKRT 53	0.9	3.64E-08	4.45E-08
111	PKRT 54	1	4.49E-08	4.89E-08
112	PKRT 55	1.1	4.84E-08	5.50E-08
113	PKRT 56	1.2	6.50E-08	6.14E-08
114	PKRT 57	1.3	6.75E-08	6.56E-08
115	PKRT 58	1.4	9.49E-08	6.53E-08
116	PKRT 59	1.5	5.42E-08	5.97E-08
117	PKRT 60	1.6	3.95E-08	5.20E-08
118	PKRT 61	1.7	3.96E-08	4.50E-08
119	PKRT 62	1.8	5.77E-08	3.95E-08
120	PKRT 63	1.9	3.09E-08	3.58E-08
121	PKRT 64	2	1.74E-08	3.64E-08
122	PKRT 65	2.1	2.37E-08	4.28E-08
123	PKRT 66	2.2	6.46E-08	5.36E-08
124	PKRT 67	2.3	7.42E-08	6.43E-08
125	PKRT 68	2.4	9.51E-08	7.15E-08
126	PKRT 69	2.5	6.73E-08	7.46E-08
127	PKRT 70	2.6	6.88E-08	7.58E-08
128	PKRT 71	2.7	7.73E-08	7.73E-08
129	PKRT 72	2.8	7.11E-08	7.99E-08

130	PKRT 73	2.9	7.27E-08	8.39E-08
131	PKRT 74	3	1.06E-07	8.80E-08
132	PKRT 75	3.1	1.05E-07	8.98E-08
133	PKRT 76	3.2	6.27E-08	8.94E-08
134	PKRT 77	3.3	9.57E-08	8.87E-08
135	PKRT 78	3.4	9.69E-08	8.67E-08
136	PKRT 79	3.5	9.21E-08	8.28E-08
137	PKRT 80	3.6	7.51E-08	7.83E-08
138	PKRT 81	3.7	5.72E-08	7.60E-08
139	PKRT 82	3.8	6.96E-08	7.79E-08
140	PKRT 83	3.9	8.06E-08	8.31E-08
141	PKRT 84	4	1.12E-07	8.89E-08
142	PKRT 85	4.1	9.82E-08	9.29E-08
143	PKRT 86	4.2	7.81E-08	9.57E-08
144	PKRT 87	4.3	1.05E-07	9.87E-08
145	PKRT 88	4.4	9.48E-08	1.02E-07
146	PKRT 89	4.5	1.12E-07	1.04E-07
147	PKRT 90	4.6	1.08E-07	1.05E-07
148	PKRT 91	4.7	9.64E-08	1.05E-07
149	PKRT 92	4.8	1.07E-07	1.04E-07
150	PKRT 93	4.9	1.10E-07	1.01E-07
151	PKRT 94	5	1.14E-07	9.67E-08
152	PKRT 95	5.1	6.32E-08	9.15E-08
153	PKRT 96	5.2	8.65E-08	8.90E-08
154	PKRT 97	5.3	9.84E-08	8.90E-08
155	PKRT 98	5.4	8.91E-08	9.05E-08
156	PKRT 99	5.5	8.23E-08	9.35E-08
157	PKRT 100	5.6	9.74E-08	9.78E-08
158	PKRT 101	5.7	1.19E-07	1.02E-07
159	PKRT 102	5.8	1.01E-07	1.03E-07
160	PKRT 103	5.9	1.01E-07	1.04E-07
161	PKRT 104	6	1.09E-07	1.03E-07
162	PKRT 105	6.1	8.75E-08	1.03E-07
163	PKRT 106	6.2	1.02E-07	1.03E-07
164	PKRT 107	6.3	1.10E-07	1.02E-07
165	PKRT 108	6.4	1.13E-07	9.98E-08
166	PKRT 109	6.5	9.81E-08	9.53E-08
167	PKRT 110	6.6	7.67E-08	9.08E-08
168	PKRT 111	6.7	7.80E-08	8.87E-08
169	PKRT 112	6.8	1.06E-07	8.94E-08
170	PKRT 113	6.9	7.58E-08	9.16E-08
171	PKRT 114	7	9.93E-08	9.58E-08
172	PKRT 115	7.1	9.76E-08	1.01E-07
173	PKRT 116	7.2	1.10E-07	1.05E-07

174	PKRT 117	7.3	1.14E-07	1.07E-07
175	PKRT 118	7.4	1.13E-07	1.07E-07
176	PKRT 119	7.5	1.14E-07	1.04E-07
177	PKRT 120	7.6	8.71E-08	1.01E-07
178	PKRT 121	7.7	7.39E-08	1.01E-07
179	PKRT 122	7.8	1.20E-07	1.04E-07
180	PKRT 123	7.9	1.24E-07	1.08E-07
181	PKRT 124	8	9.87E-08	1.12E-07
182	PKRT 125	8.1	1.02E-07	1.17E-07
183	PKRT 126	8.2	1.37E-07	1.22E-07
184	PKRT 127	8.3	1.22E-07	1.26E-07
185	PKRT 128	8.4	1.36E-07	1.28E-07
186	PKRT 129	8.5	1.38E-07	1.26E-07
187	PKRT 130	8.6	1.07E-07	1.21E-07
188	PKRT 131	8.7	1.12E-07	1.16E-07
189	PKRT 132	8.8	1.17E-07	1.11E-07
190	PKRT 133	8.9	1.14E-07	1.05E-07
191	PKRT 134	9	9.81E-08	9.97E-08
192	PKRT 135	9.1	7.50E-08	9.61E-08
193	PKRT 136	9.2	9.94E-08	9.57E-08
194	PKRT 137	9.3	1.05E-07	9.70E-08

4.2. Carbonate Contents ($CaCO_3$%) Measurements

4.2.1. GSSP Section, Drum Mountains, Western Utah

Serial	Sample #	Height	$CaCO_3$%	0.01 spline
1	DM -25	55	100	88.49
2	DM -24	55.1	89.21	85.17
3	DM -23	55.2	48.50	84.28
4	DM -22	55.3	94.20	87.62
5	DM -21	55.4	100	92.55
6	DM -20	55.5	100	96.40
7	DM -19	55.6	98.44	98.01
8	DM -18	55.7	100	97.03
9	DM -17	55.8	99.91	93.41
10	DM -16	55.9	99.78	87.77
11	DM -15	56	50.42	82.13
12	DM -14	56.1	100	79.25
13	DM -13	56.2	41.70	78.77
14	DM -12	56.3	98.14	80.83
15	DM -11	56.4	97.68	81.93
16	DM -10	56.5	99.23	80.14
17	DM -09	56.6	48.26	76.86
18	DM -08	56.7	74.73	75.60
19	DM -07	56.8	62.97	76.68
20	DM -06	56.9	95.30	78.87
21	DM -05	57	99.52	79.65
22	DM -04	57.1	54.73	78.89
23	DM -03	57.2	63.18	78.85
24	DM -02	57.3	94.48	78.72
25	DM -01	57.4	96.97	75.31
26	DM 01	57.5	77.57	71.93
27	DM 02	57.55	63.63	67.76
28	DM 03	57.6	67.71	63.30
29	DM 04	57.65	62.73	59.03
30	DM 05	57.7	33.82	55.50
31	DM 06	57.75	32.85	53.26
32	DM 07	57.8	45.81	52.41
33	DM 08	57.85	50.25	52.60
34	DM 09	57.9	71.75	53.29
35	DM 10	57.95	69.65	53.93
36	DM 11	58	50.32	54.34
37	DM 12	58.05	43.83	54.66
38	DM 13	58.1	74.21	54.99
39	DM 14	58.15	39.30	55.31
40	DM 15	58.2	46.67	55.81

41	DM 16	58.25	58.97	56.44
42	DM 17	58.3	80.91	56.97
43	DM 18	58.35	49.68	57.25
44	DM 19	58.4	54.23	57.51
45	DM 20	58.45	44.72	57.95
46	DM 21	58.5	51.67	58.63
47	DM 22	58.55	69.19	59.34
48	DM 23	58.6	74.89	59.74
49	DM 24	58.65	43.20	59.68
50	DM 25	58.7	80.58	59.26
51	DM 26	58.75	49.14	58.43
52	DM 27	58.8	50.05	57.41
53	DM 28	58.85	52.57	56.30
54	DM 29	58.9	74.80	55.05
55	DM 30	58.95	48.31	53.59
56	DM 31	59	45.15	52.11
57	DM 32	59.05	50.95	50.82
58	DM 33	59.1	48.93	49.75
59	DM 34	59.15	48.70	48.93
60	DM 35	59.2	45.86	48.34
61	DM 36	59.25	48.24	47.98
62	DM 37	59.3	50.57	47.78
63	DM 38	59.35	46.55	47.69
64	DM 39	59.4	47.30	47.71
65	DM 40	59.45	48.65	47.81
66	DM 41	59.5	49.10	47.96
67	DM 42	59.55	47.84	48.17
68	DM 43	59.6	51.59	48.43
69	DM 44	59.65	48.20	48.78
70	DM 45	59.7	45.84	49.28
71	DM 46	59.75	42.39	50.00
72	DM 47	59.8	42.74	50.91
73	DM 48	59.85	44.31	51.80
74	DM 49	59.9	74.98	52.27
75	DM 50	59.95	74.62	51.85
76	DM 51	60	39.16	50.51
77	DM 52	60.05	41.70	48.66
78	DM 53	60.1	49.73	46.57
79	DM 54	60.15	43.16	44.37
80	DM 55	60.2	44.75	42.21
81	DM 56	60.25	37.05	40.23
82	DM 57	60.3	33.01	38.60
83	DM 58	60.35	37.81	37.44
84	DM 59	60.4	35.17	36.75

85	DM 60	60.45	32.91	36.50
86	DM 61	60.5	39.92	36.63
87	DM 62	60.55	38.90	37.03
88	DM 63	60.6	31.57	37.64
89	DM 64	60.65	36.74	38.40
90	DM 65	60.7	37.81	39.17
91	DM 66	60.75	41.58	39.75
92	DM 67	60.8	56.69	39.89
93	DM 68	60.85	39.33	39.48
94	DM 69	60.9	38.77	38.67
95	DM 70	60.95	31.91	37.68
96	DM 71	61	33.22	36.70
97	DM 72	61.05	35.99	35.82
98	DM 73	61.1	32.72	35.06
99	DM 74	61.15	37.94	34.40
100	DM 75	61.2	29.41	33.79
101	DM 76	61.25	35.17	33.25
102	DM 77	61.3	36.63	32.69
103	DM 78	61.35	33.48	32.11
104	DM 79	61.4	22.64	31.55
105	DM 80	61.45	35.51	31.06
106	DM 81	61.5	31.31	30.59
107	DM 82	61.55	34.34	30.09
108	DM 83	61.6	30.49	29.59
109	DM 84	61.65	26.98	29.18
110	DM 85	61.7	26.68	28.98
111	DM 86	61.75	27.37	29.07
112	DM 87	61.8	30.05	29.47
113	DM 88	61.85	31.48	30.17
114	DM 89	61.9	37.34	31.17
115	DM 90	61.95	32.74	32.51
116	DM 91	62	25.43	34.35
117	DM 92	62.05	12.13	36.82
118	DM 93	62.1	50.49	39.83
119	DM 94	62.15	55.55	42.88
120	DM 95	62.2	56.45	45.57
121	DM 96	62.25	44.38	47.84
122	DM 97	62.3	56.50	49.81
123	DM 98	62.35	51.62	51.66
124	DM 99	62.4	39.04	53.62
125	DM 100	62.45	54.83	55.92
126	DM 101	62.5	42.49	58.52
127	DM 102	62.55	60.23	61.27
128	DM 103	62.6	72.68	63.70

129	DM 104	62.65	75.30	65.32
130	DM 105	62.7	69.88	65.82
131	DM 106	62.75	74.32	65.11
132	DM 107	62.8	62.90	63.24
133	DM 108	62.85	58.60	60.46
134	DM 109	62.9	65.36	57.00
135	DM 110	62.95	49.31	53.12
136	DM 111	63	55.97	49.20
137	DM 112	63.05	53.53	45.60
138	DM 113	63.1	31.67	42.82
139	DM 114	63.15	14.30	41.49
140	DM 115	63.2	31.06	41.93
141	DM 116	63.25	43.74	43.97
142	DM 117	63.3	53.27	47.10
143	DM 118	63.35	55.95	50.80
144	DM 119	63.4	51.80	54.70
145	DM 120	63.45	77.40	58.49
146	DM 121	63.5	50.62	61.93
147	DM 122	63.55	61.02	65.04
148	DM 123	63.6	71.21	67.71
149	DM 124	63.65	78.91	69.72
150	DM 125	63.7	74.61	70.94
151	DM 126	63.75	68.44	71.42
152	DM 127	63.8	72.57	71.32
153	DM 128	63.85	71.27	70.72
154	DM 129	63.9	71.88	69.76
155	DM 130	63.95	61.62	68.57
156	DM 131	64	76.90	67.32
157	DM 132	64.05	67.80	66.08
158	DM 133	64.1	53.83	65.08
159	DM 134	64.15	54.31	64.56
160	DM 135	64.2	71.84	64.55
161	DM 136	64.25	63.47	64.87
162	DM 137	64.3	67.35	65.45
163	DM 138	64.35	67.15	66.20
164	DM 139	64.4	58.55	67.07
165	DM 140	64.45	74.58	68.00
166	DM 141	64.5	67.75	68.83
167	DM 142	64.55	66.83	69.45
168	DM 143	64.6	77.21	69.77
169	DM 144	64.65	62.50	69.66
170	DM 145	64.7	74.09	69.09
171	DM 146	64.75	66.84	67.95
172	DM 147	64.8	66.45	66.20

173	DM 148	64.85	67.47	63.78
174	DM 149	64.9	72.74	60.66
175	DM 150	64.95	63.10	56.91
176	DM 151	65	53.47	52.85
177	DM 152	65.05	50.21	48.96
178	DM 153	65.1	43.71	45.75
179	DM 154	65.15	44.55	43.76
180	DM 155	65.2	16.43	43.50
181	DM 156	65.25	21.67	45.35
182	DM 157	65.3	64.98	49.19
183	DM 158	65.35	31.76	54.40
184	DM 159	65.4	67.53	60.48
185	DM 160	65.45	77.05	66.63
186	DM 161	65.5	90.09	72.10
187	DM 162	65.55	82.99	76.45
188	DM 163	65.6	88.83	79.57
189	DM 164	65.65	87.12	81.62
190	DM 165	65.7	52.96	82.92
191	DM 166	65.75	88.09	83.83
192	DM 167	65.8	97.36	84.23
193	DM 168	65.85	97.57	84.01
194	DM 169	65.9	81.93	83.35
195	DM 170	65.95	56.09	82.70
196	DM 171	66	83.34	82.44
197	DM 172	66.05	95.00	82.51
198	DM 173	66.1	65.42	82.78
199	DM 174	66.15	97.08	83.29
200	DM 175	66.2	93.88	83.89
201	DM 176	66.25	64.00	84.62
202	DM 177	66.3	90.50	85.66
203	DM 178	66.35	81.05	86.92
204	DM 179	66.4	94.07	88.27
205	DM 180	66.45	97.88	89.54
206	DM 181	66.5	92.04	90.64
207	DM 182	66.55	77.83	91.68
208	DM 183	66.6	96.06	92.75
209	DM 184	66.65	91.29	93.73
210	DM 185	66.7	98.84	94.50
211	DM 186	66.75	98.09	94.91
212	DM 187	66.8	100	94.92
213	DM 188	66.85	97.36	94.55
214	DM 189	66.9	95.81	93.95
215	DM 190	66.95	67.53	93.33
216	DM 191	67	97.40	92.86

217	DM 192	67.05	97.26	92.29
218	DM 193	67.1	93.24	91.36
219	DM 194	67.15	92.44	89.92
220	DM 195	67.2	98.80	87.89
221	DM 196	67.25	90.53	85.27
222	DM 197	67.3	69.17	82.29
223	DM 198	67.35	77.33	79.25
224	DM 199	67.4	84.05	76.26
225	DM 200	67.45	63.74	73.35
226	DM 201	67.5	62.35	70.65
227	DM 202	67.55	89.09	68.12
228	DM 203	67.6	62.50	65.64
229	DM 204	67.65	54.71	63.38
230	DM 205	67.7	59.17	61.51
231	DM 206	67.75	64.70	60.04
232	DM 207	67.8	55.56	58.91
233	DM 208	67.85	55.31	58.14
234	DM 209	67.9	55.52	57.68
235	DM 210	67.95	62.19	57.41
236	DM 211	68	56.24	57.19
237	DM 212	68.05	60.93	56.95
238	DM 213	68.1	56.97	56.64
239	DM 214	68.15	57.32	56.25
240	DM 215	68.2	55.75	55.83
241	DM 216	68.25	52.26	55.44
242	DM 217	68.3	58.38	55.11
243	DM 218	68.35	54.90	54.85
244	DM 219	68.4	56.16	54.71
245	DM 220	68.45	51.73	54.75
246	DM 221	68.5	53.80	55.06
247	DM 222	68.55	56.81	55.66
248	DM 223	68.6	53.32	56.55
249	DM 224	68.65	55.72	57.73
250	DM 225	68.7	51.45	59.15
251	DM 226	68.75	60.45	60.66
252	DM 227	68.8	69.60	62.00
253	DM 228	68.85	65.73	62.89
254	DM 229	68.9	71.72	63.19
255	DM 230	68.95	56.96	62.87
256	DM 231	69	60.37	62.03
257	DM 232	69.05	58.40	60.72
258	DM 233	69.1	58.32	58.90
259	DM 234	69.15	56.56	56.50
260	DM 235	69.2	58.56	53.42

261	DM 236	69.25	48.53	49.59
262	DM 237	69.3	45.24	45.01
263	DM 238	69.35	44.14	39.69
264	DM 239	69.4	48.03	33.67
265	DM 240	69.45	48.88	27.11
266	DM 241	69.5	0.16	20.51
267	DM 242	69.55	0.21	14.74
268	DM 243	69.6	0.06	10.33
269	DM 244	69.65	0.41	7.44
270	DM 245	69.7	-0.14	6.00
271	DM 246	69.75	2.99	5.73
272	DM 247	69.8	16.23	6.21
273	DM 248	69.85	1.78	6.99
274	DM 249	69.9	20.94	7.76
275	DM 250	69.95	8.93	8.21
276	DM 251	70	18.53	8.24
277	DM 252	70.05	6.67	7.85
278	DM 253	70.1	0.75	7.23
279	DM 254	70.15	13.19	6.54
280	DM 255	70.2	0.28	5.88
281	DM 256	70.25	1.95	5.38
282	DM 257	70.3	7.92	5.12
283	DM 258	70.35	0.59	5.10
284	DM 259	70.4	5.56	5.32
285	DM 260	70.45	7.61	5.74
286	DM 261	70.5	0.02	6.31
287	DM 262	70.55	12.85	6.96
288	DM 263	70.6	7.87	7.58
289	DM 264	70.65	14.85	8.11
290	DM 265	70.7	11.64	8.57
291	DM 266	70.75	6.29	9.09
292	DM 267	70.8	1.66	9.86
293	DM 268	70.85	22.87	11.02
294	DM 269	70.9	16.61	12.61
295	DM 270	70.95	3.54	14.83
296	DM 271	71	8.35	17.98
297	DM 272	71.05	0.12	22.11
298	DM 273	71.1	1.10	27.01
299	DM 274	71.15	49.59	31.93
300	DM 275	71.2	87.70	35.67
301	DM 276	71.25	3.41	37.45
302	DM 277	71.3	80.19	37.28
303	DM 278	71.35	81.69	34.99
304	DM 279	71.4	1.40	31.19

305	DM 280	71.45	0.71	27.32
306	DM 281	71.5	1.56	24.40
307	DM 282	71.55	19.20	22.79
308	DM 283	71.6	73.84	22.35
309	DM 284	71.65	0.52	23.01
310	DM 285	71.7	0.90	25.41
311	DM 286	71.75	0.50	29.97
312	DM 287	71.8	0.71	36.47
313	DM 288	71.85	75.93	43.93
314	DM 289	71.9	79.42	50.81
315	DM 290	71.95	76.11	56.07
316	DM 291	72	69.29	59.35
317	DM 292	72.05	69.11	60.79
318	DM 293	72.1	76.26	60.82
319	DM 294	72.15	18.26	60.11
320	DM 295	72.2	79.85	59.45
321	DM 296	72.25	81.04	59.08
322	DM 297	72.3	25.63	59.50
323	DM 298	72.35	16.01	61.51
324	DM 299	72.4	77.64	65.26
325	DM 300	72.45	65.07	70.05
326	DM 301	72.5	90.92	75.16
327	DM 302	72.55	93.05	79.93
328	DM 303	72.6	89.91	83.98
329	DM 304	72.65	90.14	87.24
330	DM 305	72.7	83.48	89.81
331	DM 306	72.75	93.69	91.82
332	DM +01	72.85	91.54	94.46
333	DM +02	72.95	97.11	95.58
334	DM +03	73.05	96.98	95.33
335	DM +04	73.15	90.66	93.99
336	DM +05	73.25	88.27	92.03
337	DM +06	73.35	91.59	89.39
338	DM +07	73.45	92.98	85.48
339	DM +08	73.55	89.28	80.10
340	DM +09	73.65	46.09	74.48
341	DM +10	73.75	80.06	70.32
342	DM +11	73.85	77.15	66.21
343	DM +12	73.95	71.37	61.43
344	DM +13	74.05	31.11	57.40
345	DM +14	74.15	62.08	56.31
346	DM +15	74.25	47.96	57.42
347	DM +16	74.35	68.17	59.54
348	DM +17	74.45	51.83	60.69

349	DM +18	74.55	96.61	59.45
350	DM +19	74.65	35.66	54.73
351	DM +20	74.75	50.34	49.47
352	DM +21	74.85	46.53	45.35
353	DM +22	74.95	39.63	43.53
354	DM +23	75.05	26.68	45.27
355	DM +24	75.15	40.61	50.69
356	DM +25	75.25	86.05	57.00
357	DM +26	75.35	55.20	60.39
358	DM +27	75.45	76.42	60.44
359	DM +28	75.55	54.85	57.51
360	DM +29	75.65	55.03	53.84
361	DM +30	75.75	43.25	51.90
362	DM +31	75.85	38.91	53.93
363	DM +32	75.95	43.89	60.55
364	DM +33	76.05	89.40	69.54
365	DM +34	76.15	94.64	76.63
366	DM +35	76.25	80.61	80.23
367	DM +36	76.35	66.75	81.82
368	DM +37	76.45	86.35	83.05
369	DM +38	76.55	85.09	83.66
370	DM +39	76.65	90.67	83.39
371	DM +40	76.75	65.07	82.53
372	DM +41	76.85	96.92	81.78
373	DM +42	76.95	71.74	80.29
374	DM +43	77.05	88.01	78.33
375	DM +44	77.15	89.71	75.89
376	DM +45	77.25	31.53	74.40
377	DM +46	77.35	85.48	76.05
378	DM +47	77.45	90.93	78.06
379	DM +48	77.55	81.66	77.93
380	DM +49	77.65	91.93	75.31
381	DM +50	77.75	50.52	71.34
382	DM +51	77.85	81.72	68.79
383	DM +52	77.95	31.75	68.65
384	DM +53	78.05	93.68	71.69
385	DM +54	78.15	78.64	74.96
386	DM +55	78.25	81.66	77.30
387	DM +56	78.35	63.32	78.95
388	DM +57	78.45	94.73	80.30
389	DM +58	78.55	82.87	80.30
390	DM +59	78.65	75.75	79.40
391	DM +60	78.75	72.03	78.72
392	DM +61	78.85	81.21	78.79

393	DM +62	78.95	74.53	79.19
394	DM +63	79.05	81.10	79.46
395	DM +64	79.15	84.18	78.63
396	DM +65	79.25	84.09	75.99
397	DM +66	79.35	78.74	71.91
398	DM +67	79.45	69.53	68.23
399	DM +68	79.55	22.96	68.02
400	DM +69	79.65	82.82	73.26
401	DM +70	79.75	92.37	80.28
402	DM +71	79.85	93.83	85.58
403	DM +72	79.95	90.29	87.87
404	DM +73	80.05	92.45	87.45
405	DM +74	80.15	75.18	85.37
406	DM +75	80.25	87.84	83.10
407	DM +76	80.35	71.12	81.07
408	DM +77	80.45	87.03	79.68
409	DM +78	80.55	77.49	78.40
410	DM +79	80.65	80.64	77.32
411	DM +80	80.75	69.93	76.75
412	DM +81	80.85	78.91	77.21
413	DM +82	80.95	77.17	78.47
414	DM +83	81.05	80.15	80.24
415	DM +84	81.15	78.74	82.13
416	DM +85	81.25	83.75	83.58
417	DM +86	81.35	99.19	83.56
418	DM +87	81.45	75.37	81.50
419	DM +88	81.55	75.09	78.68
420	DM +89	81.65	79.46	75.99
421	DM +90	81.75	80.68	73.74
422	DM +91	81.85	49.73	72.82
423	DM +92	81.95	79.72	74.39
424	DM +93	82.05	81.86	76.93
425	DM +94	82.15	87.42	79.03
426	DM +95	82.25	76.01	80.41
427	DM +96	82.35	83.00	81.91
428	DM +97	82.45	69.56	84.09
429	DM +98	82.55	91.71	87.04
430	DM +99	82.65	97.75	89.11
431	DM +100	82.75	77.21	89.07
432	DM +101	82.85	96.02	86.58
433	DM +102	82.95	97.11	80.36
434	DM +103	83.05	85.56	70.52
435	DM +104	83.15	31.36	60.23
436	DM +105	83.25	48.02	54.27

437	DM +106	83.35	59.12	53.85
438	DM +107	83.45	26.57	58.56
439	DM +108	83.55	91.24	67.43
440	DM +109	83.65	78.56	76.18
441	DM +110	83.75	92.48	82.73
442	DM +111	83.85	86.90	86.43
443	DM +112	83.95	90.09	88.02
444	DM +113	84.05	89.19	88.71
445	DM +114	84.15	70.90	90.01
446	DM +115	84.25	96.55	92.92
447	DM +116	84.35	102.90	96.03
448	DM +117	84.45	99.83	98.01
449	DM +118	84.55	100	98.64
450	DM +119	84.65	97.48	98.21
451	DM +120	84.75	98.21	97.21
452	DM +121	84.85	94.07	96.16
453	DM +122	84.95	91.88	95.58
454	DM +123	85.05	96.63	95.65
455	DM +124	85.15	97.04	96.01
456	DM +125	85.25	95.66	96.33
457	DM +126	85.35	98.68	96.44
458	DM +127	85.45	98.00	96.19
459	DM +128	85.55	94.48	95.77
460	DM +129	85.65	92.28	95.63
461	DM +130	85.75	96.00	96.01
462	DM +131	85.85	96.00	96.65
463	DM +132	85.95	99.15	97.17
464	DM +133	86.05	99.05	97.14
465	DM +134	86.15	98.22	96.48
466	DM +135	86.25	92.10	95.44
467	DM +136	86.35	97.23	94.49
468	DM +137	86.45	94.14	93.79
469	DM +138	86.55	86.54	93.78
470	DM +139	86.65	97.22	94.77
471	DM +140	86.75	98.12	96.23

4.2.2. Marjum Pass Section, House Range, Western Utah

Serial	Sample #	Height	$CaCO_3$%	0.01 spline
1	HR -124	0	100	98.95
2	HR -123	0.62	6.41	9.82
3	HR -122	1.24	49.38	45.50
4	HR -121	1.86	3.93	5.91
5	HR -120	2.48	27.43	28.23
6	HR -119	3.1	90.11	88.29
7	HR -118	3.72	50.02	49.67
8	HR -117	4.34	0.00	3.01
9	HR -116	4.96	49.12	45.60
10	HR -115	5.58	0.15	2.04
11	HR -114	6.2	2.67	2.87
12	HR -113	6.82	38.10	36.97
13	HR -112	7.44	39.98	41.09
14	HR -111	8.06	60.88	60.05
15	HR -110	8.68	56.74	57.16
16	HR -109	9.3	55.60	55.34
17	HR -108	9.92	56.99	57.73
18	HR -107	10.54	65.62	64.28
19	HR -106	11.16	28.52	29.74
20	HR -105	11.78	23.25	22.36
21	HR -104	12.4	19.57	21.08
22	HR -103	13.02	41.39	32.45
23	HR -102	13.6	26.86	29.07
24	HR -101	13.7	21.52	25.67
25	HR -100	13.8	12.65	23.32
26	HR -099	13.9	33.01	22.11
27	HR -098	14	22.76	20.93
28	HR -097	14.1	14.67	19.82
29	HR -096	14.2	21.65	19.27
30	HR -095	14.3	19.98	19.20
31	HR -094	14.4	20.16	19.74
32	HR -093	14.5	13.86	21.18
33	HR -092	14.6	22.08	23.68
34	HR -091	14.7	27.86	26.36
35	HR -090	14.8	40.98	27.94
36	HR -089	14.9	24.26	27.73
37	HR -088	15	19.85	26.70
38	HR -087	15.1	31.25	25.56
39	HR -086	15.2	20.00	24.19
40	HR -085	15.3	27.93	22.86
41	HR -084	15.4	18.05	21.64
42	HR -083	15.5	21.61	21.01

43	HR -082	15.6	15.21	21.17
44	HR -081	15.7	22.77	22.07
45	HR -080	15.8	26.93	22.94
46	HR -079	15.9	27.26	23.00
47	HR -078	16	22.82	22.19
48	HR -077	16.1	15.39	21.16
49	HR -076	16.2	18.32	20.61
50	HR -075	16.3	24.94	20.40
51	HR -074	16.4	18.19	20.04
52	HR -073	16.5	24.32	19.52
53	HR -072	16.6	19.83	18.88
54	HR -071	16.7	8.14	18.80
55	HR -070	16.8	18.07	19.86
56	HR -069	16.9	33.97	21.21
57	HR -068	17	19.49	21.81
58	HR -067	17.1	22.12	22.21
59	HR -066	17.2	16.99	23.06
60	HR -065	17.3	27.80	24.73
61	HR -064	17.4	25.31	26.85
62	HR -063	17.5	22.12	29.25
63	HR -062	17.6	42.31	31.37
64	HR -061	17.7	33.82	32.05
65	HR -060	17.8	31.31	31.39
66	HR -059	17.9	30.15	30.11
67	HR -058	18	21.32	28.95
68	HR -057	18.1	30.87	28.42
69	HR -056	18.2	24.79	28.08
70	HR -055	18.3	34.29	27.48
71	HR -054	18.4	24.83	26.02
72	HR -053	18.5	31.82	23.85
73	HR -052	18.6	15.61	21.47
74	HR -051	18.7	17.45	20.20
75	HR -050	18.8	15.29	20.76
76	HR -049	18.9	15.15	23.12
77	HR -048	19	35.17	26.17
78	HR -047	19.1	44.18	27.85
79	HR -046	19.2	22.30	27.57
80	HR -045	19.3	17.30	27.06
81	HR -044	19.4	23.36	27.55
82	HR -043	19.5	45.56	28.65
83	HR -042	19.6	18.72	29.68
84	HR -041	19.7	23.84	31.67
85	HR -040	19.8	43.98	34.52
86	HR -039	19.9	35.46	37.02

87	HR -038	20	34.32	38.91
88	HR -037	20.1	31.95	39.91
89	HR -036	20.2	71.85	38.77
90	HR -035	20.3	23.65	34.15
91	HR -034	20.4	31.31	28.52
92	HR -033	20.5	12.10	24.13
93	HR -032	20.6	10.96	22.84
94	HR -031	20.7	30.30	24.62
95	HR -030	20.8	33.06	27.63
96	HR -029	20.9	28.38	30.60
97	HR -028	21	42.83	33.07
98	HR -027	21.1	29.27	34.81
99	HR -026	21.2	34.19	36.60
100	HR -025	21.3	38.36	38.76
101	HR -024	21.4	45.42	41.09
102	HR -023	21.5	35.29	43.37
103	HR -022	21.6	40.62	45.71
104	HR -021	21.7	49.36	47.09
105	HR -020	21.8	75.63	45.64
106	HR -019	21.9	27.46	40.60
107	HR -018	22	32.13	34.87
108	HR -017	22.1	23.10	30.49
109	HR -016	22.2	28.75	28.47
110	HR -015	22.3	23.11	28.72
111	HR -014	22.4	25.52	30.79
112	HR -013	22.5	29.89	33.29
113	HR -012	22.6	65.05	33.85
114	HR -011	22.7	21.93	30.49
115	HR -010	22.8	20.50	25.00
116	HR -009	22.9	26.11	18.91
117	HR -008	23	5.74	13.11
118	HR -007	23.1	4.68	9.08
119	HR -006	23.2	7.08	7.37
120	HR -005	23.3	5.35	7.70
121	HR -004	23.4	8.79	9.55
122	HR -003	23.5	15.45	12.02
123	HR -002	23.6	22.15	14.16
124	HR -001	23.7	12.86	15.71
125	HR 001	23.8	27.49	17.52
126	HR 002	23.9	7.98	20.62
127	HR 003	24	23.26	26.89
128	HR 004	24.1	22.24	36.72
129	HR 005	24.2	25.31	49.10
130	HR 006	24.3	95.64	60.20

131	HR 007	24.4	90.49	63.71
132	HR 008	24.5	92.66	58.12
133	HR 009	24.6	6.74	47.85
134	HR 010	24.7	17.24	41.45
135	HR 011	24.8	40.25	42.32
136	HR 012	24.9	22.05	49.21
137	HR 013	25	95.04	58.86
138	HR 014	25.1	98.27	65.54
139	HR 015	25.2	8.39	68.54
140	HR 016	25.3	94.38	70.69
141	HR 017	25.4	86.45	68.71
142	HR 018	25.5	53.62	61.04
143	HR 019	25.6	85.34	49.05
144	HR 020	25.7	1.99	34.90
145	HR 021	25.8	1.77	24.27
146	HR 022	25.9	21.82	18.88
147	HR 023	26	24.55	16.47
148	HR 024	26.1	35.78	14.69
149	HR 025	26.2	3.25	13.07
150	HR 026	26.3	5.82	13.89
151	HR 027	26.4	9.30	18.56
152	HR 028	26.5	16.47	26.76
153	HR 029	26.6	58.93	36.36
154	HR 030	26.7	51.10	44.27
155	HR 031	26.8	31.85	50.30
156	HR 032	26.9	74.37	55.31
157	HR 033	27	53.34	58.59
158	HR 034	27.1	47.24	61.13
159	HR 035	27.2	83.41	63.45
160	HR 036	27.3	55.29	64.66
161	HR 037	27.4	51.75	65.79
162	HR 038	27.5	78.07	66.79
163	HR 039	27.6	74.55	65.83
164	HR 040	27.7	47.74	62.39
165	HR 041	27.8	69.01	57.01
166	HR 042	27.9	56.59	48.95
167	HR 043	28	38.41	38.86
168	HR 044	28.1	21.42	28.76
169	HR 045	28.2	14.93	20.66
170	HR 046	28.3	13.71	15.36
171	HR 047	28.4	12.29	12.60
172	HR 048	28.5	14.49	11.71
173	HR 049	28.6	10.11	11.99
174	HR 050	28.7	15.06	13.07

175	HR 051	28.8	15.98	14.47
176	HR 052	28.9	18.54	15.96
177	HR 053	29	16.54	17.68
178	HR 045	29.1	18.83	20.10
179	HR 055	29.2	25.79	23.61
180	HR 056	29.3	20.87	28.45
181	HR 057	29.4	36.99	34.84
182	HR 058	29.5	17.84	42.18
183	HR 059	29.6	70.38	49.05
184	HR 060	29.7	86.67	51.58
185	HR 061	29.8	36.88	49.11
186	HR 062	29.9	26.84	45.96
187	HR 063	30	43.11	45.34
188	HR 064	30.1	39.58	47.45
189	HR 065	30.2	54.52	51.27
190	HR 066	30.3	56.04	54.79
191	HR 067	30.4	80.10	56.19
192	HR 068	30.5	47.42	54.74
193	HR 069	30.6	37.27	52.68
194	HR 070	30.7	62.56	51.57
195	HR 071	30.8	46.24	51.02
196	HR 072	30.9	42.08	51.47
197	HR 073	31	65.64	52.73
198	HR 074	31.1	42.79	53.66
199	HR 075	31.2	71.12	54.15
200	HR 076	31.3	49.82	53.65
201	HR 077	31.4	34.57	53.37
202	HR 078	31.5	65.17	53.96
203	HR 079	31.6	58.97	53.81
204	HR 080	31.7	51.58	52.34
205	HR 081	31.8	52.30	50.01
206	HR 082	31.9	42.94	47.42
207	HR 083	32	42.39	45.32
208	HR 084	32.1	48.55	43.81
209	HR 085	32.2	35.77	42.64
210	HR 086	32.3	44.69	41.85
211	HR 087	32.4	44.97	40.81
212	HR 088	32.5	41.87	39.21
213	HR 089	32.6	35.44	37.45
214	HR 090	32.7	30.12	36.35
215	HR 091	32.8	38.53	36.38
216	HR 092	32.9	31.10	37.14
217	HR 093	33	42.46	38.16
218	HR 094	33.1	42.58	38.32

219	HR 095	33.2	42.67	37.07
220	HR 096	33.3	30.05	34.72
221	HR 097	33.4	25.80	32.33
222	HR 098	33.5	32.96	30.31
223	HR 099	33.6	34.61	28.13
224	HR 100	33.7	23.82	25.60
225	HR 101	33.8	23.43	23.44
226	HR 102	33.9	15.70	22.33
227	HR 103	34	16.88	22.69
228	HR 104	34.1	33.53	23.85
229	HR 105	34.2	26.46	24.46
230	HR 106	34.3	26.82	24.35
231	HR 107	34.4	18.80	24.00
232	HR 108	34.5	25.85	24.14
233	HR 109	34.6	25.57	24.94
234	HR 110	34.7	18.85	26.62
235	HR 111	34.8	31.06	29.31
236	HR 112	34.9	34.87	32.17
237	HR 113	35	35.94	34.43
238	HR 114	35.1	37.36	35.79
239	HR 115	35.2	32.72	36.29
240	HR 116	35.3	38.00	36.11
241	HR 117	35.4	40.38	35.08
242	HR 118	35.5	30.28	33.32
243	HR 119	35.6	31.21	31.64
244	HR 120	35.7	29.03	30.60
245	HR 121	35.8	25.42	30.55
246	HR 122	35.9	34.17	31.43
247	HR 123	36	33.29	32.54
248	HR 124	36.1	38.99	33.43
249	HR 125	36.2	38.04	33.98
250	HR 126	36.3	25.32	34.99
251	HR 127	36.4	26.59	37.69
252	HR 128	36.5	43.81	41.75
253	HR 129	36.6	55.22	45.12
254	HR 130	36.7	51.90	45.99
255	HR 131	36.8	46.41	44.17
256	HR 132	36.9	39.93	40.66
257	HR 133	37	29.11	36.94
258	HR 134	37.1	31.95	34.18
259	HR 135	37.2	36.30	32.45
260	HR 136	37.3	32.93	31.35
261	HR 137	37.4	27.97	30.99
262	HR 138	37.5	29.94	31.73

263	HR 139	37.6	32.32	33.50
264	HR 140	37.7	35.82	35.87
265	HR 141	37.8	39.21	38.17
266	HR 142	37.9	45.84	39.74
267	HR 143	38	36.66	40.25
268	HR 144	38.1	42.95	40.10
269	HR 145	38.2	39.76	39.51
270	HR 146	38.3	31.63	38.98
271	HR 147	38.4	43.29	38.86
272	HR 148	38.5	38.82	38.72
273	HR 149	38.6	33.91	38.45
274	HR 150	38.7	48.89	37.96
275	HR 151	38.8	30.62	36.91
276	HR 152	38.9	38.88	36.06
277	HR 153	39	31.29	35.82
278	HR 154	39.1	38.43	36.56
279	HR 155	39.2	33.63	38.26
280	HR 156	39.3	45.06	40.80
281	HR 157	39.4	36.04	43.67
282	HR 158	39.5	46.63	46.51
283	HR 159	39.6	56.43	48.11
284	HR 160	39.7	52.26	47.26
285	HR 161	39.8	44.19	44.07
286	HR 162	39.9	33.61	39.58
287	HR 163	40	37.70	34.80
288	HR 164	40.1	25.16	30.08
289	HR 165	40.2	33.46	25.75
290	HR 166	40.3	16.25	21.88
291	HR 167	40.4	19.04	19.18
292	HR 168	40.5	16.31	17.88
293	HR 169	40.6	15.22	17.96
294	HR 170	40.7	19.91	19.07
295	HR 171	40.8	28.64	20.50
296	HR 172	40.9	15.36	21.81
297	HR 173	41	18.27	23.46
298	HR 174	41.1	35.01	25.17
299	HR 175	41.2	26.09	26.05
300	HR 176	41.3	24.49	26.38
301	HR 177	41.4	26.03	26.68
302	HR 178	41.5	26.30	27.24
303	HR 179	41.6	34.49	28.11
304	HR 180	41.7	16.03	29.47
305	HR 181	41.8	38.13	31.81
306	HR 182	41.9	31.30	34.30

307	HR 183	42	40.21	36.38
308	HR 184	42.1	37.22	37.43
309	HR 185	42.2	42.08	37.23
310	HR 186	42.3	34.69	35.83
311	HR 187	42.4	28.33	33.89
312	HR 188	42.5	36.64	31.88
313	HR 189	42.6	26.14	29.65
314	HR 190	42.7	32.35	27.38
315	HR 191	42.8	20.87	25.12
316	HR 192	42.9	24.65	23.32
317	HR 193	43	21.31	22.05
318	HR 194	43.1	15.13	21.43
319	HR 195	43.2	26.89	21.27
320	HR 196	43.3	25.43	20.73
321	HR 197	43.4	17.25	19.68
322	HR 198	43.5	15.14	18.69
323	HR 199	43.6	19.33	18.06
324	HR 200	43.7	18.63	17.58
325	HR 201	43.8	16.44	17.13
326	HR 202	43.9	16.10	16.73
327	HR 203	44	16.71	16.35
328	HR 204	44.1	16.76	15.85
329	HR 205	44.2	19.96	15.16
330	HR 206	44.3	9.07	14.47
331	HR 207	44.4	12.10	14.50
332	HR 208	44.5	12.79	15.31
333	HR 209	44.6	24.04	16.38
334	HR 210	44.7	15.74	17.03
335	HR 211	44.8	17.75	17.48
336	HR 212	44.9	15.49	18.03
337	HR 213	45	20.78	18.90
338	HR 214	45.1	19.02	20.04
339	HR 215	45.2	17.34	21.53
340	HR 216	45.3	29.35	23.25
341	HR 217	45.4	18.12	24.66
342	HR 218	45.5	30.83	25.72
343	HR 219	45.6	30.64	25.85
344	HR 220	45.7	19.98	25.11

4.2.3. Packrat Section, Eastern Nevada

Serial	Sample #	Height (m)	$CaCO_3$%	0.01 spline
1	PKRT 1A	-10	76.83	82.00
2	PKRT 2A	-9.9	97.00	84.79
3	PKRT 3A	-9.8	76.02	86.96
4	PKRT 4A	-9.7	96.78	89.14
5	PKRT 5A	-9.6	81.51	91.16
6	PKRT 6A	-9.5	96.70	93.21
7	PKRT 7A	-9.4	97.04	94.54
8	PKRT 8A	-9.3	95.59	94.63
9	PKRT 9A	-9.2	96.31	93.46
10	PKRT 10A	-9.1	85.91	91.29
11	PKRT 11A	-9	84.85	88.63
12	PKRT 12A	-8.9	94.19	85.25
13	PKRT 13A	-8.8	84.77	80.51
14	PKRT 14A	-8.7	81.32	74.99
15	PKRT 15A	-8.6	56.22	70.37
16	PKRT 16A	-8.5	55.93	68.80
17	PKRT 17A	-8.4	75.29	70.36
18	PKRT 18A	-8.3	84.57	73.11
19	PKRT 19A	-8.2	78.44	75.69
20	PKRT 20A	-8.1	72.22	78.56
21	PKRT 21A	-8	69.85	82.69
22	PKRT 22A	-7.9	97.36	87.89
23	PKRT 23A	-7.8	94.53	92.34
24	PKRT 24A	-7.7	95.77	95.15
25	PKRT 25A	-7.6	98.67	96.04
26	PKRT 26A	-7.5	97.59	94.99
27	PKRT 27A	-7.4	88.85	92.42
28	PKRT 28A	-7.3	88.07	89.08
29	PKRT 29A	-7.2	95.30	85.29
30	PKRT30A	-7.1	77.10	81.45
31	PKRT 31A	-7	77.64	79.11
32	PKRT 32A	-6.9	61.03	79.53
33	PKRT 33A	-6.8	88.17	83.01
34	PKRT 34A	-6.7	93.27	87.51
35	PKRT 35A	-6.6	95.12	91.23
36	PKRT 36A	-6.5	96.02	93.47
37	PKRT 37A	-6.4	93.67	94.30
38	PKRT 38A	-6.3	94.31	94.27
39	PKRT 39A	-6.2	77.83	93.89
40	PKRT 40A	-6.1	100	93.16
41	PKRT 41A	-6	99.52	90.25
42	PKRT 42A	-5.9	91.10	84.51

43	PKRT 43A	-5.8	82.81	77.07
44	PKRT 44A	-5.7	52.66	70.44
45	PKRT 45A	-5.6	43.84	67.54
46	PKRT 46A	-5.5	77.14	68.30
47	PKRT 47A	-5.4	91.74	69.21
48	PKRT 48A	-5.3	68.86	67.87
49	PKRT 49A	-5.2	58.36	65.25
50	PKRT 50A	-5.1	59.46	62.94
51	PKRT 51A	-5	72.84	61.55
52	PKRT 52A	-4.9	42.49	61.36
53	PKRT 53A	-4.8	67.19	63.41
54	PKRT 54A	-4.7	71.77	66.73
55	PKRT 55A	-4.6	76.47	70.40
56	PKRT 56A	-4.5	62.19	74.50
57	PKRT 57A	-4.4	67.65	79.67
58	PKRT 01	-4.3	96.45	84.70
59	PKRT 02	-4.2	100	86.78
60	PKRT 03	-4.1	79.96	84.71
61	PKRT 04	-4	89.66	79.27
62	PKRT 05	-3.9	61.75	71.42
63	PKRT 06	-3.8	70.06	63.01
64	PKRT 07	-3.7	51.97	55.20
65	PKRT 08	-3.6	40.64	49.64
66	PKRT 09	-3.5	39.81	47.48
67	PKRT 10	-3.4	56.03	48.34
68	PKRT 11	-3.3	63.94	50.74
69	PKRT 12	-3.2	48.16	54.42
70	PKRT 13	-3.1	36.93	60.96
71	PKRT 14	-3	74.87	70.69
72	PKRT 15	-2.9	92.06	80.70
73	PKRT 16	-2.8	96.29	88.22
74	PKRT 17	-2.7	95.63	92.38
75	PKRT 18	-2.6	90.89	93.90
76	PKRT 19	-2.5	88.95	94.08
77	PKRT 20	-2.4	95.15	93.75
78	PKRT 21	-2.3	95.35	93.04
79	PKRT 22	-2.2	93.58	92.13
80	PKRT 23	-2.1	87.41	91.63
81	PKRT 24	-2	87.42	92.27
82	PKRT 25	-1.9	93.25	94.09
83	PKRT 26	-1.8	94.63	96.35
84	PKRT 27	-1.7	100	97.94
85	PKRT 28	-1.6	96.99	97.81
86	PKRT 29	-1.5	94.57	95.93

87	PKRT 30	-1.4	92.68	92.42
88	PKRT 31	-1.3	95.45	87.20
89	PKRT 32	-1.2	88.48	80.46
90	PKRT 33	-1.1	54.94	73.74
91	PKRT 34	-1	79.38	69.34
92	PKRT 35	-0.9	52.26	67.61
93	PKRT 36	-0.8	79.90	69.13
94	PKRT 37	-0.7	57.04	73.12
95	PKRT 38	-0.6	86.24	79.20
96	PKRT 39	-0.5	85.20	85.41
97	PKRT 40	-0.4	93.51	90.22
98	PKRT 41	-0.3	98.04	92.40
99	PKRT 42	-0.2	91.00	91.33
100	PKRT 43	-0.1	91.10	87.25
101	PKRT 44	0	92.12	80.69
102	PKRT 45	0.1	53.56	73.03
103	PKRT 46	0.2	67.88	66.68
104	PKRT 47	0.3	60.37	61.86
105	PKRT 48	0.4	62.16	58.25
106	PKRT 49	0.5	53.82	55.52
107	PKRT 50	0.6	53.14	53.72
108	PKRT 51	0.7	50.27	52.83
109	PKRT 52	0.8	48.00	52.56
110	PKRT 53	0.9	69.75	52.15
111	PKRT 54	1	49.30	50.71
112	PKRT 55	1.1	27.18	49.51
113	PKRT 56	1.2	71.99	49.46
114	PKRT 57	1.3	42.96	49.21
115	PKRT 58	1.4	43.34	49.46
116	PKRT 59	1.5	61.63	50.61
117	PKRT 60	1.6	38.56	52.43
118	PKRT 61	1.7	76.10	55.45
119	PKRT 62	1.8	19.70	59.45
120	PKRT 63	1.9	75.95	65.15
121	PKRT 64	2	81.70	69.03
122	PKRT 65	2.1	84.70	68.10
123	PKRT 66	2.2	75.62	61.98
124	PKRT 67	2.3	40.67	53.39
125	PKRT 68	2.4	16.89	46.96
126	PKRT 69	2.5	35.65	45.12
127	PKRT 70	2.6	74.59	45.53
128	PKRT 71	2.7	51.40	44.56
129	PKRT 72	2.8	22.60	42.35
130	PKRT 73	2.9	71.66	40.30

131	PKRT 74	3	9.34	38.41
132	PKRT 75	3.1	14.00	39.26
133	PKRT 76	3.2	88.95	41.73
134	PKRT 77	3.3	36.43	41.97
135	PKRT 78	3.4	38.15	41.38
136	PKRT 79	3.5	1.04	42.09
137	PKRT 80	3.6	72.84	44.25
138	PKRT 81	3.7	61.67	43.37
139	PKRT 82	3.8	48.12	38.03
140	PKRT 83	3.9	9.98	30.53
141	PKRT 84	4	19.12	24.43
142	PKRT 85	4.1	3.35	20.74
143	PKRT 86	4.2	56.05	18.47
144	PKRT 87	4.3	6.37	15.40
145	PKRT 88	4.4	0.66	13.43
146	PKRT 89	4.5	11.81	14.09
147	PKRT 90	4.6	3.21	16.84
148	PKRT 91	4.7	63.42	19.95
149	PKRT 92	4.8	4.24	21.23
150	PKRT 93	4.9	1.14	23.28
151	PKRT 94	5	16.22	27.15
152	PKRT 95	5.1	67.47	30.00
153	PKRT 96	5.2	46.98	28.04
154	PKRT 97	5.3	2.19	22.75
155	PKRT 98	5.4	1.45	18.71
156	PKRT 99	5.5	16.32	17.80
157	PKRT 100	5.6	16.53	18.86
158	PKRT 101	5.7	34.92	19.89
159	PKRT 102	5.8	34.99	19.04
160	PKRT 103	5.9	3.07	16.90
161	PKRT 104	6	3.36	16.25
162	PKRT 105	6.1	13.88	18.09
163	PKRT 106	6.2	37.17	21.15
164	PKRT 107	6.3	27.61	23.67
165	PKRT 108	6.4	12.61	26.02
166	PKRT 109	6.5	34.82	29.18
167	PKRT 110	6.6	6.60	32.67
168	PKRT 111	6.7	84.59	35.46
169	PKRT 112	6.8	6.98	34.84
170	PKRT 113	6.9	47.10	32.88
171	PKRT 114	7	25.11	30.01
172	PKRT 115	7.1	17.77	27.52
173	PKRT 116	7.2	33.24	26.13
174	PKRT 117	7.3	28.05	25.39

175	PKRT 118	7.4	8.28	25.53
176	PKRT 119	7.5	29.81	26.80
177	PKRT 120	7.6	38.88	27.35
178	PKRT 121	7.7	42.05	25.52
179	PKRT 122	7.8	5.25	21.86
180	PKRT 123	7.9	15.50	18.94
181	PKRT 124	8	15.72	17.55
182	PKRT 125	8.1	7.82	17.42
183	PKRT 126	8.2	41.20	17.59
184	PKRT 127	8.3	7.79	16.56
185	PKRT 128	8.4	14.34	15.35
186	PKRT 129	8.5	17.17	14.56
187	PKRT 130	8.6	5.64	14.49
188	PKRT 131	8.7	29.84	15.40
189	PKRT 132	8.8	5.96	16.98
190	PKRT 133	8.9	5.29	20.18
191	PKRT 134	9	27.99	24.45
192	PKRT 135	9.1	47.43	27.02
193	PKRT 136	9.2	34.32	25.76
194	PKRT 137	9.3	6.13	21.67

4.3. Stable Isotopes ($\delta^{13}C$ and $\delta^{18}O$) Measurements

4.3.1. The GSSP section, Drum Mountain, Western Utah

Serial	Sample #	Height (m)	$\delta^{13}C$	$\delta^{13}C$ 1.0 spline	$\delta^{18}O$	$\delta^{18}O$ 1.0 spline
1	DM -25	55	0.194	0.355	-9.178	-8.921
2	DM -15	56	0.978	0.640	-7.972	-8.424
3	DM -05	57	0.461	0.715	-8.538	-8.290
4	DM 11	58	0.777	0.737	-8.157	-8.365
5	DM 30	58.95	0.747	0.662	-8.597	-8.591
6	DM 34	59.15	0.820	0.627	-9.001	-8.640
7	DM 38	59.35	0.618	0.585	-8.414	-8.686
8	DM 42	59.55	0.698	0.541	-8.438	-8.729
9	DM 46	59.75	-0.234	0.498	-8.729	-8.769
10	DM 50	59.95	0.484	0.462	-9.527	-8.801
11	DM 54	60.15	0.687	0.430	-8.894	-8.821
12	DM 57	60.35	0.736	0.398	-8.416	-8.833
13	DM 62	60.55	0.002	0.365	-9.025	-8.841
14	DM 66	60.75	0.544	0.334	-8.882	-8.847
15	DM 70	60.95	0.354	0.308	-8.650	-8.853
16	DM 74	61.15	0.161	0.287	-8.820	-8.863
17	DM 78	61.35	-0.225	0.275	-9.419	-8.877
18	DM 86	61.75	0.656	0.272	-8.312	-8.926
19	DM 90	61.95	0.918	0.271	-8.193	-8.975
20	DM 94	62.15	-0.064	0.268	-9.456	-9.039
21	DM 98	62.35	-0.178	0.270	-9.321	-9.108
22	DM 102	62.55	0.351	0.281	-9.649	-9.174
23	DM 106	62.75	0.227	0.301	-8.774	-9.232
24	DM 110	62.95	0.234	0.327	-8.803	-9.286
25	DM 114	63.15	0.184	0.357	-9.245	-9.329
26	DM 118	63.35	0.412	0.386	-9.580	-9.352
27	DM 122	63.55	0.835	0.408	-10.658	-9.343
28	DM 126	63.75	0.553	0.417	-9.138	-9.295
29	DM 130	63.95	0.592	0.413	-10.010	-9.216
30	DM 134	64.15	0.453	0.399	-8.804	-9.118
31	DM 138	64.35	0.290	0.378	-8.577	-9.020
32	DM 142	64.55	0.565	0.358	-8.949	-8.938
33	DM 146	64.75	-0.025	0.344	-8.540	-8.883
34	DM 150	64.95	0.217	0.341	-8.872	-8.865
35	DM 154	65.15	-0.122	0.354	-7.615	-8.889
36	DM 158	65.35	0.273	0.381	-8.902	-8.956
37	DM 162	65.55	0.548	0.416	-9.496	-9.054
38	DM 166	65.75	0.475	0.450	-9.325	-9.166
39	DM 170	65.95	0.912	0.476	-9.248	-9.284
40	DM 174	66.15	0.503	0.488	-9.725	-9.399

41	DM 178	66.35	0.714	0.486	-9.586	-9.505
42	DM 182	66.55	0.693	0.471	-9.748	-9.599
43	DM 186	66.75	0.398	0.447	-9.600	-9.680
44	DM 190	66.95	0.587	0.421	-9.428	-9.748
45	DM 194	67.15	-0.282	0.400	-10.073	-9.804
46	DM 198	67.35	0.514	0.393	-9.906	-9.843
47	DM 206	67.75	0.270	0.421	-10.297	-9.867
48	DM 210	67.95	0.283	0.457	-9.992	-9.853
49	DM 214	68.15	0.396	0.506	-9.529	-9.830
50	DM 222	68.55	0.909	0.624	-9.142	-9.782
51	DM 226	68.75	0.115	0.681	-9.555	-9.766
52	DM 230	68.95	1.134	0.731	-10.073	-9.751
53	DM 234	69.15	0.930	0.766	-10.041	-9.731
54	DM 262	70.55	0.805	0.349	-9.711	-9.343
55	DM 273	71.1	1.306	-0.190	-8.438	-9.141
56	DM 274	71.15	0.507	-0.247	-9.383	-9.126
57	DM 277	71.3	0.210	-0.419	-8.856	-9.087
58	DM 282	71.55	-1.877	-0.667	-9.350	-9.037
59	DM 286	71.75	-1.954	-0.776	-9.067	-9.009
60	DM 287	71.8	-5.764	-0.786	-9.134	-9.004
61	DM 289	71.9	-0.663	-0.784	-8.825	-8.995
62	DM 290	71.95	0.295	-0.775	-9.027	-8.992
63	DM 291	72	-0.018	-0.760	-8.817	-8.989
64	DM 297	72.3	0.783	-0.614	-8.903	-8.991
65	DM 298	72.35	0.660	-0.585	-9.005	-8.994
66	DM 299	72.4	-2.391	-0.555	-8.844	-8.998
67	DM 301	72.5	-0.138	-0.495	-9.137	-9.008
68	DM 302	72.55	0.594	-0.465	-8.928	-9.014
69	DM 303	72.6	-0.547	-0.436	-9.150	-9.020
70	DM 305	72.7	0.464	-0.378	-9.023	-9.034
71	DM 306	72.75	-0.856	-0.351	-9.149	-9.042
72	DM +02	72.95	-0.110	-0.243	-8.807	-9.076
73	DM +03	73.05	-0.110	-0.191	-8.786	-9.095
74	DM +04	73.15	-1.092	-0.138	-9.539	-9.115
75	DM +05	73.25	0.201	-0.084	-9.264	-9.135
76	DM +06	73.35	-0.020	-0.031	-9.351	-9.154
77	DM +08	73.55	0.147	0.075	-8.954	-9.192
78	DM +10	73.75	0.127	0.177	-9.207	-9.228
79	DM +12	73.95	0.493	0.272	-8.722	-9.263
80	DM +14	74.15	0.377	0.357	-9.322	-9.294
81	DM +16	74.35	0.387	0.434	-9.567	-9.312
82	DM +18	74.55	0.385	0.503	-10.168	-9.308
83	DM +20	74.75	0.625	0.565	-9.053	-9.277
84	DM +28	75.55	0.683	0.712	-9.229	-8.989

85	DM +33	76.05	1.220	0.710	-8.146	-8.778
86	DM +28	76.55	0.514	0.638	-8.297	-8.652
87	DM +43	77.05	0.034	0.579	-9.354	-8.594
88	DM +48	77.55	0.757	0.594	-8.235	-8.532
89	DM +53	78.05	0.533	0.655	-8.637	-8.496
90	DM +58	78.55	0.968	0.734	-8.315	-8.501
91	DM +63	79.05	0.747	0.796	-8.481	-8.566
92	DM +73	80.05	0.805	0.872	-8.795	-8.825
93	DM +78	80.55	0.990	0.880	-8.974	-8.952
94	DM +83	81.05	0.912	0.857	-9.395	-9.025
95	DM +88	81.55	0.799	0.810	-8.768	-9.023
96	DM +98	83.55	0.427	0.778	-9.051	-8.562
97	DM +113	84.05	1.048	0.897	-7.822	-8.329
98	DM +118	84.55	0.951	1.032	-8.501	-8.126
99	DM +123	85.05	1.527	1.142	-7.260	-7.979
100	DM +128	85.55	1.244	1.197	-7.960	-7.924
101	DM +133	86.05	0.823	1.229	-8.534	-7.896
102	DM +138	86.55	1.572	1.276	-7.480	-7.830
103	DM +140	86.75	1.175	1.295	-7.867	-7.800

4.3.2. Marjum Pass Section, House Range, Western Utah

Serial	Sample #	Height (m)	$\delta^{13}C$	$\delta^{13}C$ 1.0 spline	$\delta^{18}O$	$\delta^{18}O$ 1.0 spline
1	HR -124	0	-0.735	-0.549	-8.254	-9.062
2	HR -122	1.24	-0.062	-0.438	-12.254	-10.863
3	HR -118	3.72	-1.466	-1.145	-8.485	-9.222
4	HR -113	6.82	-0.149	-0.387	-9.741	-9.644
5	HR -108	9.92	-0.397	-0.482	-10.442	-10.405
6	HR -107	10.54	-1.182	-0.322	-10.459	-10.186
7	HR -106	11.16	0.640	-0.016	-9.895	-9.816
8	HR -105	11.78	0.285	0.240	-9.210	-9.402
9	HR -104	12.4	0.469	0.390	-8.633	-9.079
10	HR -102	13.6	0.458	0.471	-9.188	-8.748
11	HR -098	14	0.263	0.485	-8.887	-8.606
12	HR -093	14.5	0.558	0.517	-8.417	-8.402
13	HR -088	15	0.645	0.544	-7.794	-8.257
14	HR -083	15.5	0.559	0.548	-8.206	-8.256
15	HR -078	16	0.456	0.530	-8.329	-8.410
16	HR -073	16.5	0.702	0.494	-7.974	-8.694
17	HR -68	17	0.013	0.440	-10.781	-9.042
18	HR -063	17.5	0.869	0.382	-7.545	-9.334
19	HR -58	18	-0.145	0.295	-11.367	-9.637
20	HR -053	18.5	0.547	0.193	-8.683	-9.865
21	HR -48	19	-0.004	0.058	-11.536	-10.094
22	HR -043	19.5	-0.228	-0.095	-8.294	-10.337
23	HR -38	20	-0.311	-0.249	-11.435	-10.714
25	HR -28	21	-0.998	-0.621	-11.009	-11.376
26	HR -26	21.2	-0.344	-0.722	-11.675	-11.447
27	HR -24	21.4	0.222	-0.841	-11.611	-11.483
28	HR -22	21.6	-0.396	-0.978	-12.062	-11.477
29	HR -20	21.8	-2.051	-1.120	-11.314	-11.426
30	HR -18	22	-0.932	-1.245	-10.577	-11.333
31	HR -16	22.2	-1.740	-1.341	-11.111	-11.199
32	HR -14	22.4	-2.201	-1.396	-11.688	-11.017
33	HR -12	22.6	-1.995	-1.402	-12.128	-10.779
34	HR -10	22.8	-1.259	-1.363	-12.098	-10.487
35	HR -08	23	-0.381	-1.291	-9.185	-10.163
36	HR -06	23.2	-2.168	-1.198	-8.333	-9.849
37	HR -04	23.4	-0.708	-1.086	-9.144	-9.575
38	HR -02	23.6	-1.484	-0.965	-10.283	-9.351
39	HR 01	23.8	-0.596	-0.844	-8.637	-9.183
40	HR 03	24	-0.192	-0.739	-8.304	-9.083
41	HR 05	24.2	-0.001	-0.658	-8.223	-9.056
42	HR 07	24.4	-0.489	-0.606	-8.781	-9.097
43	HR 09	24.6	-0.464	-0.575	-8.956	-9.190

44	HR 11	24.8	-1.725	-0.558	-9.151	-9.310
45	HR 13	25	-0.606	-0.545	-11.031	-9.429
47	HR 17	25.4	0.274	-0.557	-10.625	-9.585
48	HR 19	25.6	-0.014	-0.597	-10.946	-9.610
49	HR 21	25.8	-1.116	-0.656	-8.231	-9.613
50	HR 23	26	-0.253	-0.724	-8.357	-9.619
51	HR 25	26.2	-1.630	-0.792	-9.837	-9.641
52	HR 27	26.4	-0.827	-0.848	-8.742	-9.674
53	HR 29	26.6	-0.988	-0.890	-10.533	-9.709
54	HR 31	26.8	-1.236	-0.917	-10.301	-9.731
55	HR 33	27	-1.473	-0.929	-10.454	-9.731
56	HR 35	27.2	-0.262	-0.933	-7.794	-9.712
57	HR 37	27.4	-1.052	-0.939	-10.443	-9.681
58	HR 39	27.6	-0.503	-0.954	-10.209	-9.626
59	HR 41	27.8	-0.467	-0.980	-9.910	-9.542
60	HR 43	28	-1.138	-1.017	-9.438	-9.433
61	HR 45	28.2	-1.587	-1.054	-10.653	-9.309
62	HR 47	28.4	-0.929	-1.086	-8.277	-9.183
63	HR 49	28.6	-0.930	-1.111	-8.779	-9.080
64	HR 51	28.8	-1.326	-1.126	-8.738	-9.020
65	HR 53	29	-1.281	-1.127	-8.609	-9.014
66	HR 55	29.2	-1.266	-1.113	-8.681	-9.071
67	HR 57	29.4	-0.980	-1.083	-8.347	-9.192
68	HR 59	29.6	-1.180	-1.040	-8.631	-9.371
69	HR 61	29.8	-0.925	-0.987	-10.036	-9.590
70	HR 63	30	-1.060	-0.926	-10.539	-9.821
71	HR 65	30.2	-0.883	-0.861	-10.269	-10.043
72	HR 67	30.4	-0.447	-0.795	-10.523	-10.242
73	HR 69	30.6	-0.781	-0.733	-10.330	-10.412
74	HR 71	30.8	-0.680	-0.675	-11.186	-10.546
75	HR 73	31	-0.621	-0.623	-10.735	-10.644
76	HR 75	31.2	-0.680	-0.575	-10.392	-10.707
77	HR 77	31.4	-0.656	-0.534	-11.492	-10.744
78	HR 79	31.6	-0.499	-0.500	-10.696	-10.757
79	HR 81	31.8	-0.306	-0.478	-10.330	-10.759
80	HR 83	32	-0.280	-0.471	-11.616	-10.762
81	HR 85	32.2	-0.529	-0.480	-10.204	-10.776
82	HR 87	32.4	-0.421	-0.504	-10.001	-10.815
83	HR 89	32.6	-0.678	-0.542	-10.819	-10.891
84	HR 91	32.8	-0.230	-0.592	-9.712	-11.002
85	HR 93	33	-0.928	-0.652	-11.346	-11.141
86	HR 95	33.2	-0.296	-0.718	-11.412	-11.290
87	HR 97	33.4	-1.290	-0.787	-12.408	-11.425
88	HR 99	33.6	-0.692	-0.853	-11.433	-11.530

89	HR 101	33.8	-0.973	-0.914	-12.322	-11.600
90	HR 103	34	-1.195	-0.967	-11.854	-11.632
91	HR 105	34.2	-0.814	-1.012	-11.576	-11.630
92	HR 107	34.4	-0.898	-1.048	-11.417	-11.605
93	HR 109	34.6	-1.196	-1.075	-11.504	-11.566
94	HR 111	34.8	-1.271	-1.090	-11.456	-11.518
95	HR 113	35	-1.272	-1.090	-11.338	-11.469
96	HR 123	36	-0.629	-0.968	-10.896	-11.298
97	HR 133	37	-1.023	-0.887	-11.526	-11.340
98	HR 143	38	-0.762	-0.819	-11.427	-11.276
99	HR 153	39	-0.658	-0.789	-10.635	-10.953
100	HR 163	40	-0.972	-0.747	-10.848	-10.375
102	HR 183	42	-0.234	-0.204	-8.210	-8.139
103	HR 193	43	0.229	0.037	-6.683	-7.293
104	HR 203	44	0.146	0.055	-7.385	-7.181
105	HR 213	45	-0.350	-0.021	-7.471	-7.469
106	HR 220	45.7	0.157	-0.001	-7.859	-7.763

4.3.3. Packrat Section, Eastern Nevada

Serial	Sample #	Height (m)	$\delta^{13}C$	$\delta^{13}C$ (1.0 spl.)	$\delta^{18}O$	$\delta^{18}O$ (1.0 spl.)
1	PKRT 1A	-10	0.120	1.007	-7.850	-9.071
2	PKRT 2A	-9.9	1.610	1.052	-8.240	-9.188
3	PKRT 3A	-9.8	0.190	1.096	-10.770	-9.303
4	PKRT 4A	-9.7	2.290	1.136	-9.220	-9.411
5	PKRT 5A	-9.6	1.850	1.173	-9.620	-9.511
6	PKRT 6A	-9.5	1.560	1.204	-9.670	-9.602
7	PKRT 7A	-9.4	0.150	1.232	-9.400	-9.680
8	PKRT 8A	-9.3	2.330	1.257	-9.340	-9.746
9	PKRT 9A	-9.2	1.560	1.281	-12.780	-9.796
10	PKRT 10A	-9.1	1.440	1.304	-9.850	-9.830
11	PKRT 11A	-9	0.317	1.329	-8.981	-9.849
12	PKRT 12A	-8.9	1.030	1.359	-8.860	-9.857
13	PKRT 13A	-8.8	0.280	1.395	-9.380	-9.854
14	PKRT 14A	-8.7	1.690	1.435	-12.320	-9.841
15	PKRT 15A	-8.6	1.280	1.479	-8.950	-9.816
16	PKRT 16A	-8.5	1.940	1.524	-11.960	-9.783
17	PKRT 17A	-8.4	1.060	1.570	-8.320	-9.743
18	PKRT 18A	-8.3	2.300	1.613	-9.830	-9.703
19	PKRT 19A	-8.2	2.410	1.652	-9.480	-9.665
20	PKRT 20A	-8.1	1.380	1.687	-10.040	-9.634
21	PKRT 21A	-8	0.110	1.718	-8.180	-9.612
22	PKRT 22A	-7.9	2.040	1.744	-8.620	-9.602
23	PKRT 23A	-7.8	1.280	1.762	-8.550	-9.607
24	PKRT 24A	-7.7	2.800	1.770	-9.140	-9.625
25	PKRT 25A	-7.6	3.190	1.765	-9.200	-9.653
26	PKRT 26A	-7.5	3.160	1.746	-8.990	-9.688
27	PKRT 27A	-7.4	0.760	1.712	-11.130	-9.723
28	PKRT 28A	-7.3	2.070	1.669	-9.570	-9.755
29	PKRT 29A	-7.2	1.630	1.619	-12.630	-9.779
30	PKRT 30A	-7.1	1.490	1.564	-10.250	-9.792
31	PKRT 31A	-7	0.850	1.507	-8.480	-9.795
32	PKRT 32A	-6.9	-0.860	1.452	-10.180	-9.790
33	PKRT 33A	-6.8	0.720	1.400	-8.800	-9.779
34	PKRT 34A	-6.7	2.090	1.347	-10.370	-9.761
35	PKRT 35A	-6.6	2.490	1.290	-9.410	-9.736
36	PKRT 36A	-6.5	1.730	1.227	-11.520	-9.705
37	PKRT 37A	-6.4	-0.170	1.156	-9.700	-9.667
38	PKRT 38A	-6.3	1.610	1.078	-9.330	-9.624
39	PKRT 39A	-6.2	1.500	0.991	-9.610	-9.581
40	PKRT 40A	-6.1	2.490	0.894	-9.270	-9.539
41	PKRT 41A	-6	0.510	0.786	-8.290	-9.502
42	PKRT 42A	-5.9	0.370	0.672	-8.380	-9.472

43	PKRT 43A	-5.8	-0.230	0.553	-8.640	-9.447
44	PKRT 44A	-5.7	1.140	0.431	-9.830	-9.427
45	PKRT 45A	-5.6	1.140	0.307	-10.130	-9.406
46	PKRT 46A	-5.5	1.070	0.183	-9.970	-9.383
47	PKRT 47A	-5.4	-0.378	0.062	-8.814	-9.354
48	PKRT 48A	-5.3	-0.596	-0.050	-9.706	-9.320
49	PKRT 49A	-5.2	-0.687	-0.150	-9.601	-9.279
50	PKRT 50A	-5.1	-0.694	-0.234	-10.153	-9.230
51	PKRT 51A	-5	-1.963	-0.300	-9.438	-9.173
52	PKRT 52A	-4.9	-0.914	-0.346	-8.482	-9.109
53	PKRT 53A	-4.8	-0.250	-0.375	-9.278	-9.040
54	PKRT 54A	-4.7	-0.098	-0.390	-9.900	-8.967
55	PKRT 55A	-4.6	-0.123	-0.393	-8.921	-8.892
56	PKRT 56A	-4.5	-0.069	-0.386	-8.814	-8.817
57	PKRT 57A	-4.4	-0.241	-0.372	-10.105	-8.746
58	PKRT 1	-4.3	-0.211	-0.352	-7.342	-8.683
59	PKRT 2	-4.2	-0.357	-0.326	-8.034	-8.633
60	PKRT 3	-4.1	-0.384	-0.295	-7.817	-8.599
61	PKRT 4	-4	-0.250	-0.260	-7.532	-8.583
62	PKRT 5	-3.9	-0.228	-0.221	-7.984	-8.585
63	PKRT 6	-3.8	-0.479	-0.180	-10.660	-8.605
64	PKRT 7	-3.7	-0.356	-0.137	-8.448	-8.640
65	PKRT 8	-3.6	0.356	-0.094	-7.117	-8.692
66	PKRT 9	-3.5	-0.080	-0.053	-8.840	-8.759
67	PKRT 10	-3.4	-0.040	-0.014	-8.482	-8.841
68	PKRT 11	-3.3	-0.193	0.022	-9.136	-8.936
69	PKRT 12	-3.2	0.083	0.053	-8.274	-9.041
70	PKRT 13	-3.1	0.491	0.077	-10.264	-9.153
71	PKRT 14	-3	0.311	0.095	-10.979	-9.269
72	PKRT 15	-2.9	0.555	0.104	-9.352	-9.387
73	PKRT 16	-2.8	0.025	0.105	-8.732	-9.509
74	PKRT 17	-2.7	0.405	0.099	-8.894	-9.637
75	PKRT 18	-2.6	0.437	0.085	-8.494	-9.769
76	PKRT 19	-2.5	0.324	0.066	-8.831	-9.906
78	PKRT 21	-2.3	0.014	0.018	-9.579	-10.173
79	PKRT 22	-2.2	-0.582	-0.006	-12.359	-10.291
80	PKRT 23	-2.1	-0.460	-0.027	-12.549	-10.391
81	PKRT 24	-2	-1.257	-0.044	-12.052	-10.470
82	PKRT 25	-1.9	-0.046	-0.056	-10.566	-10.528
83	PKRT 26	-1.8	-0.814	-0.066	-10.834	-10.570
84	PKRT 27	-1.7	0.390	-0.075	-9.938	-10.599
85	PKRT 28	-1.6	0.812	-0.087	-9.710	-10.621
86	PKRT 29	-1.5	0.599	-0.104	-9.764	-10.639
87	PKRT 30	-1.4	0.097	-0.127	-11.344	-10.656

88	PKRT 31	-1.3	0.721	-0.155	-9.750	-10.670
89	PKRT 32	-1.2	0.501	-0.188	-9.714	-10.685
90	PKRT 33	-1.1	-1.131	-0.222	-10.601	-10.698
91	PKRT 34	-1	-0.573	-0.255	-10.593	-10.708
92	PKRT 35	-0.9	-0.811	-0.282	-11.706	-10.713
93	PKRT 36	-0.8	-0.885	-0.304	-10.526	-10.710
94	PKRT 37	-0.7	-0.836	-0.318	-10.918	-10.698
95	PKRT 38	-0.6	-0.681	-0.326	-11.957	-10.676
96	PKRT 39	-0.5	-0.242	-0.329	-10.078	-10.644
97	PKRT 40	-0.4	-0.478	-0.329	-11.852	-10.602
98	PKRT 41	-0.3	0.853	-0.329	-10.344	-10.553
99	PKRT 42	-0.2	-0.133	-0.329	-9.813	-10.499
100	PKRT 43	-0.1	0.109	-0.331	-9.818	-10.442
101	PKRT 44	0	-0.426	-0.335	-10.536	-10.385
102	PKRT 45	0.1	-0.425	-0.338	-11.507	-10.327
103	PKRT 46	0.2	-0.263	-0.340	-9.870	-10.269
104	PKRT 47	0.3	-0.526	-0.340	-10.013	-10.215
105	PKRT 48	0.4	-0.786	-0.337	-10.211	-10.165
106	PKRT 49	0.5	-0.305	-0.330	-9.681	-10.121
107	PKRT 50	0.6	-0.703	-0.319	-9.814	-10.086
108	PKRT 51	0.7	-0.278	-0.306	-9.582	-10.060
109	PKRT 52	0.8	-0.047	-0.289	-9.953	-10.043
110	PKRT 53	0.9	-0.362	-0.271	-9.983	-10.035
111	PKRT 54	1	-0.647	-0.252	-10.287	-10.035
112	PKRT 55	1.1	-0.103	-0.232	-10.058	-10.043
113	PKRT 56	1.2	-0.200	-0.212	-9.986	-10.057
114	PKRT 57	1.3	-0.058	-0.195	-10.098	-10.077
115	PKRT 58	1.4	-0.239	-0.180	-10.087	-10.104
116	PKRT 59	1.5	0.332	-0.168	-9.520	-10.135
117	PKRT 60	1.6	-0.346	-0.161	-9.959	-10.172
118	PKRT 61	1.7	-0.276	-0.159	-10.471	-10.211
119	PKRT 62	1.8	0.581	-0.161	-10.869	-10.252
120	PKRT 63	1.9	-0.022	-0.169	-10.764	-10.292
121	PKRT 64	2	0.040	-0.180	-10.237	-10.331
122	PKRT 65	2.1	-0.032	-0.195	-9.948	-10.369
123	PKRT 66	2.2	-0.518	-0.211	-10.184	-10.407
124	PKRT 67	2.3	-0.911	-0.227	-11.146	-10.444
125	PKRT 69	2.5	-0.227	-0.252	-10.946	-10.515
126	PKRT 71	2.7	-0.507	-0.268	-9.897	-10.583
127	PKRT 72	2.8	-0.613	-0.273	-10.875	-10.619
128	PKRT 73	2.9	-0.069	-0.276	-9.429	-10.656
130	PKRT 76	3.2	-0.124	-0.282	-11.382	-10.774
131	PKRT 77	3.3	-0.451	-0.285	-11.327	-10.808
132	PKRT 78	3.4	-0.111	-0.290	-10.437	-10.839

133	PKRT 81	3.7	-0.102	-0.318	-11.348	-10.901
134	PKRT 82	3.8	-0.228	-0.333	-11.149	-10.911
135	PKRT 83	3.9	-0.375	-0.351	-10.988	-10.915
136	PKRT 84	4	-0.402	-0.371	-10.945	-10.915
137	PKRT 86	4.2	-0.578	-0.419	-10.245	-10.904
138	PKRT 87	4.3	-0.674	-0.445	-11.307	-10.895
139	PKRT 89	4.5	-0.092	-0.505	-11.096	-10.872
140	PKRT 91	4.7	-0.483	-0.577	-10.196	-10.846
141	PKRT 95	5.1	-0.582	-0.746	-10.944	-10.800
142	PKRT 100	5.6	-1.269	-0.963	-11.193	-10.742
143	PKRT 101	5.7	-0.888	-1.000	-10.422	-10.730
144	PKRT 102	5.8	-1.106	-1.034	-10.714	-10.718
145	PKRT 104	6	-1.263	-1.089	-10.808	-10.697
146	PKRT 105	6.1	-1.156	-1.111	-10.528	-10.689
147	PKRT 106	6.2	-1.214	-1.129	-10.483	-10.682
148	PKRT 107	6.3	-1.263	-1.142	-10.284	-10.677
149	PKRT 108	6.4	-1.158	-1.153	-10.589	-10.674
150	PKRT 109	6.5	-1.280	-1.160	-10.978	-10.671
151	PKRT 110	6.6	-1.029	-1.164	-10.673	-10.668
152	PKRT 111	6.7	-0.943	-1.168	-10.641	-10.664
153	PKRT 113	6.9	-1.388	-1.171	-10.715	-10.649
154	PKRT 114	7	-1.223	-1.172	-10.699	-10.638
155	PKRT 115	7.1	-1.259	-1.172	-10.418	-10.623
156	PKRT 116	7.2	-0.871	-1.173	-10.328	-10.605
157	PKRT 117	7.3	-1.066	-1.176	-11.077	-10.582
158	PKRT 118	7.4	-0.871	-1.180	-10.518	-10.552
159	PKRT 119	7.5	-1.309	-1.185	-11.241	-10.517
160	PKRT 120	7.6	-1.098	-1.192	-10.786	-10.475
161	PKRT 121	7.7	-1.019	-1.199	-10.494	-10.428
162	PKRT 122	7.8	-1.376	-1.206	-10.324	-10.376
163	PKRT 123	7.9	-1.302	-1.213	-10.058	-10.322
164	PKRT 124	8	-1.201	-1.218	-10.166	-10.268
165	PKRT 126	8.2	-1.148	-1.224	-10.062	-10.162
166	PKRT 127	8.3	-1.478	-1.223	-10.214	-10.112
167	PKRT 128	8.4	-1.239	-1.219	-9.747	-10.065
168	PKRT 129	8.5	-1.242	-1.212	-9.864	-10.023
169	PKRT 130	8.6	-1.435	-1.201	-9.796	-9.984
170	PKRT 132	8.8	-1.154	-1.172	-9.628	-9.921
171	PKRT 134	9	-1.162	-1.135	-9.756	-9.871
172	PKRT 135	9.1	-0.981	-1.114	-10.265	-9.850
173	PKRT 136	9.2	-1.145	-1.092	-9.898	-9.829
174	PKRT 137	9.3	-0.888	-1.071	-9.922	-9.808

4.4. Carbonate Digestion Apparatus

4.4.1. Theoretical background

Carbonate digestion is a method that has been used to quantify the carbonate content, in percent (%), within any sediment or sedimentary rock sample. Carbonate rocks constitute 20-25% of the sedimentary rock record, and are observed in all stages, series and systems of the Phanerozoic. Limestone and dolomite constitute the majority of the carbonate sedimentary rock record. They might be pure or mixed. Pure carbonate rocks are rare and are composed entirely of carbonates (100%). Mixed carbonate rocks are abundant and have different carbonate percentage that ranges between 0 and 100%. Carbonates are mixed with non-carbonate sediments, primarily siliciclastic sediments. Carbonates might be deposited simultaneously along with siliciclastic sediments in the same depositional environment or serve as cement. Quantifying the carbonate content along with other geochemical and/or geophysical analyses of patterns in collected samples help to construct facies analysis models. These models lead to depositional environment interpretations, and decipher lateral and vertical lithological variations when correlated to time equivalent sections. This unravels stratigraphic complexity and can provide an insight into entire marine sedimentary basins.

This manual illustrates the carbonate digestion method when the vacuum-gasometric technique (Jones and Kaiteris, 1983) is used. First, 0.25 gm of powdered sample is allowed to react with 5 ml of highly concentrated phosphoric acid in a closed system. This reaction releases carbon dioxide gas, where

$$3CaCO_3 + 2H_3PO_4 \rightarrow Ca_3(PO_4)_2 + 3H_2O + 3CO_2 \qquad (1)$$

Because the reaction is performed in a closed pre-vacuumed system, the change in system pressure, ΔP, quantifies the released CO_2 gas. This change represents the

difference in pressure before and after the reaction. The carbonate percent is calculated when ΔP of a given sample is compared with the ΔP of a standard sample. A correction should be made for the volume differences between different reaction vessels. Three different cases have been observed throughout thousands of measurements;

1. If the given sample has no carbonates, its ΔP equals zero and its carbonate percent equals 0%.
2. If the given sample is composed of pure carbonate, its ΔP equals the ΔP of the standard sample and its carbonate percent equals 100%.
3. If the given sample has different contribution of carbonates and non-carbonate materials, its' ΔP and carbonate percent lie in between the upper two cases.

The third case is more common for fine grained marine sedimentary rocks than the first two cases.

4.4.2. Apparatus Components (see the appendecies figure below):

1- Reaction Vessels (RV): It has a main tube and side arm. Each reaction vessel has its own number.

2- Reaction vessel cap (RV cap): It has a valve that is referred to as the "RV cap valve". Each RV cap has a number that matches its corresponding reaction vessel.

3- O-rings and clamps: Used to attach the RVs with their caps. The O-rings should always be greased before use.

Note: All the above-mentioned parts can be assembled into one entity which is referred to as the **RV assembly**.

4- Reaction vessel rail: Holds all RVs and RV caps during measurements.

5- Vacuum meter: Measures the system pressure

6- Vacuum Pump: Pumps the air out of the system before the reaction starts. It also pumps the system down before releasing the CO_2 into the system.

7- System valve A: Connects the system with the vacuum pump.

8- System Valve B: Connects the system with the RV assembly through the system outlet.

9- System Outlet: Connects the system with the RV assembly

10- Electric vibrator: used for sample agitation.

4.4.3. Testing the system

1. Turn on the vacuum pump and the vacuum meter, open system valve A, and close system valve B.
2. Leave the pump on for ~5 minutes to equilibrate. Close system valve A, turn off the Vacuum pump and watch the vacuum meter.
3. Be sure that A and B valves are closed properly.
4. The pressure should increase slowly. If the pressure increases rapidly, then the system has a leak that should be fixed before use.

4.4.4. Sample Preparation

1. Grind ~1 gm of each rock sample to pass a ~63µ screen, using a pestle.

   Note: This increases the reaction surface area and reduces the chances of any leftover carbonates during reaction.

2. Place the powdered sample in a cupcake holder on an electric heater griddle, for one hour at ~110^{o} C.

   Note: This step removes the moisture and reduces sample weight errors. You can leave the sample on the griddle for a longer time at a lower temperature.

This apparatus consists of eight reaction vessels. Therefore it is preferred to prepare eight, or more, samples at a time.

4.4.5. Sample Measurement

1. Carefully add 0.25 gm of the dried sample into the main tube of the reaction vessel.

   Note: Place the RV on the scale and zero its weight. Then carefully add the 0.25 gm using a spatula. Be sure that the RV is cleaned properly.

2. Add 5 ml of phosphoric acid into the RV side arm using a pipette. Don't spill any acid on the sample in the main RV tube.
3. Grease the O-ring and use it to attach the RV with its cap. Clamp them together and tighten the clamp screw tightly.

   Notes:

   I. The RV number should always match the RV cap number.

   II. The RV side arm and the cap valve outlet should be on the opposite sides, at 180^{o} angle, during assembly (Fig. 1C).

   III. Don't tilt the RV assembly or it will start the reaction early.

4. Attach the RV cap male outlet to the system female inlet with the small O-ring in between.

   Notes:

   IV. Be sure that the small O-ring is in place and greased.

   V. Hold the RV assembly firmly against the system inlet.

   VI. Be sure that the RV cap valve is **OPEN**.

5. Turn on the Vacuum pump and the vacuum meter, and open system valves A and B. Let the system adjust for one minute.

6. Close the RV cap valve and system valve B and remove the RV assembly from the system inlet
7. Start the reaction by tilting the RV assembly enough to pore all the acid into the main tube. Then place it onto the RV rail.

   Note: The RV rail slot number should match the RV and RV cap numbers.
8. Leave it there for one and half (1.5) hours and shake it every half hour using the electric vibrator.
9. Connect the RV assembly after 1.5 hours to the system again and pump the system down for one minute. During this step:

   I. System valves A and B must be **OPEN**.

   II. The RV cap valve must be **CLOSED**.
10. **CLOSE** system valve **A** and record the vacuum meter reading.
11. **OPEN** the RV cap valve to release the CO_2 into the system and record the vacuum meter reading.
12. Take the RV assembly off the system inlet, disassemble and carefully clean the RV.
13. Start over for the next set of samples.

4.4.6. Overall Notes:

i. Turn off the meter and the pump after step 7, during the 1.5 hour reaction period.

ii. When it says open or close a certain valve (s), be sure that it is done properly.

iii. During steps 9-11, the RV assembly should always be held firmly against the system inlet.

This apparatus consists of eight reaction vessels. Therefore it is preferred to break the 13 steps of sample measurement into five sets. Each set of steps should be performed for the eight RVs before moving to the next set of steps.

- Set 1 includes steps 1 to 3
- Set 2 includes steps 4 to 7
- Set 3 includes step 8
- Set 4 includes steps 9-11
- Set 5 include steps 12 and 13

4.4.7. Carbonate Percent ($CaCO_3$%) Calculations

The difference between the two vacuum meter readings in steps 10 and 11, ΔP, represents the CO_2 gas pressure released by the reaction. ΔPs are calibrated for the volume difference among the eight RVs in the final $CaCO_3$% calculations. The carbonate percent final calculation for each sample incorporates ΔP of the measured sample and ΔP of the standard sample for the same RV.

$$CaCO_3\% = (\Delta P_{sample} / \Delta P_{Standard}) \times 100 \qquad (2)$$

The standard ΔP for each RV assembly is tabulated below. It is obtained through running pre-prepared samples of known carbonate percent (standards) for each RV assembly. The $CaCO_3$% values for these samples are 10, 40, 60, and 90 percent of $CaCO_3$. The 100% percent was calculated for each of the four ΔP readings for each RV assembly and the ΔP average is calculated. The standard deviation of these readings is <5, and the ΔP average serves as the standard ΔP for each RV assembly. The $\Delta P_{Standard}$ for every RV is tabulated below.

RV #	ΔP Standard	RV #	ΔP Standard
1	470.4791667	5	450.3472222
2	485.2083333	6	477.6180556
3	480.6041667	7	476.875
4	484.0416667	8	500.2083333

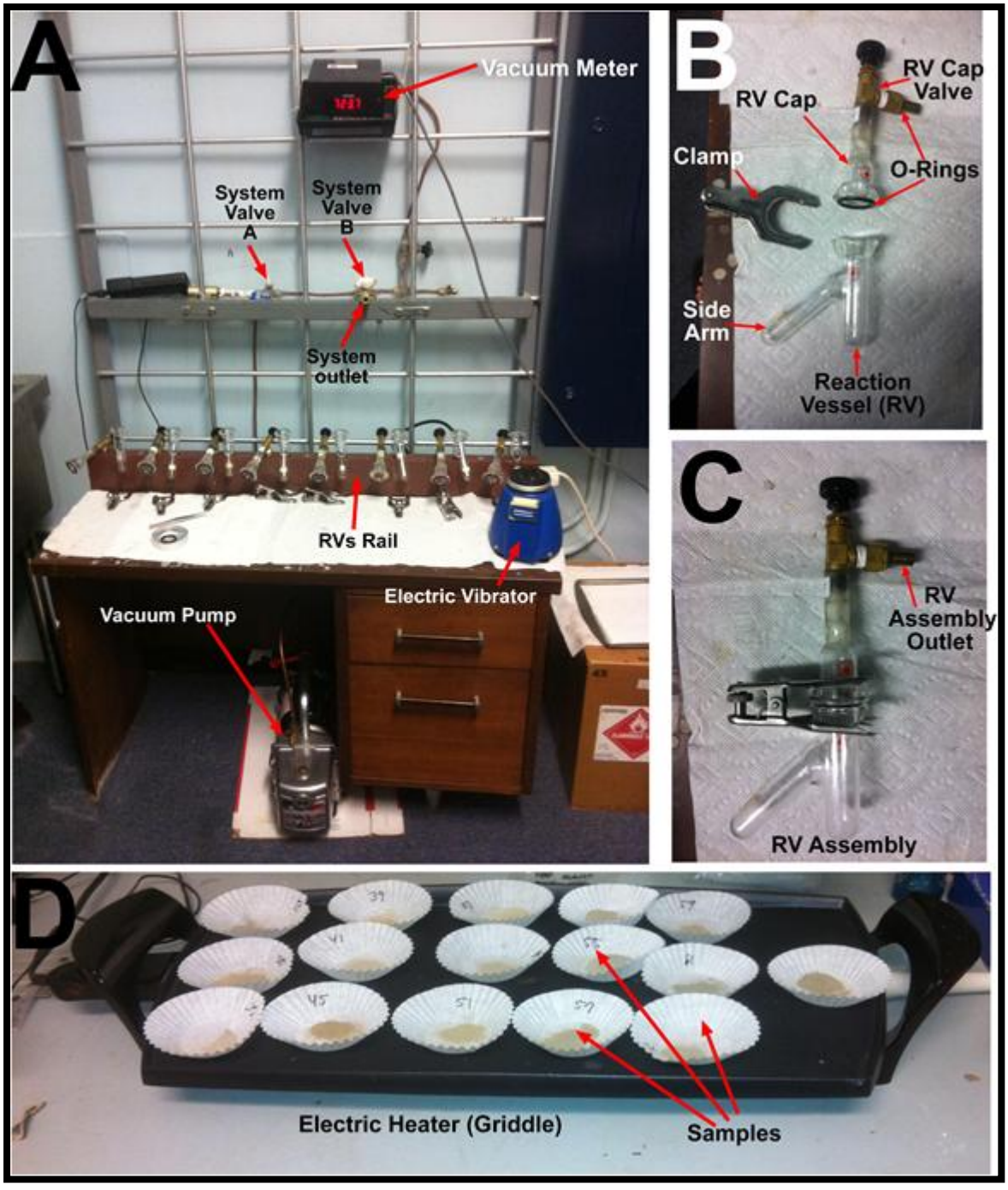

Appendecies Figure: Please email me: emaddelfarr@gmail.com or Dr. Ellwood: ellwood@lsu.edu if you want to build or use this apparatus.

4.4.8. Carbonate Percent (CaCO$_3$%) Sheet

RV #	Sample #	Sam. Wt 0.25 gm (±0.001)	P1	P2	Date /Time	Notes
1					Date	
2					/ / 20	
3					Start Time	
4						
5					End Time	
6						
7					Duration	
8					1.5 Hours	
1					Date	
2					/ / 20	
3					Start Time	
4						
5					End Time	
6						
7					Duration	
8					1.5 Hours	
1					Date	
2					/ / 20	
3					Start Time	
4						
5					End Time	
6						
7					Duration	
8					1.5 Hours	
1					Date	
2					/ / 20	
3					Start Time	
4						
5					End Time	
6						
7					Duration	
8					1.5 Hours	

VITA

Emad Elfar, the world long-awaited baby dinasour, was born in Egypt in 1982. I used to have the highest cumulative grades among my peers throughout my education path starting from elementary school to college. Therefore, Tanta University awarded me a bachler degree, offered me a full-time job, and paid for my graduate studies. I was appointed as teaching assistant and then assistant lecturer for about 10 years. After having my master degree from Tanta Unversity, I decided to pursue my PhD studies at Louisiana State University throught full funded PhD opurtunity from the Egyptian government. I had 4.0 GPA during my PhD program that lasted approximately 4 years. I was interested in geology since high school when the science teacher illustrated the formation and deformation of sedimentary rocks, and how water, oil, and gas were stored and migrated within these rocks. My curiosity drove me into undergraduate and graduate program in geology at Tanta University, and PhD program at LSU.